UNIVERSIDADE FEDERAL DE MINAS GERAIS
PROGRAMA DE PÓS-GRADUAÇÃO EM FÍSICA

PEDRO HENRIQUE REZENDE GONÇALVES

# Electronic Structure of Topological Materials probed by Angle-Resolved Photoemission Spectroscopy

BELO HORIZONTE
2021

Pedro Henrique Rezende Gonçalves

# Electronic Structure of Topological Materials probed by Angle-Resolved Photoemission Spectroscopy

Thesis submitted to Universidade Federal de Minas Gerais as a partial requirement for obtaining the Ph.D. degree in Physics.

Supervisor: Rogério Magalhães Paniago

Co-supervisor: Wendell Simões e Silva

Ph.D. sandwich supervisor: Andres Felipe Santander-Syro

Belo Horizonte

2021

Dados Internacionais de Catalogação na Publicação (CIP)

G635e Gonçalves, Pedro Henrique Rezende.
Electronic structure of topological materials probed by angle-resolved photoemission spectroscopy / Pedro Henrique Rezende Gonçalves. – 2021.
100f., enc. : il.

Orientador: Rogério Magalhães Paniago.
Coorientador: Wendell Simões e Silva.
Tese (doutorado) – Universidade Federal de Minas Gerais, Departamento de Física.
Bibliografia: f. 85-100.

1. Estrutura eletrônica. 2. Semimetais. 3. Fotoemissão. 4. Ondas de densidade de carga.
I. Título. II. Paniago, Rogério Magalhães. III. Universidade Federal de Minas Gerais, Departamento de Física.

CDU – 538.9 (043)

Ficha catalográfica elaborada por Romário Martins Ribeiro – CRB6 3595
Biblioteca Professor Manoel Lopes de Siqueira – Departamento de Física - UFMG

UNIVERSIDADE FEDERAL DE MINAS GERAIS
INSTITUTO DE CIÊNCIAS EXATAS
PROGRAMA DE PÓS-GRADUAÇÃO EM FÍSICA

## FOLHA DE APROVAÇÃO

A PRESENTE TESE, INTITULADA **"ELECTRONIC STRUCTURE OF TOPOLOGICAL MATERIALS PROBED BY ANGLE-RESOLVED PHOTOEMISSION SPECTROSCOPY"** DE AUTORIA DE **PEDRO HENRIQUE REZENDE GONÇALVES** SUBMETIDA À COMISSÃO EXAMINADORA, ABAIXO-ASSINADA, FOI APROVADA PARA OBTENÇÃO DO GRAU DE **DOUTOR EM CIÊNCIAS**, EM VINTE E UM DE JUNHO DE 2021.

Belo Horizonte, 21 de Junho de 2021.

Prof. Rogério Magalhães Paniago
Orientador do estudante
Departamento de Física/UFMG

Prof. Andrés Felipe Santander-Syro
Université Paris-Saclay

Profa. Simone Silva Alexandre
Departamento de Física/UFMG

Profa. Carolina Parra Gonzalez
Universidad Técnica Federico Santa María

Prof. Myriano Henriques de Oliveira Junior
Departamento de Física/UFMG

Documento assinado eletronicamente por **Andres Felipe Santander Syro**, **Usuário Externo**, em 21/06/2021, às 18:50, conforme horário oficial de Brasília, com fundamento no art. 5º do Decreto nº 10.543, de 13 de novembro de 2020.

Documento assinado eletronicamente por **Myriano Henriques de Oliveira Junior**, **Professor do Magistério Superior**, em 22/06/2021, às 10:35, conforme horário oficial de Brasília, com fundamento no art. 5º do Decreto nº 10.543, de 13 de novembro de 2020.

Documento assinado eletronicamente por **Rogerio Magalhaes Paniago**, **Professor do Magistério Superior**, em 23/06/2021, às 11:00, conforme horário oficial de Brasília, com fundamento no art. 5º do Decreto nº 10.543, de 13 de novembro de 2020.

Documento assinado eletronicamente por **Simone Silva Alexandre**, **Professora do Magistério Superior**, em 28/06/2021, às 10:17, conforme horário oficial de Brasília, com fundamento no art. 5º do Decreto nº 10.543, de 13 de novembro de 2020.

Documento assinado eletronicamente por **Carolina Ivón Parra Gonzáles**, **Usuário Externo**, em 06/07/2021, às 22:28, conforme horário oficial de Brasília, com fundamento no art. 5º do Decreto nº 10.543, de 13 de novembro de 2020.

A autenticidade deste documento pode ser conferida no site https://sei.ufmg.br/sei/controlador_externo.php?acao=documento_conferir&id_orgao_acesso_externo=0, informando o código verificador **0796017** e o código CRC **3E91A454**.

**Referência:** Processo nº 23072.232171/2021-91 SEI nº 0796017

***Dedicatória***

*Este trabalho é dedicado ao meu pai José Carlos Gonçalves*

# Acknowledgements

I would like to thank my advisor Prof. Rogério Paniago. His insistence was fundamental for the development of my doctorate, sometimes approaching stubbornness, but essential to the formation of my career.

I also would like to thank my co-advisor Prof. Wendell Simões for his collaboration in this work, guiding my transition from Scanning Tunneling Microscopy to ARPES. A special thank to Prof. Ângelo Malachias, also important for the execution of this work, particularly the first part. I extend my acknowledgment to all teachers and employees from the Physics Department who contributed to my formation.

I thank Prof. Andrés Santander-Syro for welcoming me as a member of his research group in Orsay (France) during the year of 2020. The acquired knowledge under his supervision was essential for the development of this thesis. I also thank him for the hospitality and friendship, making my stay in a foreign country during the Covid-19 crisis much more enjoyable.

I thank all colleagues from the UHV Nanoscopy laboratory in UFMG, specially Dra. Thaís Chagas, who had been collaborating with all my projects and gifted me with her friendship during all my student career. I also thank all colleagues from the SIM2D laboratory in Orsay that created an excellent working environment during my stay in Orsay.

I also thank my family and friends who provide the emotional support to face the academic life. A special thanks to my mother Izabel Cristina, always by my side; and my beautiful partner Viviane who took charge of putting a smile on my face during the last three years.

Finally, I thank the funding agencies CNPq and CAPES for the financial support I received during different stages of my academic life. I thank the financial and experimental support from LNLS-CNPEM during Synchrotron experiments. I thank the financial support from CRNS during my stay in France and the financial and experimental support from SOLEIL during Synchrotron experiments. Their help was primordial for the outcome of this thesis.

# Resumo

A pesquisa em materiais topológicos tem se mostrado uma extensa fonte de previsão e observação de novos e exóticos fenômenos em física da matéria condensada. Nos últimos 20 anos, surgiram uma variedade de novos materiais com propriedades topológicas. Os mais proeminentes são os Isolantes Topológicos e os Semimetais de Weyl. Nesta tese de doutorado, usamos Espectroscopia de Fotoemissão Resolvida em Ângulo (ARPES) para caracterizar a estrutura eletrônica de dois materiais topológicos: o isolante topológico quaternário $BiSbSe_{2.5}Te_{0.5}$ e o candidato a semimetal de Weyl $TaTe_4$. Relatamos a realização de um isolante topológico quaternário estável, $BiSbSe_{2.5}Te_{0.5}$, caracterizado por uma dopagem positiva e com portadores de carga com massa efetiva menor quando comparado ao $Bi_2Se_3$. Sobre o $TaTe_4$, relatamos a existência de uma superfície de Fermi bidimensional composta por quatro cones de Dirac/Weyl na primeira zona de Brillouin. A estrutura eletrônica desses estados metálicos se mostrou compatível com trabalhos anteriores encontrados na literatura, mostrando uma coexistência de ondas de densidade de cargas e estados topológicos em uma superfície de Fermi bidimensional.

**Palavras-chave**: isolantes topológicos, semimetais de Weyl, ondas de densidade de carga, espectroscopia de fotoemissão resolvida em ângulo.

# Abstract

The research in topological materials had been an extensive source for prediction and observation of new and exotic phenomena at the condensed matter level. During the last 20 years, a variety of new topological phases of matter had emerged. The most prominent are Topological Insulators and Weyl Semimetals. In this thesis, we used Angle-resolved Photoemission Spectroscopy to characterize the electronic structure of two topological materials: the quaternary topological insulator $BiSbSe_{2.5}Te_{0.5}$ and the topological Weyl semimetal candidate $TaTe_4$. We reported the realization of a stable quaternary topological insulator, $BiSbSe_{2.5}Te_{0.5}$, characterized by a positive doping and charge carriers with smaller effective mass when compared with $Bi_2Se_3$. About $TaTe_4$, we report a 2D Fermi surface composed by four Dirac/Weyl cones in the surface first Brillouin zone. The electronic structure of these metallic states is compatible with previous findings in the literature, showing a coexistence of CDW and topological features in a 2D Fermi surface.

**Keywords**: topological insulators, Weyl semimetals, charge-density waves, angle-resolved photoemission spectroscopy.

# Contents

# List of Figures

# Introduction

The theoretical prediction and consequent experimental realization of topological insulators in mid-2006 represented an important milestone in the research of condensed-matter physics. In 2016, Haldade, Thouless and Kosterlitz were awarded with the Physics Nobel Prize for their studies about the topological phases of matter. After the discovery of topological insulators, other types of topological materials emerged as new opportunities of research in that area, including the topological nodal semimetals. The universality of the effects present in those materials makes them important players for the idealization of new electronic devices based on spintronics and quantum computing. For a complete characterization of these materials, it is necessary to understand the behaviour of the electrons inside them, that is, to obtain information about their electronic bandstructure.

From the perspective of experimental physics, the main technique for acquiring information about the bandstructure of different materials is Angle-resolved Photoemission Spectroscopy (ARPES). Based on the photoelectric effect, this technique provides a direct relation between energy and crystalline momentum of electrons inside the material, among other properties. This thesis focuses on studying the electronic structure of topological materials using ARPES. The non-destructive character and high power of visualization of surface effects among different materials make ARPES the perfect technique for study topological materials. The content of this thesis is divided in four chapters covering the description of the physics behind topological materials, the experimental and theoretical aspects involving ARPES and the presentation of two projects developed during this doctorate.

The first chapter covers theoretical background about the main properties associated with topological materials. Some concepts of topological band theory are presented to familiarize the reader with the topological classification of electronic bandstructures. These concepts were presented in a historical order starting from the description of the quantum Hall effect, which started the foundations of the topological materials research. A comprehensive description about the theory of topological insulators is presented focusing

in the most important aspects, without entering on deeper theoretical discussions. In other words, this content should be a guide for experimentalist without further knowledge of topological band theory. The chapter ends with a brief discussion about topological nodal semimetals, focusing on the physical phenomena observed on photoemission experiments. Topological Weyl and Dirac semimetals are presented in this manner, together with a brief presentation of the recent discovered topological phase known as axion insulator.

The second chapter presents theoretical and experimental aspects associated to Angle-resolved Photoemission Spectroscopy (ARPES). Starting from the historical background describing the photoelectric effect and the development of experimental techniques associated with the photoemission phenomenon. The theory concerning the photoemission process is presented divided in two parts: the photoemission theory of independent electrons and the photoemission theory of interacting electrons; which includes a many-body approach of the photoemission process. After that, fundamental aspects related to the instrumentation and implementation of an ARPES experiment are presented, from the types of photon sources used in photoemission experiments to the design of the electron energy analyzer.

The next two chapters cover the scientific projects executed during this doctorate. The first project addresses the growth and characterization of the topological insulator $BiSbSe_{2.5}Te_{0.5}$. The realization of this quaternary compound as a topological insulator phase was performed through structural and chemical characterizations, showing the formation of a non-stoichiometric compound where the topological features remain. The electronic characterization of the material was accomplished by the observation of the topological surface states using ARPES.

The second project presents the results obtained during one year of doctoral stay at Université Paris-Saclay (France) under the supervision of Prof. Andrés Felipe Santander-Syro. The resulting project addresses the electronic properties of the quasi-1D transition metal tetrachalcogenide $TaTe_4$ studied by ARPES. $TaTe_4$ has an important role in topological materials research, since it is classified as a topological semimetal candidate and it also presents a charge-density wave (CDW) phase observed at room temperature. The interplay between CDW and topological features unlock interesting discussions about the electronic properties of the material, creating new targets for the quest of new exotic topological phases of matter.

At the end, a brief conclusion gathering the central results associated with the projects presented in this thesis and a list of articles published by the author in international scientific journals during his scientific career.

# Chapter 1

# Topological Materials

## 1.1 Topological Band Theory

### 1.1.1 Topological Invariants

Topology is the topic of mathematics interested in the properties of geometrical objects that are preserved under continuous transformations [1]. Two geometrical objects are considered topologically equivalent if they can be transformed into one another through continuous deformations, like flattening and stretching. For instance, a sphere is topologically equivalent to a cube or a disk (see figure 1.1). The same sphere is topologically distinct from a torus, since the transformation involves the appearance of a hole on the surface. In summary, this requirement is what topologically distinguishes different geometrical objects. The topological classification of geometrical objects implicates the determination of a particular number capable of distinguishing among different topological classes [1]. This number is called topological invariant. For parameterized surfaces, the topological invariant is determined using the Gauss-Bonnet formula [2], which relates the Gaussian curvature ($K$) of a surface $S$ with a number called Euler characteristic ($\chi$):

$$\chi = \frac{1}{2\pi}\int_S K dA \tag{1.1}$$

The Euler characteristic is easily calculated for convex polyhedra, $\chi = V - E + F$, where $V$, $E$ and $F$ are respectively the number of vertices, edges and faces of the polyhedron [3]. For general surfaces, the Euler characteristic is linked to the genus ($g$) of the surface: $\chi = 2 - 2g$; which denotes the number of holes [1].

There are several manners of classify different phases of matter. For instance, by their physical (solid, liquid and gas), electrical (metals and insulators) or magnetic

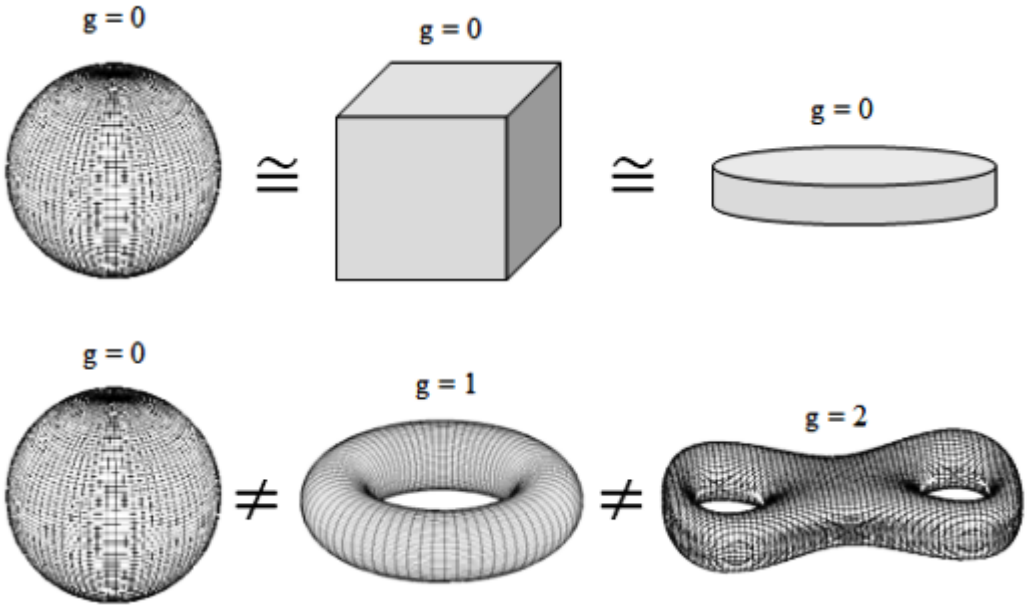


Figure 1.1 – Topological classification of the geometrical objects by the genus ($g$) - number of holes. Continuous deformations like flattening and stretching can transform a sphere into a cube or a disk (all have $g = 0$). However, continuous deformations cannot transform a sphere into objects with different genus ($g = 1, 2, ...$).

(diamagnets, paramagnets and ferromagnets) properties. The connection between topology and the different topological phases of matter is done by the topological classification of insulators [4]. Using topological considerations, insulators can be classified into different topological classes, linked to different topological invariants. An insulator is a material that presents an energy gap for electronic excitations, separating the ground state from all excited states. In other words, they have full-filled energy bands and an energy gap separating the last occupied electronic state from the first non-occupied state. Figure 1.2 shows the representative bandstructures of insulators, semiconductors, semimetals and metals. The topological classification of insulators associates the concept of continuous deformations to adiabatic changes in the Hamiltonian of the material [4]. Insulators are considered topologically equivalent if there is an adiabatic path where the Hamiltonians are transformed into one another, so the system always remains in the ground state. This process is only possible if there is an energy gap separating the ground state from the excited states. The size of gap controls how smooth the adiabatic displacements should be. Therefore, insulators are called topologically distinct if there is no adiabatic path to transform them into one another; in this case, the energy gap must vanish at some point.

The bandstructure of a material is obtained from the Hamiltonian of the many-body system under the crystalline periodic potential. According to Bloch's theorem [5], the

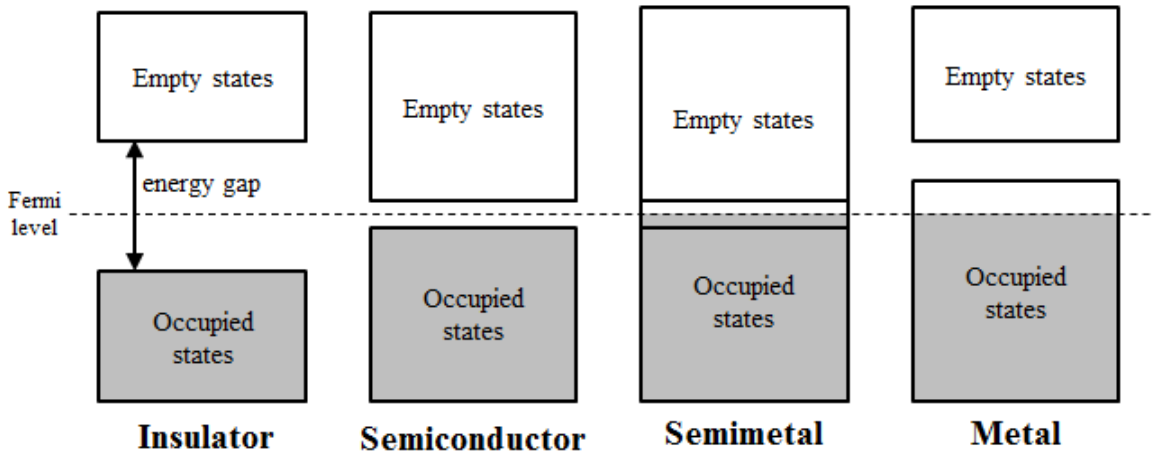


Figure 1.2 – Comparative representation of the electronic bandstructure of insulators, semiconductors, semimetals and metals. In insulators, occupied and non-occupied states are separated by an energy gap. Semiconductors are materials that have a relatively small energy gap, accessible to external excitations. Semimetals present an overlap between energy bands creating a zero energy gap. Metals do not present an energy gap between occupied and non-occupied states, so there are states available for electrical conduction.

electronic states in the crystal are expressed in terms of Bloch eigenstates:

$$|\psi_n(\mathbf{k})\rangle = e^{i\mathbf{k}\cdot\mathbf{r}}|u_n(\mathbf{k})\rangle \tag{1.2}$$

Where $u_n(\mathbf{k}) = u_n(\mathbf{k}+\mathbf{G})$ has the periodicity of the reciprocal lattice vector $\mathbf{G}$. The topological classification of insulators is manly associated with the concept of Berry phase ($\gamma_C$), or geometrical phase. It is a phase factor acquired by a quantum state during a adiabatic cycle in the parameter space of the Hamiltonian [6]. Along the closed path $C$, it is defined by the expression:

$$\gamma_C = -i \oint_C \langle u(\mathbf{k})|\nabla_{\mathbf{k}}|u(\mathbf{k})\rangle \cdot d\mathbf{k} \tag{1.3}$$

The argument of the integral is called Berry connection and it is analogous to the magnetic vector potential [7]. If the closed path $C$ defines a surface $S$, the application of Stoke's theorem [8] results in a expression for the Berry phase in terms of the surface integral:

$$\gamma_C = \int_S \nabla \times \mathbf{A}\, d^2\mathbf{k} \tag{1.4}$$

Where $\mathcal{F} = \nabla \times \mathbf{A}$ is called Berry curvature [6]. The analogy of the Berry connection

with the magnetic vector potential introduce important considerations. The Berry phase has the form of a magnetic flux $\Phi$, while the Berry curvature resembles the magnetic field $\mathbf{B}$. A gauge transformation displaces the Berry connection, whereas Berry curvature and Berry phase remains intact since they are gauge-invariant. The effect of the gauge transformation in the Bloch eigenstates is:

$$\mathbf{A} \rightarrow \mathbf{A}' = \mathbf{A} + \nabla\chi \tag{1.5a}$$

$$|\Psi\rangle \rightarrow |\Psi'\rangle = e^{i(q/\hbar)\chi}|\Psi\rangle \tag{1.5b}$$

An important consequence from the definition of the Berry phase is that the integrated Berry curvature over a close two-dimensional space is an integer multiple of $2\pi$. This quantization defines a topological invariant named Chern number ($n$), given by:

$$n = \frac{1}{2\pi}\oint_S \mathcal{F} d^2\mathbf{k} \tag{1.6}$$

This equation has the same structure of the Gauss-Bonnet formula in equation 1.1 with the Berry curvature $\mathcal{F}$ performing the role of the Gaussian curvature $K$. The Chern number defines different topological classes of insulators, i.e, insulators with different Chern numbers cannot be transform into one another unless the energy gap vanishes.

The topological classification of insulators implicates an interesting phenomenon when two topologically distinct insulators are disposed in contact. The energy gap should vanish at some point along the interface to maintain the continuity of the Bloch wavefunctions. As consequence, localized electronic states must appear at the interface [9]. The appearance of these edge states (or surface sates in the 3D case) creates a connection between topologically distinct electronic bands from both materials, locally closing the energy gap, see figure 1.3.

### 1.1.2 Quantum Hall Effect

The first system where notions of topology could be applied in the context of condensed matter physics was the quantum Hall effect [10]. The classical Hall effect occurs when a voltage is applied on a metallic plate subjected to a perpendicular magnetic field $\mathbf{B}$, see figure 1.4. The Lorentz force originated from the magnetic field is responsible for creating a charge accumulation perpendicularly to the electrical current $I$. This charge accumulation generates an electric field and, at some moment, the Lorentz forces originated from the electrical and magnetic fields cancel one another. The transverse voltage generated

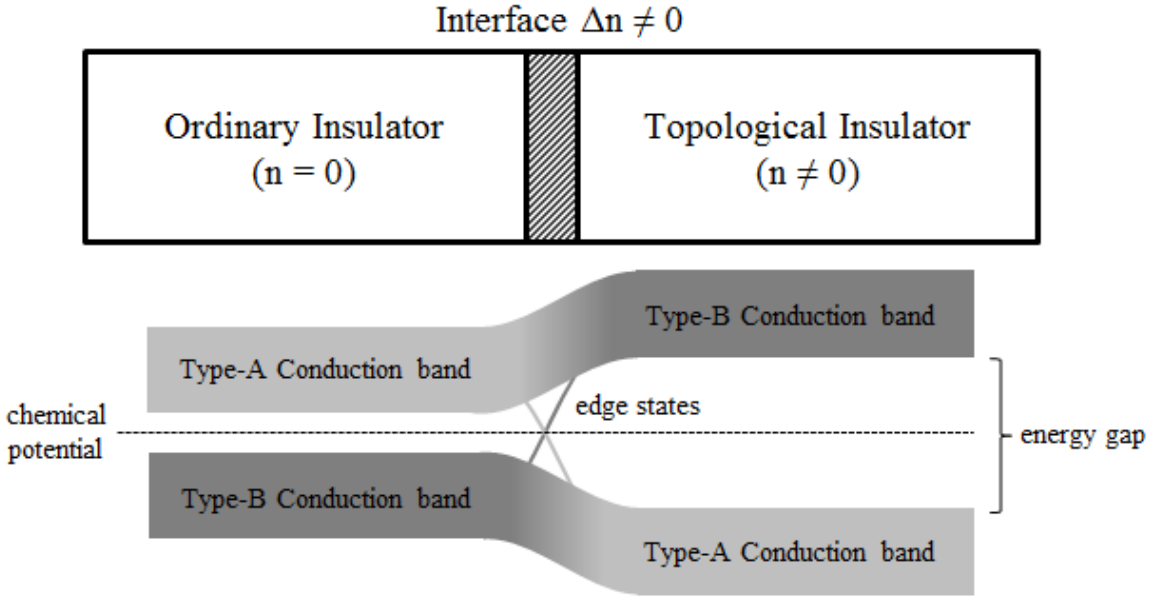


Figure 1.3 – Edge states at the interface between topologically distinct insulators. If the interface between two insulators has $\Delta n \neq 0$, the energy gap should vanish at the interface. The connection between conduction and valance bands of both materials is done by those edge states.

by the magnetic field is called Hall voltage ($V_H$) and the Hall conductivity ($\sigma_{xy}$) is defined by:

$$\sigma_{xy} = \frac{I}{V_H} = \frac{\rho_e e}{B} \tag{1.7}$$

Where $e$ is the electron charge and $\rho_e$ is the density of charge carriers. The classical Hall effect was first observed in the late 19th century by Edwin Hall [11] and the quantum version was discovered almost a hundred years later.

The quantum Hall effect was first observed by Klaus von Klitzing [12] at the metal-oxide-semiconductor junction of a Si-MOSFET transistor. In this system, an insulating layer of $SiO_2$ separates a layer of silicon doped with acceptors and a metal. An electric field is generated by a voltage applied between the metal and the semiconductor. Increasing the voltage, the electric field bends the energy levels of the semiconductor and the electrons near the interface can occupy the conduction band, so they move freely in the junction Si-$SiO_2$. This phenomenon is observed when a sufficiently intense magnetic field is applied to a two-dimensional electron gas (2DEG) subject to low temperatures [13]. The Hall conductance ($\sigma_{xy}$) is quantized in plateaus of integer multiples of $e^2/h$:

$$\sigma_{xy} = \nu \frac{e^2}{h} \tag{1.8}$$

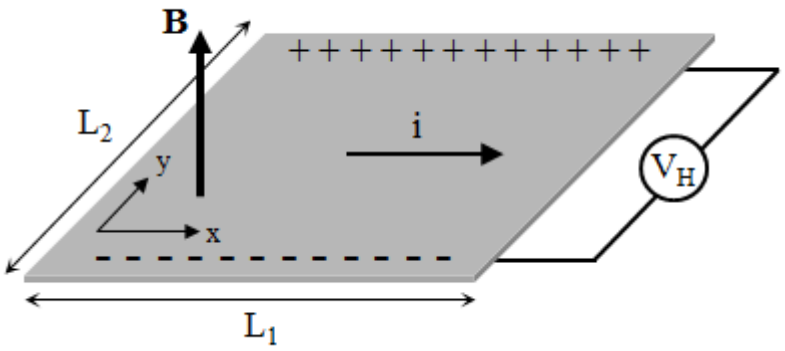


Figure 1.4 – Classical Hall effect. The Lorentz force generated by the magnetic field **B** produces a deflection of the charges in the direction perpendicular to the electrical current $I$. The charge accumulation on the edges generates the Hall voltage $V_H$.

The quantized Hall conductance is obtained by a quantum description of the system. Consider an electron confined to a two-dimensional rectangular plane with dimensions $L_1$ and $L_2$ as in figure 1.4. The Hamiltonian of the electron subjected to the external magnetic field **B** is given by [7] :

$$\hat{H} = \frac{1}{2m}(\mathbf{p} - e\mathbf{A})^2 \tag{1.9}$$

Where **p** is the momentum operator, **A** is the magnetic vector potential and $m$ is the electron mass. The solution of this problem depends on a suitable choosing of the vector potential **A**, i.e, a proper gauge transformation that makes the problem more easily solvable. Since the magnetic field is given by $\mathbf{B} = B\hat{\mathbf{z}}$, a suitable choice for the magnetic vector potential is $\mathbf{A} = xB\hat{\mathbf{y}}$. This gauge is called Landau gauge [14]. The Schrodinger equation describing the system is:

$$-\frac{\hbar^2}{2m}\left[\frac{\partial^2}{\partial x^2} + \left(\frac{\partial}{\partial y} - i\frac{eB}{\hbar}x\right)^2\right]\Psi(x,y) = E\Psi(x,y) \tag{1.10}$$

Assuming periodic boundary conditions in $y$, the eigenstates of the system can be described by:

$$\Psi(x,y) = \Theta(x)e^{ik_y \cdot y} \tag{1.11}$$

With $k_y = 2\pi q/L_2$ and q is an integer. The $\Theta(x)$ component is obtained from:

$$-\frac{\hbar^2}{2m}\left[\frac{\partial^2}{\partial x^2} - \left(k_y + \frac{eB}{\hbar}x\right)^2\right]\Theta(x) = E\Theta(x) \tag{1.12}$$

This expression has the form of a Schrodinger equation of a quantum harmonic oscillator [15] with the origin displaced by $x_0 = -\hbar k_y/eB$. The energy levels of the system are:

$$E_n = \left(n + \frac{1}{2}\right)\hbar\omega \tag{1.13}$$

Where $n$ is an integer and $\omega$ corresponds to the electron cyclotron frequency $\omega = eB/m$. The quantized energy levels are called Landau levels [16]. The eigenvalues $E_n$ are highly degenerated and the correspondent eigenstates can be parameterized by $k_y$, which defines a set of eigenstates with wavefunctions centered at different values of $x_0$. The dimensions of the system restricts the values of $x_0$ from 0 to $L_1$, which creates the following restrictions for $k_y$:

$$0 < |k_y| < \frac{eBL_1}{\hbar} \tag{1.14}$$

From these boundary conditions, it is possible to calculate the degeneracy ($D$) of each Landau level, i. e, the number of allowed values for $k_y$.:

$$D = \frac{eBL_1/\hbar}{2\pi/L_2} = \frac{BL_1L_2}{h/e} \tag{1.15}$$

The numerator of the equation defines the magnetic flux ($\Phi$) generated by the magnetic field $\mathbf{B}$, so the degeneracy of the Landau levels is given by the magnetic flux in terms of the fundamental flux $\Phi_0 = h/e$ [9]. The total amount of electrons flowing through the material ($N$) is given by:

$$N = \nu D = \nu\frac{\Phi}{\Phi_0} \tag{1.16}$$

Where $\nu$ is called Landau filling factor [9]. In the integer quantum Hall Effect, it is precisely the number of filled Landau levels.

The conductance plateaus in the quantum Hall effect is explained by the quantization and degeneracy of the Landau levels. The position of the Fermi level is controlled by the intensity of the magnetic field $\mathbf{B}$. If the Fermi level is placed between Landau levels, the increasing of the Hall voltage raises the electrical current linearly by a fixed proportion

of $\sigma_{xy}$. The electrical current is associated with the number of available electronic states, since it gives the number of conducting electrons per unit of time. If the magnetic field increases, the Fermi level can reach the next Landau level and new electronic states become available for conduction. Thus, the electrical current will raise more rapidly for the same variation of the Hall voltage. The electrical conductivity is then raised by an integer of $e^2/h$.

Since the Hall conductivity does not depend on the geometry [17], it must be related to topological properties of the system. The conductivity in plateaus can be obtained by a thought experiment proposed by Robert Laughlin in 1981 [18]. In the hypothetical situation, the edges of the material are brought into contact forming a cylinder, see figure 1.5. The magnetic field $\mathbf{B}$ points perpendicular to the cylinder surface, which is crossed by the magnetic flux $\Phi$. The Laughlin argument consists of evaluating the electrical charge flowing through the ends of the cylinder during a magnetic flux variation of $\Delta\Phi = \Phi_0$, which induces an electrical field $\mathbf{E}$. The electrical charge transported along the cylinder is obtained from Ohm's law - $\mathbf{J} = \sigma\mathbf{E}$:

$$Q = \sigma_{xy}\Delta\Phi \tag{1.17}$$

In this geometrical configuration, there is a linear relation between the magnetic flux and the magnetic vector potential given by:

$$\Phi = \int \mathbf{A} \cdot d\mathbf{l} = 2\pi R|\mathbf{A}| \tag{1.18}$$

A variation of $\Phi_0$ in the magnetic flux is equivalent of a gauge transformation in the magnetic vector potential of $\mathbf{A} \rightarrow \mathbf{A} + \Phi_0/2\pi R$. The effect of this transformation in equation 1.10 is a translation of the center of the Landau eigenstates by:

$$x_0 \rightarrow x_0 - \frac{\Phi_0}{2\pi RB} \tag{1.19}$$

This translation is equivalent to the length of the cylinder ($L$). Therefore, the electrical charge transported by a variation of $\Phi_0$ in the magnetic flux is $Q = Ne$. For $\Phi = \Phi_0$, equation 1.16 reduces to $N = \nu$. Replacing $Q = \nu e$ and $\Delta\Phi = h/e$ in equation 1.17, the obtained Hall conductivity is exactly $\sigma_{xy} = \nu e^2/h$, with the integer number originated from the Landau filling factor. This integer number is a topological invariant, more precisely, the Chern number of the system [19].

Assuming the Fermi level between Landau levels, i. e, inside the energy gap, the quantum Hall system is equivalent to an insulator. However, it is characterized by a

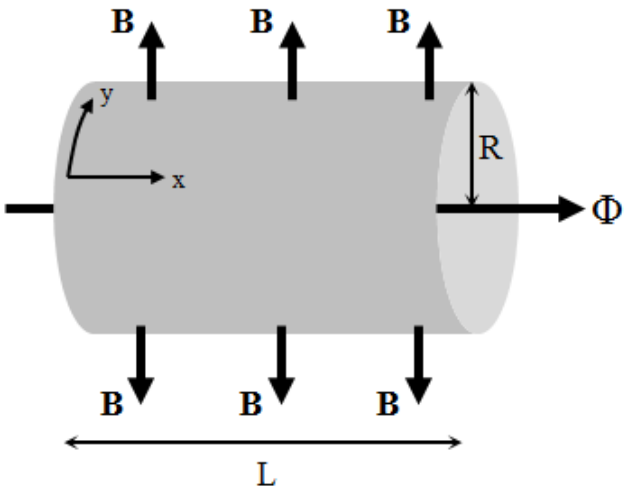


Figure 1.5 – Laughlin experiment. The quantum Hall effect is originated from the magnetic flux $\Phi$ passing through a cylinder of radius $R$ and length $L$. The magnetic field points perpendicular to the cylinder surface. A variation of $\Phi_0$ in the magnetic flux generates a charge transfer of $Q = \nu e$ along the ends of the cylinder, from which follows $\sigma_{xy} = \nu e^2/h$.

topological invariant different from zero. The energy gap must vanish at the interface with the vacuum ($n = 0$), resulting in metallic edges. It means that the longitudinal electrical current is not zero on the edges. Classically, these conducting channels are imagined as the Landau orbits bouncing along the edges, see figure 1.6.

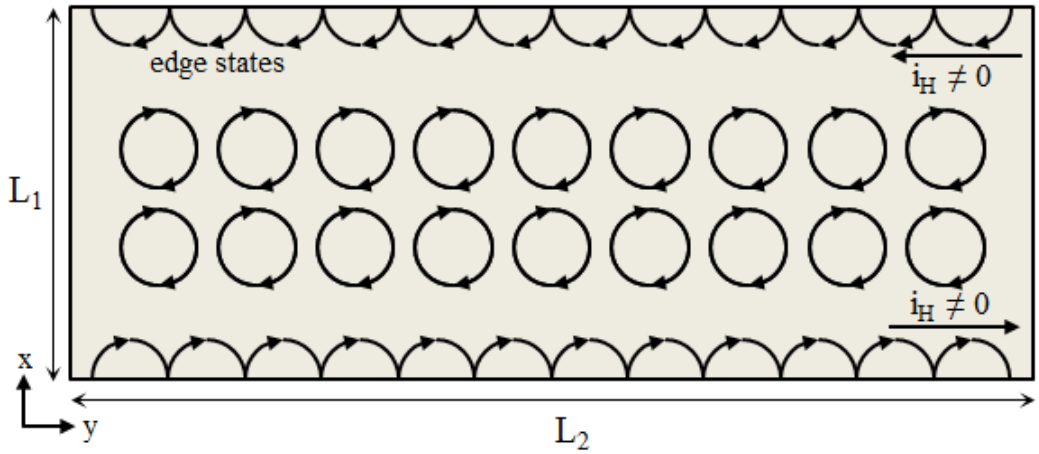


Figure 1.6 – Edge states and the quantum Hall effect. The topological order forces the appearance of longitudinal currents with opposite directions along the edges. Classically, these states are described by Landau orbits bouncing along the edges.

The fractional version of the quantum Hall effect was observed later by Tsui et al. [20]. In that case, the Landau filling factor assumes fractional values ($\nu = \frac{1}{2}, \frac{2}{3}, \frac{1}{5}, \frac{2}{5}, ...$).

This effect is originated from electron-electron interactions that forms quasiparticles carrying a fractional value of the electron charge $e$.

## 1.2 Topological Insulators

### 1.2.1 2D Topological Insulators

Some experiments carried out in the late 19th century demonstrated the existence of the classical Hall effect in the absence of external magnetic fields [21]. An additional contribution to the Hall conductivity is originated from the magnetization of the material [22]. This phenomenon is called anomalous Hall effect. In paramagnetic materials, this effect takes place even in the absence of magnetization and the Hall state is associated with the topology of the bandstructure [23]. The quantum analogues of these phenomena follow the same protocol. The observation of the quantum Hall effect requires breaking of time-reversal symmetry, role played by the presence of external magnetic fields. In 1988, it was proposed the appearance of the quantum Hall effect in the absence of external magnetic fields. The phenomenon should be observed when an electron system is subjected to a periodic magnetic flux, where the total magnetic flux is zero [24]. Later on, this requirement was replaced by the existence of a strong enough spin-orbit coupling [25]. The transversal force created by the spin-orbit coupling separates electrons with opposite spins, forming spin currents along the edges of the material [26].

The quantum spin Hall effect occurs in materials with a strong spin-orbit coupling [27]. Since there is no external magnetic field, time-reversal symmetry is preserved and edge currents are not observed. If taken separately for each electron spin, the system is equivalent to a spinless version of a quantum Hall insulator. The quantized Hall conductivity for each case is $\pm e^2/h$. The charge accumulation on the edges creates edge currents with opposite directions attached to the electron spins that cancel one another, resulting in a total edge current equals to zero. Hall conductance is also zero. Nevertheless, there is an accumulation of electrons with opposite spins on opposite edges. This condition results in a net spin current on the edges of the material and a nonzero spin Hall conductivity ($\sigma_s$) originated from the transversal force created by the spin-orbit coupling, which acts in opposite directions depending on the electrons spin. A comparison between regular quantum Hall effect and quantum spin Hall effect is presented in figure 1.7.

In 2006, Bernevig et al. [28] proposed the realization of a quantum spin Hall state in CdTe/HgTe quantum wells. The system is composed by a thin layer of HgTe surrounded by two layers of CdTe. In the absence of spin-orbit coupling, HgTe and CdTe should present similar bandstructures with p-type valence bands formed by 5p-electrons from Tellurium and conduction bands formed by s-electrons (6s for HgTe and 5s for CdTe). The

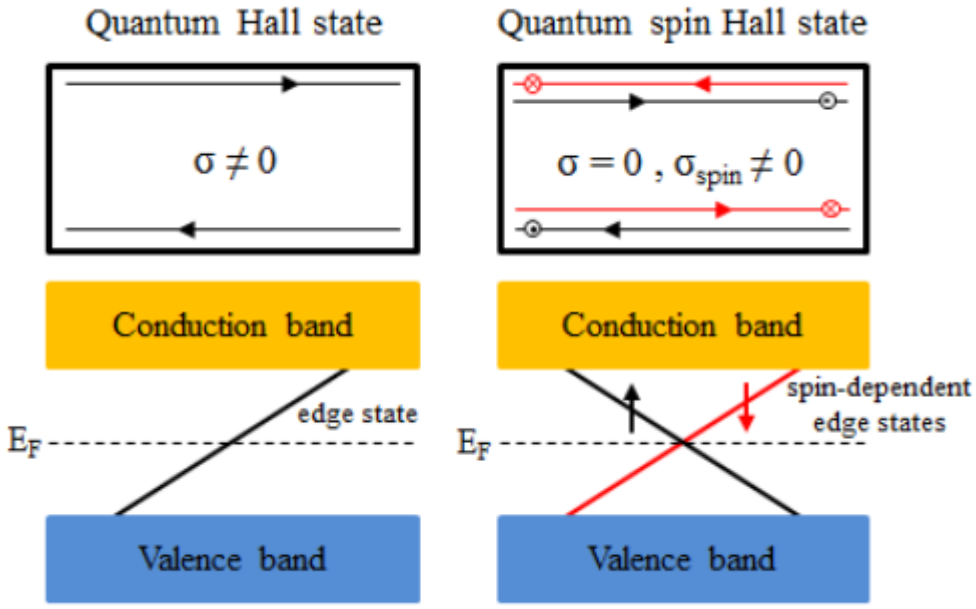


Figure 1.7 – Quantum Hall Effect vs. Quantum Spin Hall Effect. The quantum Hall state is characterized by a non-zero Hall conductivity and metallic states at the edge of the material. The quantum spin Hall state is characterized by zero Hall conductivity and spin-dependent metallic edges states.

spin-orbit coupling lifts the degeneracy of the p-levels and, if strong enough, can cause an electronic band inversion in HgTe, see figure 1.8. In this case, CdTe bandstructure is composed by a p-type valence band and an s-type conduction band, while the HgTe bandstructure has the opposite configuration. The inverted bandstructure topologically distinguishes HgTe and CdTe, so the quantum spin Hall state can be realized in the HgTe layer. The topological phase transition in CdTe/HgTe quantum wells is controlled by the thickness of the HgTe layer, which controls the intensity of the spin-orbit coupling. If the thickness lies below a critical value $d_c$, HgTe is an ordinary insulator with the energy gap separating conduction and valence bands. Above the critical thickness, there is a band inversion and the material becomes a topological non-trivial insulator. From this point, the system performs a quantum spin Hall state, with the appearance of spin-dependent states at the HgTe-CdTe interfaces. The class of materials where this effect is present are called spin Hall insulators or two-dimensional topological insulators.

Since the movement of the spin current is attached to the electron spin, electrons are allowed to travel through just one direction along the interface. This behavior makes edge states robust and protected against backscattering from non-magnetic defects. The topological nature of the quantum spin Hall state suggests the description of the phenomenon is terms of a topological invariant. This topological invariant is called $\mathbb{Z}_2$ invariant [29]. Since there is no Hall conductance in quantum spin Hall effect, the Chern number describing these systems is $n = 0$. Thus, the topological classification of the 2D

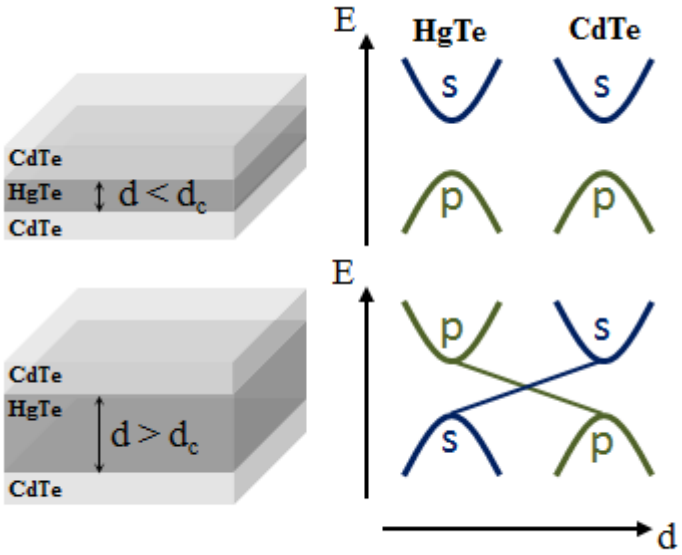


Figure 1.8 – Band inversion in HgTe-CdTe quantum wells. When HgTe thickness is above the critical thickness $d_c$, s-band and p-band are inverted and the system becomes a quantum spin Hall insulator.

topological insulators involves another number for the $\mathbb{Z}_2$ invariant, related to the concept of time-reversal symmetry ($\mathcal{T}$). $\mathcal{T}$-symmetry is represented by an anti-unitary operator $\Theta$ and a $\mathcal{T}$-invariant Bloch Hamiltonian must satisfy:

$$\Theta\ \hat{H}(\mathbf{k})\ \Theta^{-1} = \hat{H}(-\mathbf{k}) \tag{1.20}$$

There are two topological classes of time reversal invariant bandstructures in two dimensions, with the topological invariant assuming two possible values, $\nu = 0$ or $\nu = 1$. The determination of the $\mathbb{Z}_2$ topological invariant $\nu$ is provided by the identification of the points in the 2D Brillouin zone where the crystalline momentum is invariant to time-reversal transformations; i. e, where $\mathbf{k}$ is equivalent to $-\mathbf{k}$. These points are called time-reversal invariant momentum (TRIM) points. The anti-unitary operator $\Theta$ defines a unitary matrix $W$ with coefficients given by:

$$W_{mn} = \langle u_m(\mathbf{k})|\Theta|u_n(-\mathbf{k})\rangle \tag{1.21}$$

From where the following quantity is defined for each TRIM point $\Gamma_i$:

$$\delta_i = \frac{\mathrm{Pf}[W(\Gamma_i)]}{\sqrt{\mathrm{Det}[W(\Gamma_i)]}} = \pm 1 \tag{1.22}$$

Which is equivalent to determine the signal of the determinant of matrix $W(\Gamma_i)$. The $\mathbb{Z}_2$ invariant $\nu$ is obtained from:

$$(-1)^{\nu} = \prod_{i=1}^{4} \delta_i \tag{1.23}$$

The determination of the topological invariant can become extremely complicated depending on the bandstructure and the absence of other types of symmetries in the material. A simple method consists of determine the change of the $\mathbb{Z}_2$ invariant at the interface between two insulators. For spin-1/2 particles, all eigenstates of a $\mathcal{T}$-invariant Hamiltonian are at least twofold degenerate, property known as Kramers degeneracy [30]. The electronic states are degenerate at the TRIM points due to time-reversal invariance, but the degeneracy is lifted by the spin-orbit coupling away from these points, see figure 1.9. The change of the $\mathbb{Z}_2$ invariant $\Delta\nu$ is obtained counting the number of times the Kramers pairs cross the Fermi level of the material. If the number of crossings is even, $\Delta\nu = 0$, it means that the edge is formed by two topologically equivalent insulators. The Kramers pairs are not edge states and an insulator state is obtained positioning the Fermi level inside a band gap. If the number of crossings is odd, $\Delta\nu = 1$ and the insulators are topologically distinct, which classifies the Kramers pairs crossing the Fermi level as protected metallic edge states.

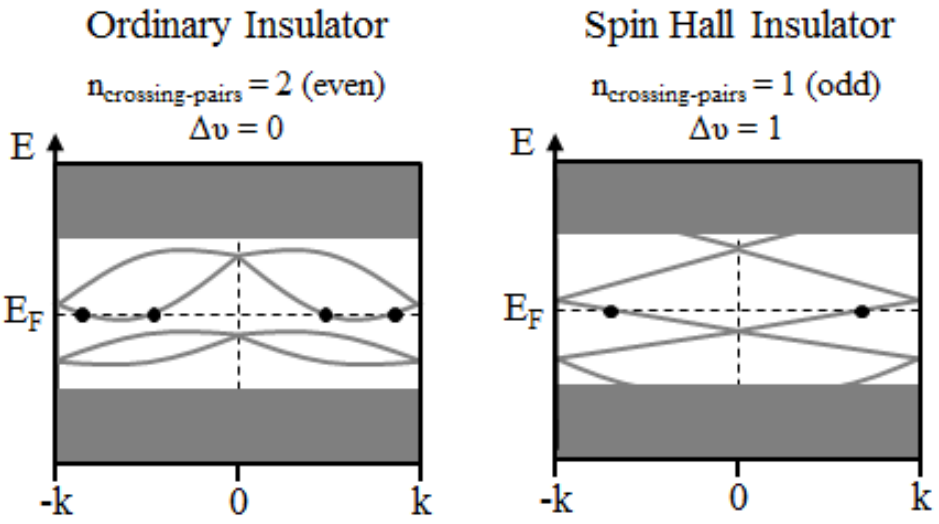


Figure 1.9 – Topology of Edge states. The topology of the edge bandstructure classifies the topology of the materials forming the interface. Outside TRIM points, spin-orbit coupling lifts the degeneracy of Kramer's pairs. The topology is obtained from the number of times the Fermi Level is crossed.

### 1.2.2 3D Topological Insulators

The quantum spin Hall effect is responsible for the appearance of the topological edge states in two-dimensional topological insulators. Those materials are simply characterized by a single $\mathbb{Z}_2$ invariant associated with the degeneracy of the Kramers pairs and how many times the Fermi level is crossed. In 3D topological insulators, the formation of the topological state involves aspects there are not a simply extension of the two-dimensional case. The topological state is composed by 2D surface states that could or could be topologically protected [9]. In summary, 3D topological insulators are materials that are insulators in the bulk, but metallic on the surface.

A 3D topological insulator is characterized by four $\mathbb{Z}_2$ topological invariants ($\nu_0$, $\nu_1$, $\nu_2$, $\nu_3$), each number assuming values of 0 or 1 [31]. These numbers are obtained in a similar manner to the 2D $\mathbb{Z}_2$ invariant $\nu$ in equation 1.23. Differently from 2D topological insulators, there are 8 points of time-reversal invariant momentum (TRIM) in the first Brillouin zone of three-dimensional materials, see figure 1.10. The $\nu_0$ index is called strong invariant and it classifies topological insulators in two classes: weak topological insulators ($\nu_0 = 0$) and strong topological insulators ($\nu_0 = 1$). Its determination involves the $\delta_i$ quantities calculated for each 8 TRIM points. The strong invariant $\nu_0$ is obtained from:

$$(-1)^{\nu_0} = \prod_{i=1}^{8} \delta_i \tag{1.24}$$

The other three indexes are called weak invariants and they are associated with the projections of the three lattice directions of the crystal, forming time-reversal invariant planes, see figure 1.10. Each weak invariant is obtained from TRIM points of different planes. The $\delta_{[n_1 n_2 n_3]}$ quantities are labeled by a discrete vector expressing the TRIM point $\Gamma_i = \nu_1 \mathbf{b}_1 + \nu_2 \mathbf{b}_2 + \nu_3 \mathbf{b}_3$, where $\mathbf{b}_1$, $\mathbf{b}_2$ and $\mathbf{b}_3$ are the primitive reciprocal lattice vectors. The weak invariants $\nu_{i=1,2,3}$ are given by:

$$(-1)^{\nu_i} = \prod_{n_i=1, n_{j\neq i}=0,1} \delta_{[n_1,n_2,n_3]} \tag{1.25}$$

Kramers degeneracy also performs an important role in the three-dimensional bandstructure. The points where the electronic states are degenerate are named Dirac points. Out of this point, the degeneracy lifted by the spin-orbit coupling creates a cone structure in two dimensions, named Dirac cone [32]. The strong invariant $\nu_0$ determines the robustness of the topological surface states in a manner that for the surface Brillouin zone, the number of Dirac cones crossing the Fermi level classifies the topological state as stronger or weak. If there is an odd number of Dirac cones crossing the Fermi level, $\nu_0 = 1$ and the system is classified as a strong topological insulator. For the case of an even number of Dirac cones

crossing the Fermi level, $\nu_0 = 0$ and the material is a weak topological insulator. When all four invariants are equal to zero, the material is an ordinary insulator.

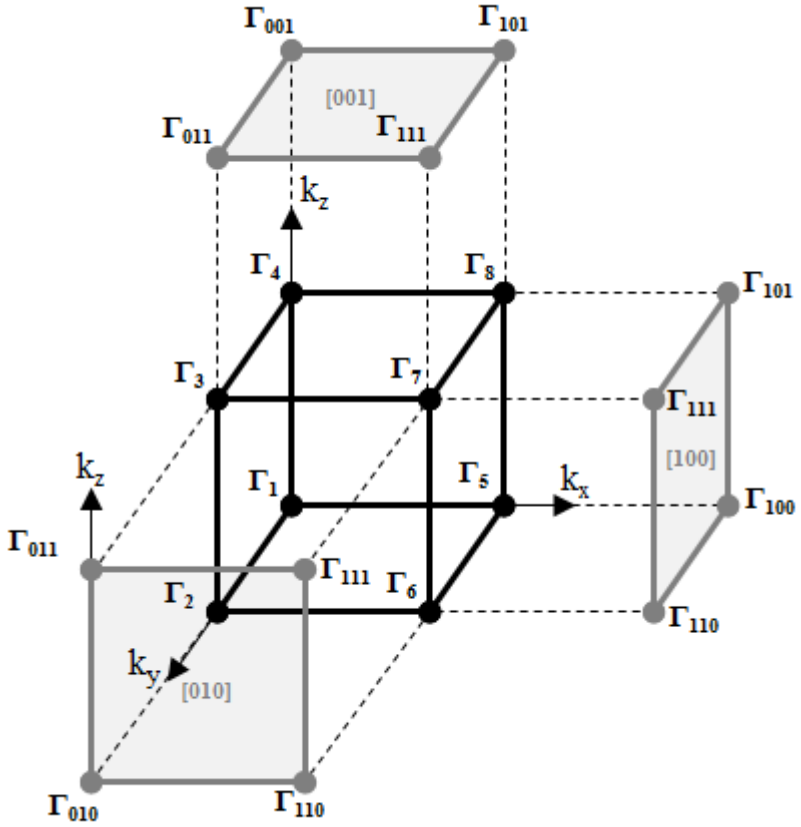


Figure 1.10 – Points of time-reversal invariant momentum (TRIM). In 3D crystals, the first Brillouin zone has 8 point of time-reversal invariant momentum ($\mathbf{k} = -\mathbf{k}$). $\Gamma_1 = (0, 0, 0)$ is the Γ-point. The projection on the reciprocal lattice vectors defines the TRIM planes where $\nu_1$, $\nu_2$ and $\nu_3$ are determined.

The distinction between strong and weak topological insulator has an important significance due the connection between momentum and spin of the electrons. Time-reversal symmetry creates a sort of chirality on the surface states, called spin texture. The 1D edge states in a 2D topological insulator are formed by states locked to the electron spins. In three dimensions, the 2D surface states form a right or left-hand spin orientation for the Dirac cones. The robustness of the surface states are linked to the spin texture. If there is an odd number of Dirac cones, backscattering is forbidden because there is no state with an opposite spin texture for the electrons; differently from what occurs with an even number of Dirac cones. In the strong topological phase described by $\nu_0 = 1$, the presence of surface states is guaranteed by the odd number of Dirac cones. If the Fermi level lies inside the bulk bandgap, it should have at least one electronic state crossing it. Weak topological insulators do not have the same assurance in relation to the presence of surface states crossing the Fermi level. The three weak invariants ($\nu_1$, $\nu_2$ and $\nu_3$) are associated to

the projection of the TRIM points into the three reciprocal lattice directions (100, 010 and 001), respectively. These projections define the symmetry of the 2D Fermi surface at each direction. The associated planes can be interpreted as 2D layers of quantum spin Hall states stacked in the respective lattice direction. The presence of protected surface states is defined separately for each crystallographic plane, concluding that the observation of topological phases depends on the sample orientation. The robustness to defects is linked to the position of the defects in the crystallographic matrix. This feature is what makes this class named weak topological insulators, as the topological protection of the surface states is not stable and resilient as the strong phase.

Strong and weak topological insulators also differs on how they are constructed. The easiest construction of a 3D topological insulator consists on the stacking of 2D quantum spin Hall insulator layers. The edge states on each layer form a chiral surface coating along the stacking direction and the robustness of these states depends on the coupling among layers. For weakly coupled layers, the surface states intersect the Fermi level an even number of times. This state is referred as a weak topological insulator, and has $\nu_0 = 0$. The weak invariants $(\nu_1, \nu_2, \nu_3)$ index the reciprocal lattice vector associated with the 2D $\mathbb{Z}_2$ invariant of the original quantum spin Hall state for each referred reciprocal lattice direction. The formation of the strong topological phase does not have the origin on 2D quantum spin Hall insulators. In a strong topological insulator, the surface states form a distinct phase that could be described as topological metal. The spin-momentum locking of electrons creates an electronic structure that can be imagined as two spinless ordinary metals.

The first topological insulator was experimentally realized in 2008 [33]. The semiconductor alloy $Bi_{1-x}Sb_x$ was predicted to render a topological phase in the particular range of $0.07 < x < 0.22$. The mechanism responsible for the non-trivial character is a band inversion caused by the variation of Bi and Sb concentrations. A phase diagram is presented in figure 1.11 with a representation of the four bands that forms the bandstructure close to the Fermi level: $T$, $L_s$, $L_a$ and $H$. For values below $x = 0.04$, the system is a semiconductor with the bandgap formed by valence ($L_a$) and conduction ($L_s$) bands and the bandgap decreases as the Sb concentration is increased. The bandgap vanishes at $x = 0.04$ and reopens with inverted bands until $x = 0.07$. At this value, the $T$ band touches the conduction band and the systems enter in a strong topological phase, which remains until $x = 0.22$ where the upcoming band $H$ touches the conduction band $L_a$, and the systems becomes an ordinary semiconductor with the bandgap increasing as the Sb concentration increases. The observation of the topological surface states was done using high-resolution angle-resolved photoemission spectroscopy, where five Dirac cones were reported in the first Brillouin zone of the 2D Fermi surface. The odd number classifies $Bi_{1-x}Se_x$ as a strong topological insulator at the $0.07 < x < 0.22$ range.

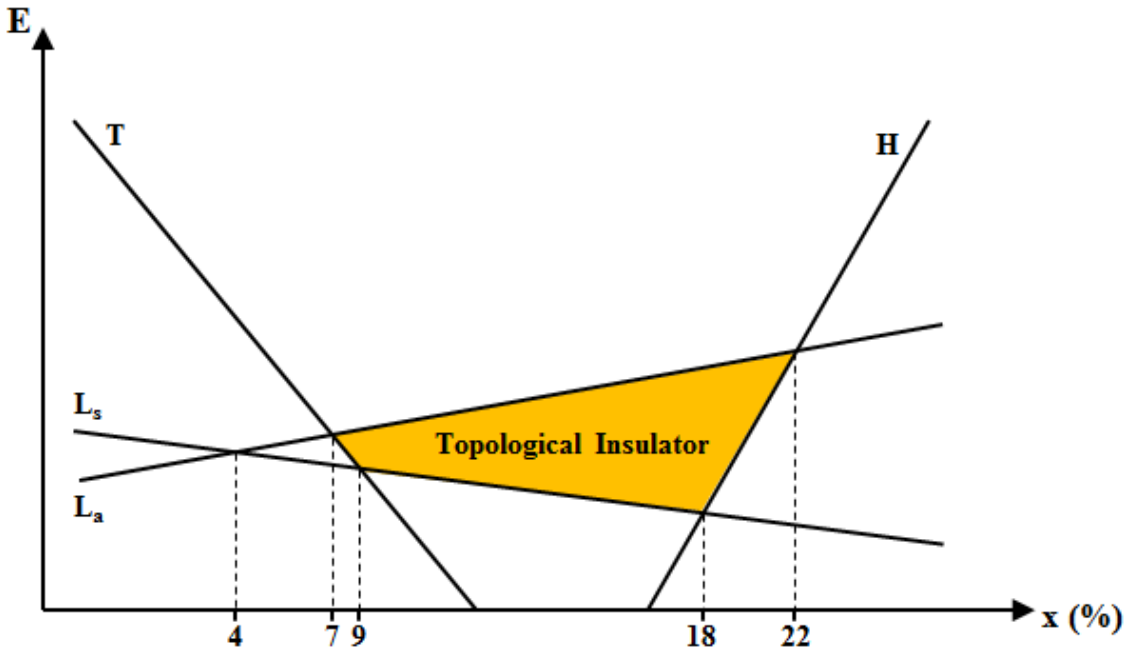


Figure 1.11 – $Bi_{1-x}Sb_x$ phase diagram. The diagram shows the relative positions of the electronic bands ($L_s$, $L_a$, $T$ and $H$) as function of Sb concentration. The topological insulator phase is observed in the interval $0.07 < x < 0.22$, depending on the position of the Fermi level.

A few years later, the Bi-Chalcogenide family emerged as the most promising class of topological insulators [34]. The stoichiometric crystals $Bi_2Se_3$, $Bi_2Te_3$ and $Sb_2Te_3$ were identified as strong topological insulators holding surface states with a single Dirac cone centered at the Γ-point. The relatively large bandgap (from 0.1 to 0.3 eV) makes these materials promising to applications at room temperature, since the topological state is observed without the requirement of low temperatures. In figure 1.12, a high-resolution ARPES measurement of a $Bi_2Se_3$ single crystal is presented. It was measured with photon energy of 21.2 eV at the Brazilian Synchttron light laboratory (LNLS) in Campinas/SP. The energy-momentum map shows the surface band dispersion providing a clear evidence of surface states in 3D topological insulators. Bi-Chalcogenide family are called the second generation of 3D topological insulators and they all present the associated topological features: 2D topologically-protected metallic surface states with a single Dirac-cone at Γ, conduction without dissipation, robustness to non-magnetic defects and spin-momentum polarization. Another main advantage of these materials is that they are stoichiometric, making them easy to produce with high purity. They present the same basic atomic structure: rhombohedral lattice formed by stacking of quintuple-layers with P-C-P-C-P atoms, where P is the pnictogen atom (Bi or Sb) and C is the chalcogen atom (Se or Te). The quintuple-layers are bounded by weak van der Waals forces what makes them easily cleavable to spectroscopy experiments.

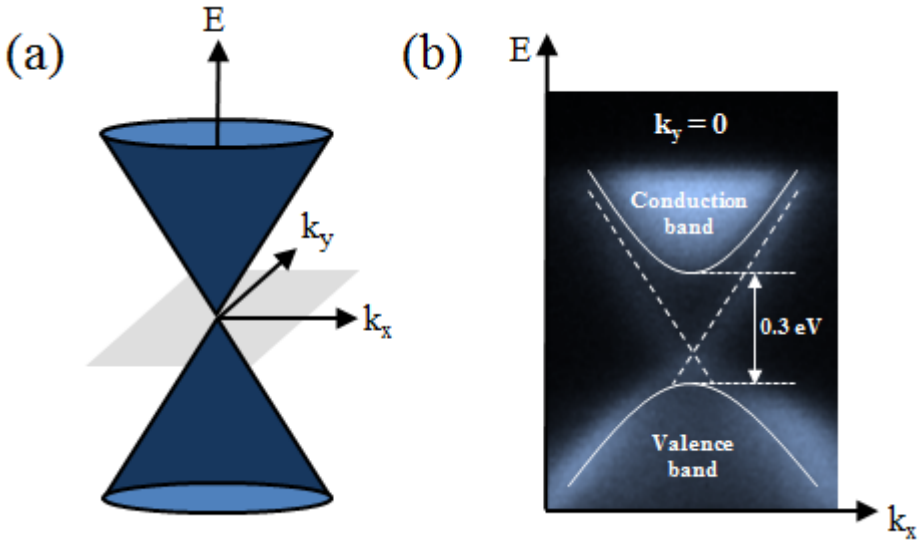


Figure 1.12 – $Bi_2Se_3$ with a single Dirac cone at Γ. (a) Three-dimensional representation of the Dirac cone. (b) Energy-momentum relation of $Bi_2Se_3$ obtained by Angle-resolved Photoemission Spectroscopy, evidencing the surface states forming the Dirac cone, marked by dashed lines inside the 0.3 eV bulk bandgap.

## 1.3 Topological Nodal Semimetals

### 1.3.1 Weyl and Dirac Semimetals

The topological classification of the bandstructures is extended beyond the concept of topological insulators. In fact, new topological phases of matter can emerge in systems where an energy gap is not present [35]. The discovery of the topological nodal semimetals opened a new branch on the study of topological band theory. These materials are characterized by a finite number of points where conduction and valence touch one another [36]. The band touching points are called Weyl nodes and they are robust and protected by crystal lattice symmetries. The interest about those materials relies on the fact that the energy dispersion in the region near a Weyl node is linear and it can be described as massless fermions with definite chirality, known as Weyl fermions [37]. Depending on the type of degeneracy at the Weyl node, materials are classified as topological Weyl semimetals or topological Dirac semimetals [38].

In 1928, Paul Dirac created an equation to describe elementary spin-1/2 particles in a relativistic quantum mechanical treatment [39]. The general form of the Hamiltonian is:

$$H = c\,\mathbf{p}\cdot\alpha + mc^2\beta \tag{1.26}$$

Where $\alpha_i$ and $\beta$ are known as Dirac matrices and $c$ is the velocity of light. In three dimensions, the solution is given by four-component wavefunctions. The 4x4 Dirac matrices are obtained from tensor products of the Pauli matrices $\sigma_i$ ($\sigma_i = \sigma_x, \sigma_y, \sigma_z$) and the identity matrix ($I$):

$$\alpha_i = \sigma_x \otimes \sigma_i \tag{1.27a}$$

$$\beta = \sigma_z \otimes I \tag{1.27b}$$

The eigenvalues of equation 1.26 are given by:

$$E_{\pm} = \pm\sqrt{m^2c^4 + p^2c^2} \tag{1.28}$$

Each of these eigenvalues is twofold degenerate, resulting in a total of four eigenstates. The positive energy corresponds to the two states of an electron: spin up and down; while the negative energy is associated to spin up and down states of a positron. In condensed matter physics, the negative energy is associated with electron holes.

One year after Dirac enunciates his equation, Hermann Weyl proposed a modification of the equation where the mass term is removed (m = 0) [40]. The modification leads to the decoupling of equation 1.26 into two independent 2x2 equations:

$$H_{\pm} = \pm v\ \mathbf{p} \cdot \sigma \tag{1.29}$$

These equations describe massless fermions with definite chirality. During more than 90 years, they had not been observed. In the last decade, Weyl fermions were observed as low-energy excitations in the electronic bandstructures of topological semimetals [41]. The linear dispersion of the electronic bands around a Weyl node is described by the Weyl equations in equation 1.29. Each Weyl node host Weyl fermions with a definite chirality. For each chiral equation, there are two eigenvalues given by $E = \pm v|\mathbf{p}|$ that are degenerated in $\mathbf{p} = 0$. The separation of chiral fermions with opposite chirality at different Weyl nodes originates an interesting property of Weyl semimetals. The topological classification of bandstructures involves the concept of Berry curvature ($\mathcal{F}$) discussed before, which defines the topological entanglement between conduction and valence bands. Weyl nodes represent singularities in the bandstructure, acting as monopoles of Berry curvature [42]. Depending on the chirality, a Weyl node is a source (+ chirality) or a sink (− chirality) of Berry curvature. They always appear in pairs; otherwise, the Berry flux becomes divergent. The

chirality of the monopoles is defined as the Berry curvature flux ($\mathcal{N}$) trespassing a sphere that encloses the Weyl node:

$$\mathcal{N} = \frac{1}{2\pi}\int_S \mathcal{F}\cdot dS = \pm 1 \tag{1.30}$$

This flux has the form of the Chern number defined in equation 1.6. Two Weyl nodes with opposite chirality can be disposed together to form a Dirac node, in that case, the associated Chern number is zero and there is no monopole of Berry curvature. A Dirac node has fourfold degeneracy.

Dirac and Weyl semimetals indicate a class of materials that presents low energy excitations consisting of degenerated quasiparticles with distinct chirality and linear energy dispersions. Weyl semimetals require breaking of either time-reversal symmetry ($\mathcal{T}$) or lattice inversion symmetry $\mathcal{P}$ [43]. The differentiation between these two scenarios is done by counting the number of Weyl nodes present in the material. If only $\mathcal{P}$-symmetry is broken, $\mathcal{T}$-symmetry guarantees that a Weyl none at certain momentum $\mathbf{k}$ has a counterpart of momentum $-\mathbf{k}$ with the same chirality. As the total Berry flux should be conserved, other two Weyl nodes with opposite chirality must be present. So, a Weyl semimetal with broken $\mathcal{P}$-symmetry has a number of Weyl nodes that is multiple of four, while the other case describes Weyl semimetals with broken $\mathcal{T}$-symmetry. If both symmetries are present, there are pairs of degenerate Weyl nodes forming a fourfold degenerate Dirac node and the system is a topological Dirac semimetal [44]. In other words, a topological Dirac semimetal can be understood as the combination of two Weyl semimetals. The Dirac/Weyl cones from each case are presented in figure 1.13.

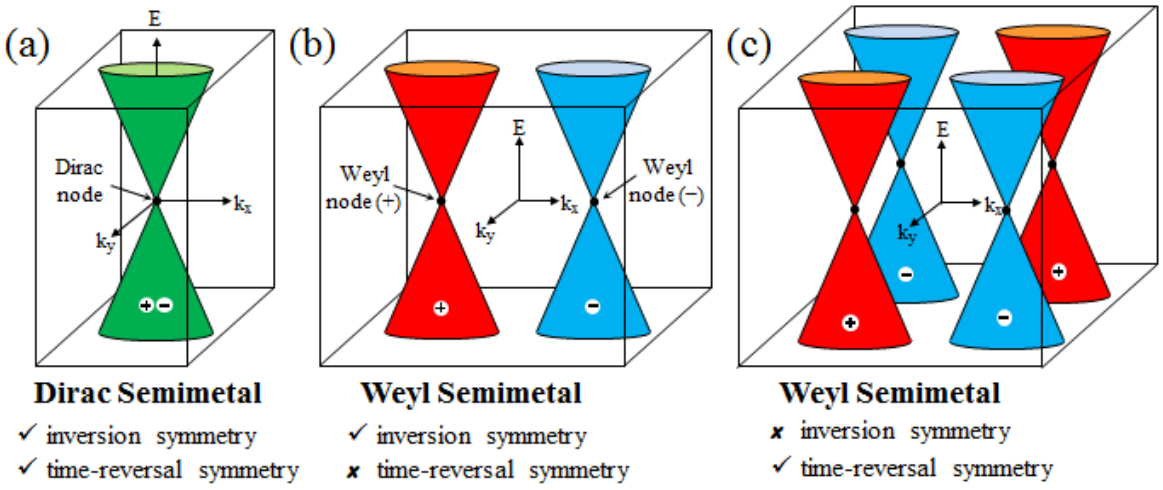


Figure 1.13 – Dirac and Weyl cones at time-reversal ($\mathcal{T}$) and inversion ($\mathcal{P}$) symmetry. (a) Dirac semimetal with one fourfold degenerated Dirac point. (b) Weyl semimetal with broken $\mathcal{T}$-symmetry. (c) Weyl semimetal with broken $\mathcal{P}$-symmetry.

The topological nature of the band touching points is manifest on the appearance of surface states connecting Weyl nodes with opposite chirality. In topological insulators, the surface states form a 2D Dirac cone that connects bulk bands with different topology. They intersect the Fermi level forming Fermi circles, except if the Fermi level is exactly at the Kramers degenerate point. In Weyl semimetals, the connection between Weyl nodes is associated with an unclosed line of constant energy observed on the Fermi surface of the material. These constant energy lines originated from the projections of a plane that connects bulk Weyl cones on the Fermi surface and are known as Fermi arcs [45]. If the Weyl nodes are positioned at a different energy position ($E \neq E_F$), the Fermi arcs appears tangentially connecting the pairs of Fermi circles formed by the 2D projection of the Weyl cones, see figure 1.14.

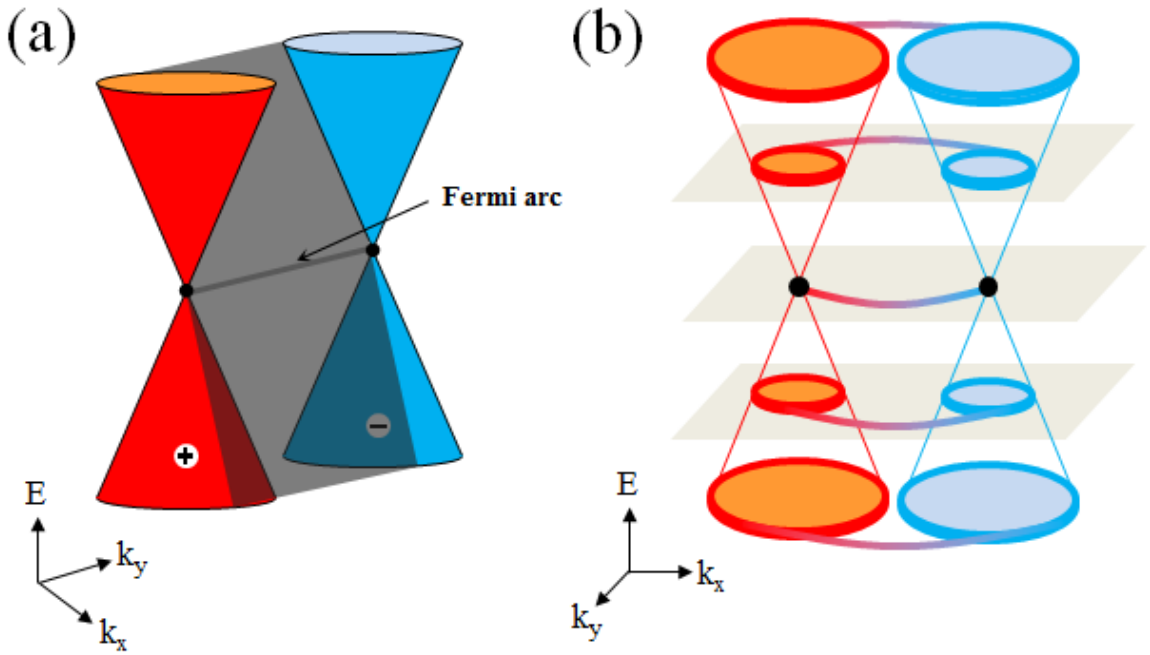


Figure 1.14 – Topological Fermi arcs. Fermi arcs appear as constant-energy states connecting Weyl nodes with opposite chirality at the Fermi surface. (a) Fermi arc defined by the plane tangent to the Weyl cones. (b) Projection of the Fermi arc on the Fermi surface for different values of Fermi energy.

The appearance of Fermi arcs is directly associated with the fact that Weyl nodes are sources and sinks of Berry flux. Consider an imaginary plane placed between two Weyl nodes with opposite chirality, see figure 1.15. There is a non-zero Berry flux crossing it, so the imaginary plane has a Chern number $n = 1$. Outside the Weyl nodes, the material presents a band gap, so the imaginary plane can be imagined as projected 2D Hall insulator since it has non-zero Chern number. The edge states associated with imaginary planes between Weyl nodes is what creates the Fermi arc, which connects the projection of the Weyl nodes on the Fermi surface [38]. Other physical consequences of the topology in Weyl semimetals include the chiral anomaly [46] and the anomalous Hall effect [47].

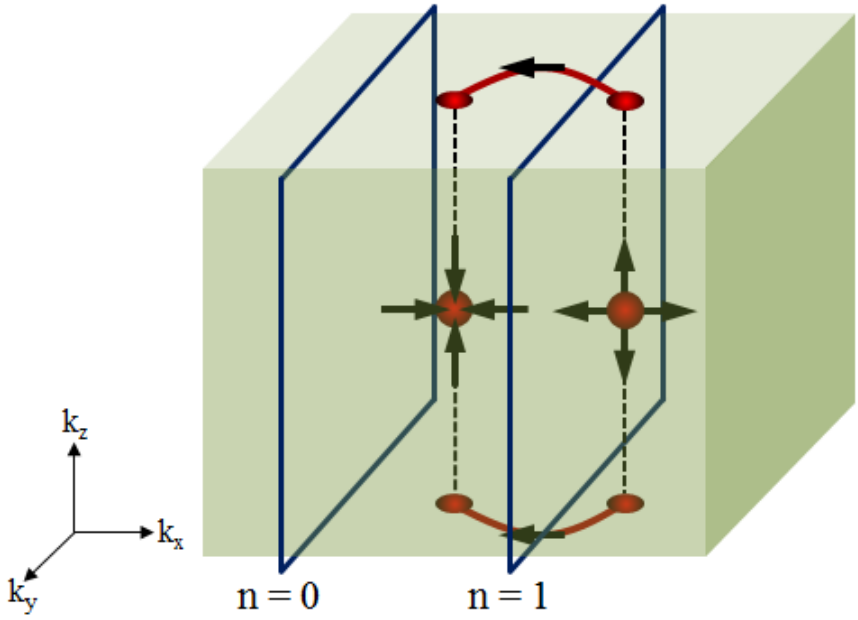


Figure 1.15 – Berry flux through Weyl nodes. The non-zero Berry flux passing through imaginary planes between Weyl nodes defines topological states associated with a Chern number $n \neq 0$. These topological states are represented by Fermi arcs in the projected Fermi surface.

The first experimental realization of a topological Weyl semimetal was performed in 2015 with the semimetal TaAs [48]. Fermi arcs were observed by high-resolution ARPES supported by theoretical considerations. Ab initio calculations were employed to determine and address the gapless touching points and reported twelve pairs of Weyl points inside the 3D Brillouin zone, all confirmed by Fermi arcs observed in ARPES measurements. TaAs is a stoichiometric material representative of the transition metal monopnictide family, which includes other materials that were also successfully reported as Weyl semimetals: TaP [49], NbP [50] and NbAs [51]. Recently, a new type of Weyl semimetals has been observed in transition metal di-chalcogenides $MoTe_2$ [52] and $WTe_2$ [53]. In those materials, the Weyl cone is tilted and the Weyl nodes are the touching points between electron and hole pockets in the Fermi surface. Their layered nature of these compounds makes them ideal candidates for the fabrication of devices holding the exotic features of a Weyl semimetal [54].

### 1.3.2 Axion Insulators

The characterization of an axion insulator is associated with existence of axion particles in the context of condensed matter physics. In 1997, Peccei and Quinn proposed the existence of an elementary particle to solve the charge-parity problem in quantum chromodynamics [55]. The associated axion field is introduced as an additional term in

the Maxwell's equation that couples magnetic and electric fields [56]. Until today, this hypothetical particle has not been observed. Therefore, low-energy excitations in topological materials were predicted to create an axion term in the Hamiltonian [57]. Materials where these excitations are present receive the name of axion insulators. Topological field theory predicts the existence of axion excitations as a coupling into the electromagnetic field given by the axion field ($\theta$):

$$\nabla \cdot \mathbf{E} = 4\pi\rho - \frac{\alpha}{\pi}(\nabla\theta) \cdot \mathbf{B} \tag{1.31a}$$

$$\nabla \times \mathbf{B} = \frac{4\pi}{c}\mu_0\mathbf{J} + \frac{1}{c}\frac{\partial \mathbf{E}}{\partial t} + \frac{\alpha}{\pi}\left[\frac{1}{c}\mathbf{B}(\frac{\partial\theta}{\partial t}) + (\nabla\theta) \times \mathbf{E}\right] \tag{1.31b}$$

Where $\alpha$ is the fine structure constant. It is clear from the expression that only spatial and temporal changes in $\theta$ induce observable effects. In time-reversal topological insulators, the axion field leads to a linear coupling between magnetic and electric fields, inducing electric polarization when a magnetic field is applied and a magnetization when an electric field is applied [57]. This effect is known as magnetoelectric effect [58]. An axion insulator has a quantized magnetoconductance associated with the axion angle $\theta$ that assumes integer values of $\pi$ in the topological state [57]. This quantized value determines a topological classification for insulators that is equivalent to the $\mathbb{Z}_2$ invariant in three dimensions. Since time-reversal symmetry is broken, axion insulators do not have protected surface states.

The axion insulator was first predicted in magnetic systems as iridates [59] and magnetically-doped topological insulators [60]. It was a few years after the discovery of topological semimetals that axion electrodynamics were proposed to describe the electromagnetic response in topological Weyl semimetals [61]. Weyl semimetals are a topological phase characterized by gapless bulk states with chiral symmetry and topological Fermi arcs connecting points were conduction and valence bands touch one another (Weyl nodes). The formation of a charge-density wave (CDW) can destroy the intrinsic chiral symmetry, opening an energy gap at the Weyl nodes and converting the otherwise bulk semimetal into a bulk insulator. The phase fluctuations of the CDW couple directly to an axion field. This gap-opening mechanics should be observed at any Weyl semimetal that exhibits a charge-density wave coupling to the spacing between Weyl nodes. The CDW instability turns Weyl semimetals into axion insulators.

The first experimentally realization of an axion insulator was reported in 2019 by transport measurements in quasi-1D $(TaSe_4)_2I$ [62]. This compound is a Weyl semimetal at room temperature and the formation of a charge-density wave at low temperatures induces the opening of the bandgap at the Weyl nodes. The phase of this charge-density wave can be identified as a contribution to the axion field and its effect is observed in magnetotransport measurements.

# Chapter 2

# Basics of Angle-resolved Photoemission Spectroscopy

## 2.1 Photoemission Spectroscopy

Photoelectric emission (or photoemission) is the process when electrons are ejected from a material illuminated by a light source [63]. This process only happens under special circumstances and the ejected electrons are called photoelectrons. The experimental techniques based on photoemission are called Photoelectron Spectroscopies. The following sections have the purpose of gather the most important concepts related to the photoemission process and familiarize the reader with the technical analysis of a photoemission spectroscopy data, especially of Angle Resolved Photoemission Spectroscopy (ARPES).

### 2.1.1 The photoelectric Effect

The photoelectric effect was first investigated in 1887 by Heinrich Hertz [64] during experiments with a spark gap generator. He observed the increasing of the generated sparks when the device is illuminated. Later on, controlled experiments were carried out to investigate this phenomenon [65, 66]. Consider two cleaned metallic plates placed inside a sealed vacuum chamber and connected by a wire, see figure 2.1. The photoemission process occurs when one plate is illuminated by a light source. Electrons from the illuminated plate purchase kinect energy from the light source, some of them having enough energy to reach the other plate. Thus, an electrical current is detected by the ammeter. A variable power supply with the negative pole connected to the non-illuminated plate generates an electric field that start to repel the photoelectrons. In this case, only electrons with higher kinect energy reach the non-illuminated plate. If the power supply voltage is increased, fewer electrons reach the non-illuminated plate and the current measured by the ammeter is reduced. For a sufficiently high voltage, the current vanishes. In the zero-current regime,

the maximum kinect energy of the photoelectrons is obtained multiplying the cut-off voltage by the electron charge.

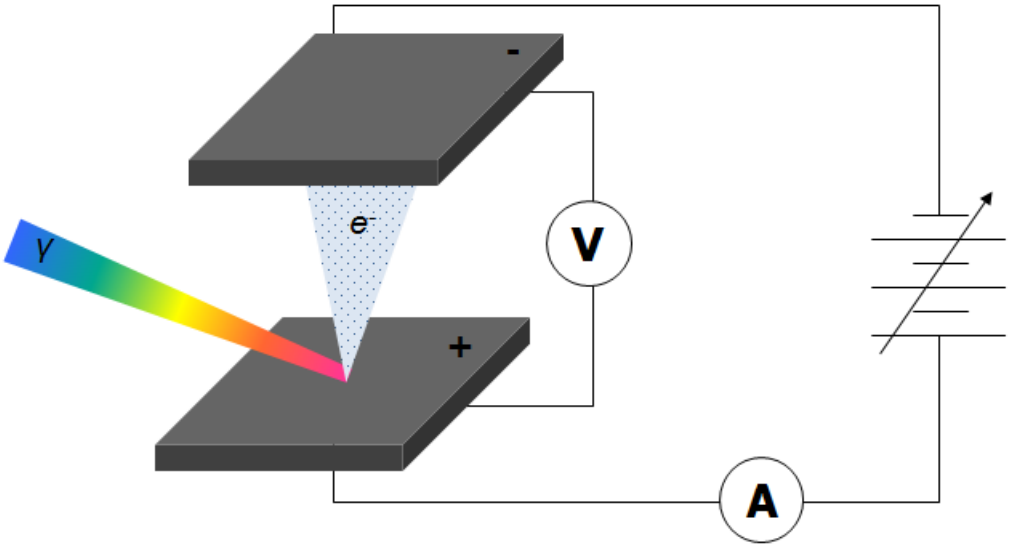


Figure 2.1 – The photoelectric experiment. A light source is used to drag out electrons from a metallic plate and a power supply controls the electrical current flowing through the circuit. When the electrical current vanishes, the maximum kinect energy of the photoelectrons is obtained reading the voltmeter.

Classical electrodynamics predicts that the kinect energy of the photoelectrons should increase with the intensity of the indecent light beam [7], which was not observed. An increment on the maximum kinect energy was only observed when the light source was replaced by another with higher frequency. Later experiments were carried out by many scientists to study this unforeseen situation [66, 67]. They observed a linear dependency between the maximum kinect energy of the photoelectrons and the light frequency, with a cutoff frequency from where no electrons are ejected from the material. This frequency is called threshold frequency and it is different for different materials, see figure 2.2. The photoelectric effect was successful explained by Albert Einstein in 1905 [68] using a quantum mechanical treatment for the light-matter interaction. In that approach, light is described by massless particles called photons. The energy of the photon is obtained multiplying the light frequency ($\nu$) by the Planck's constant ($h = 6.63 \times 10^{-34}\ J \cdot s$). The linear dependency of the maximum kinect energy with the photon energy is given by:

$$K_{max} = h\nu - \phi \tag{2.1}$$

The difference between the photoelectron kinect energy and the photon energy defines the

work function of the material ($\phi$), which is labeled for an enormous quantity of materials nowadays [69].

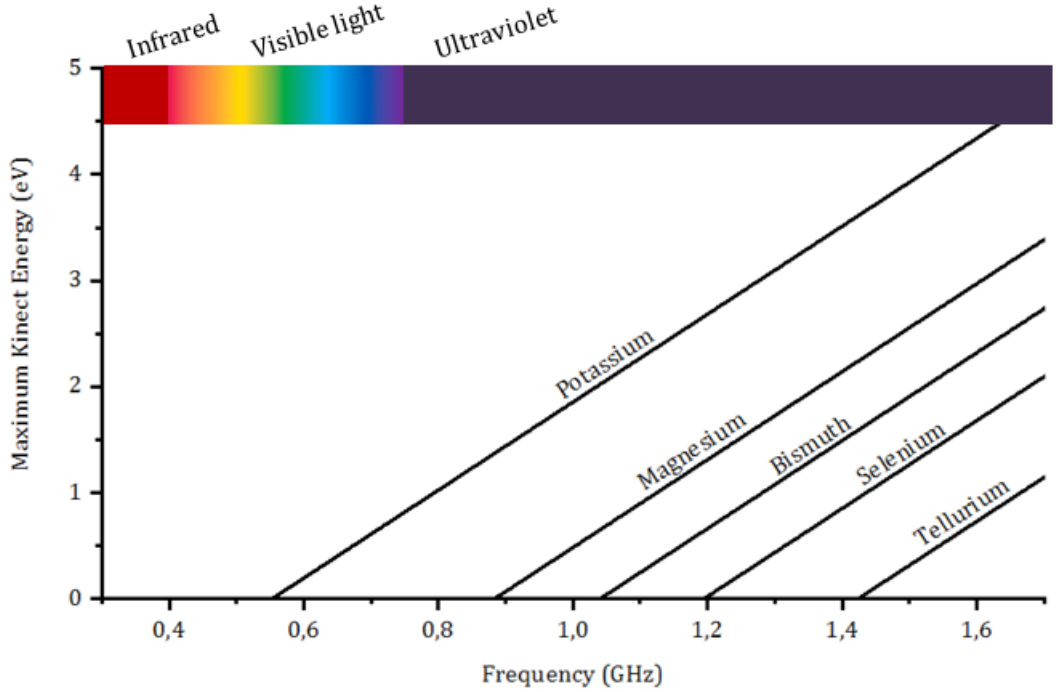


Figure 2.2 – Maximum kinect energy vs. light frequency for different materials.

### 2.1.2 X-Ray Photoelectron Spectroscopy

The linear dependency in equation 2.1 describes the electrons weekly bounded to the material. A complete description including photoelectrons with any values of kinect energy is given by:

$$E_{kin} = h\nu - \phi - |E_B| \tag{2.2}$$

Which relates the kinect energy of the photoelectrons ($E_{kin}$) to the binding energy ($E_B$) of the electrons inside the material. This equation is extremely important for spectroscopy experiments. It represents the energy conservation in the photoemission process. The information about the energy of the electrons inside a material is obtained by the measurement of the kinect energy of the photoelectrons. This relation is explored in details in figure 2.3. The energy of the last occupied state of the sample is called Fermi energy ($E_F$) and it is conventionally set to zero. The vacuum energy ($E_{vac}$) is the minimum energy that an electron must have to escape the material. The difference between theses energies is the work function ($\phi$). The photoemission spectrum of a sample is constituted by two parts: the core levels and the valence band [63]. The spectrum of the core levels provides

information about the chemical composition of the material, as it is related to the electrons that are bounded to the atoms. The spectrum of the valence band provides information about the electrons that are attached to the crystalline structure. These electrons form the bandstructure of the materials and they are responsible for electrical and thermal conductivity [5].

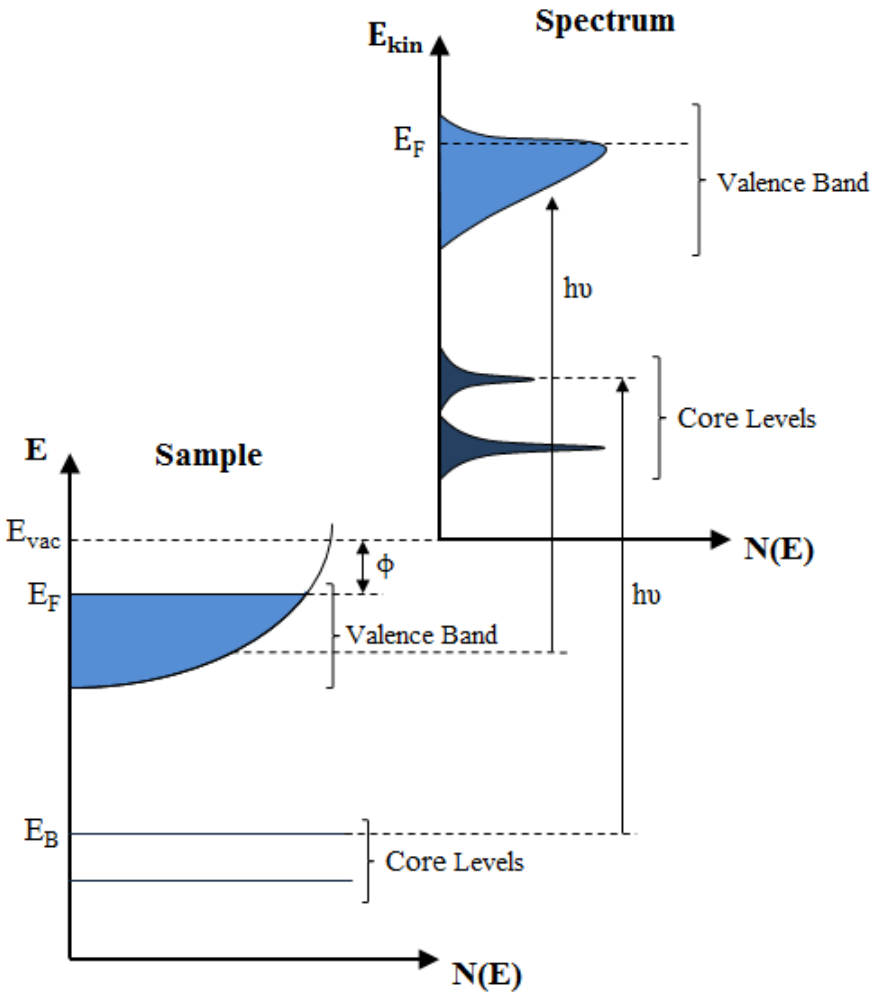


Figure 2.3 – Energy distribution in the photoemission process. In right, the energy distribution of the photoelectrons measured as function of the kinect energy ($E_{kin}$). in left, the energy distribution of the electrons inside the solid in terms of binding energy ($E_B$). $E_B = 0$ at $E_F$.

X-Ray Photoemission Spectroscopy (XPS), also called Electron Spectroscopy for Chemical Analysis (ESCA), is the experimental technique that uses the spectrum of the core levels to study the chemical composition of a sample [70]. Each element has a distinct set of core level energies that appears as sharp peaks in the photoemission spectrum, see figure 2.3. Figure 2.4 shows the XPS data acquired from a $Bi_2Se_3$ single crystal. The position of the peaks is the signature of the elements present in the sample. Other kinds of information can also be obtained from the XPS data, for instance: energy shifts indicate chemical bonds between elements; the amplitude of the peaks can be used to estimate

the amount of each chemical component; and the sharpness of the peaks can differentiate from surface and bulk photoelectrons.

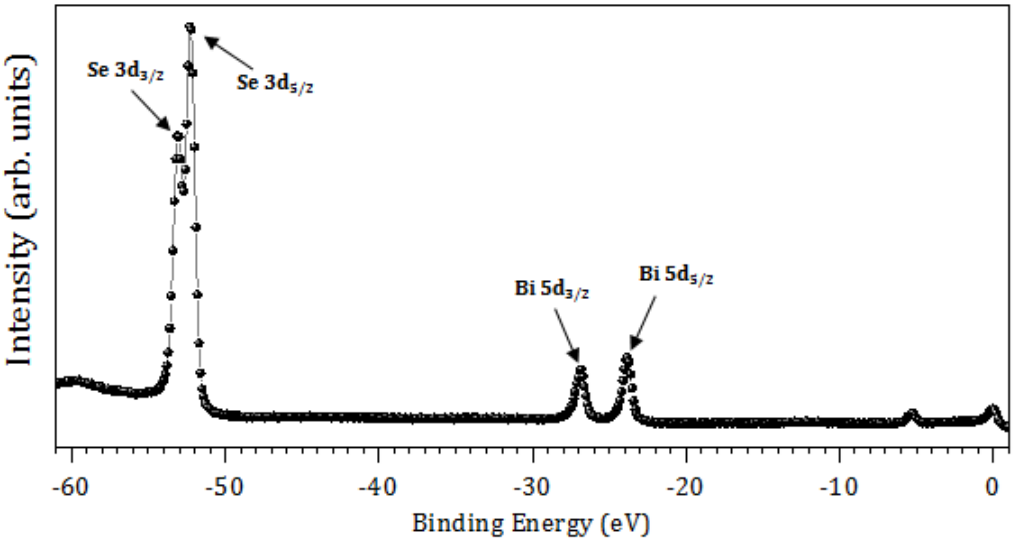


Figure 2.4 – XPS data of $Bi_2Se_3$. Selenium 3d and Bismuth 5d peaks are identified. The XPS data was acquired using a photon energy of 312 eV in the PGM beamline/LNLS.

### 2.1.3 Angle-Resolved Photoemission Spectroscopy - ARPES

Photoelectrons with the same kinect energy escape the material with different values of momentum. An ARPES experiment consists of measuring both kinect energy and momentum of the photoelectrons. The basic components of an ARPES experiments are illustrated in figure 2.5. The electron energy analyzer is composed by an aperture that selects the photoelectrons from a specified angular range. The three components of the photoelectron momentum ($\mathbf{k}_{out}$) are given by:

$$\mathbf{k}_{out}^{x} = \frac{1}{\hbar}\sqrt{2mE_{kin}}\sin\theta\cos\phi \tag{2.3a}$$

$$\mathbf{k}_{out}^{y} = \frac{1}{\hbar}\sqrt{2mE_{kin}}\sin\theta\sin\phi \tag{2.3b}$$

$$\mathbf{k}_{out}^{z} = \frac{1}{\hbar}\sqrt{2mE_{kin}}\cos\theta \tag{2.3c}$$

The concomitant measurement of both kinect energy and momentum of the photoelectrons is what makes ARPES such a powerfull technique. This peculiarity is particularly important due the possibility of retrieve the energy-momentum relation of the electrons inside the material, i. e, the electronic bandstructure [71]. Energy and momentum conservation laws are used to obtain the relation between the momentum of the electrons

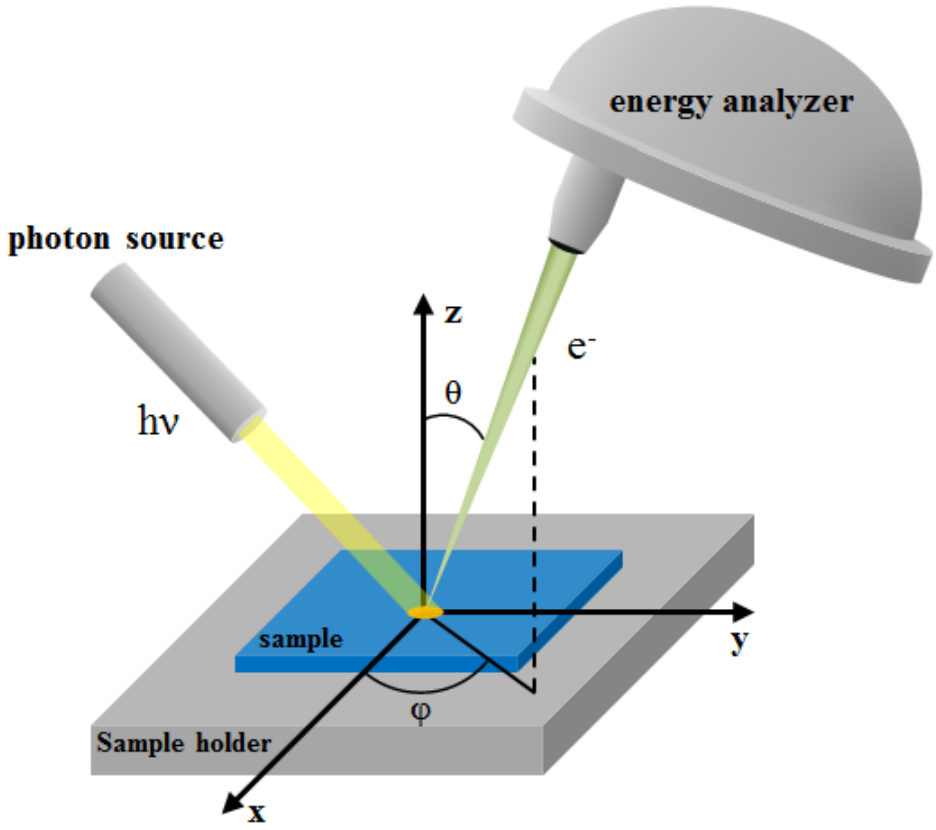


Figure 2.5 – The ARPES experiment. Electromagnetic radiation produced by the photon source ejects electrons from a sample. The electron analyzer measures the kinect energy and the exit angle of the photoelectrons. The geometry of the experiment is controlled by the movement of the sample, since the electron energy analyzer and the photon source are fixed.

inside the solid ($\mathbf{k}_{in}$) and the momentum of the photoelectrons ($\mathbf{k}_{out}$), since the photon momentum is always negligible. The conservation of the momentum parallel to the surface is guaranteed by the periodicity of the crystalline structure:

$$\mathbf{k}_{in,\parallel} = \mathbf{k}_{out,\parallel} \tag{2.4}$$

This expression is essential for the analysis of an ARPES data. Since surface states are uniquely determined by their in-plane momentum, the parallel momentum of the photoelectrons is sufficient to study their dispersion.

Since the crystalline potential vanishes at the surface, the perpendicular component of the momentum does not conserve. The free-electron final state model [72] provides a direct relation for the perpendicular components. In this model, the interface between sample and vacuum is represented by a potential barrier and the final state of the photoelectrons is approximated by a free-electron dispersion, see figure 2.6. The kinect

energy of the photoelectrons is given by:

$$E_{kin} = \frac{\hbar^2}{2m}\mathbf{k}_{out}^2 = \frac{\hbar^2}{2m}\mathbf{k}_{in}^2 - V_0 \tag{2.5}$$

Where $V_0$ is the potential of the vacuum barrier, called inner potential. The final expression for the out-of-plane momentum of the electrons inside the solid is:

$$k_{in,\perp} = \sqrt{\frac{2m}{\hbar^2}(E_{kin}\cos^2\theta + V_0)} \tag{2.6}$$

This formula is uniquely determined from measured data ($E_{kin}$ and $\theta$), if you know beforehand the value of $V_0$. The calculation of $k_{in,\perp}$ by this method works reasonably well only for large kinetic energies, up to 100 eV [72].

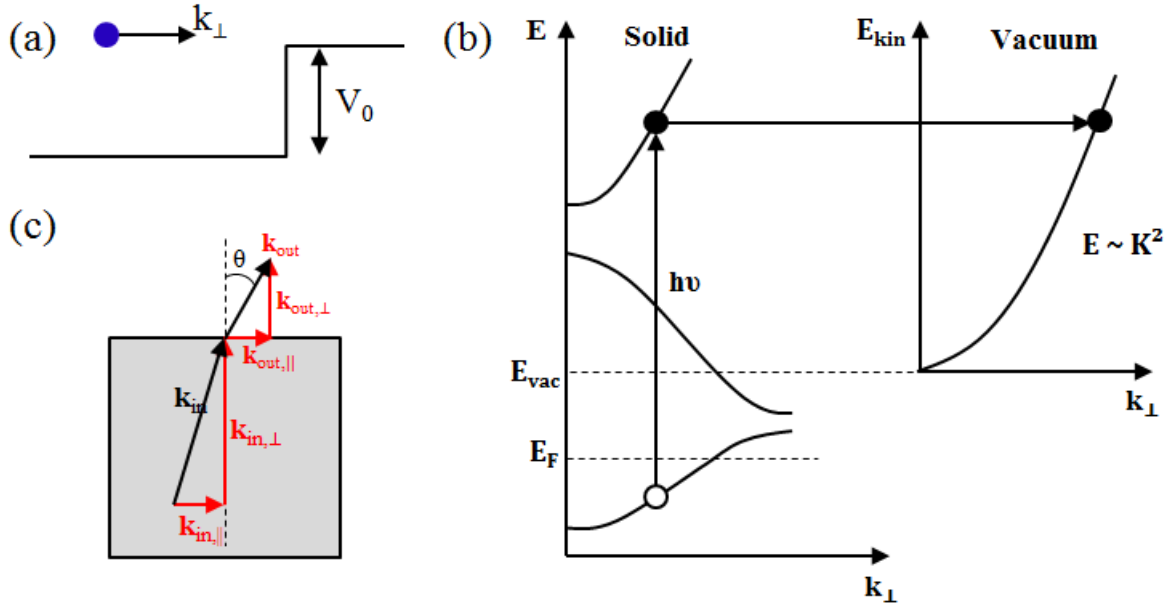


Figure 2.6 – The free-electron final state model. (a) The interface between sample and vacuum is approximated by a potential barrier $V_0$. (b) The transmission through the barrier reduces the perpendicular momentum of the photoelectrons while the parallel momentum is conserved. (c) The photoelectron final state is approximated by a free-electron state (E $\sim K^2$).

## 2.2 Theory of Photoemission

### 2.2.1 Photoemission Theory of Independent Electrons

The quantum mechanical treatment of the photoemission process involves the energy transfer from the incoming photon to the electron inside the solid. The intensity of the photoemission signal is associated to the transition probability of the electrons being excited into the final state measured by the electron analyzer [63]. The Hamiltonian describing an electron subjected to a electromagnetic field is [7]:

$$\begin{aligned}\hat{H} &= \frac{1}{2m}\Big(\mathbf{p} - e\mathbf{A}(\mathbf{r},t)\Big)^2 + V(\mathbf{r}) \\ &= \frac{p^2}{2m} + V(\mathbf{r}) - \frac{e}{2m}\Big(\mathbf{p}\cdot\mathbf{A}(\mathbf{r},t) + \mathbf{A}(\mathbf{r},t)\cdot\mathbf{p}\Big) + \frac{e^2}{2m}\Big|\mathbf{A}(\mathbf{r},t)\Big|^2\end{aligned} \tag{2.7}$$

Where $\mathbf{p} = -i\hbar\nabla$ is the momentum operator, $\mathbf{A}(\mathbf{r},t) = \mathbf{A}_0 e^{i(\mathbf{q}\cdot\mathbf{r}-\omega t)}$ is the magnetic vector potential and $V(\mathbf{r})$ is the crystalline periodic potential. The first two terms of the extended equation 2.7 represents the electron Hamiltonian in the absence of electromagnetic radiation. Third and fourth terms are reduced into one term using the commutator $\big[\mathbf{p}, \mathbf{A}(\mathbf{r},t)\big] = i\hbar\nabla\cdot\mathbf{A}(\mathbf{r},t) \approx 0$, valid if $\mathbf{q} \perp \mathbf{A}_0$. The last term refers to two-photon processes and can be neglected [73]. The Hamiltonian of one electron subject to a electromagnetic field reduces to:

$$\hat{H} = \frac{p^2}{2m} + V(\mathbf{r}) - \frac{e}{m}e^{i\mathbf{q}\cdot\mathbf{r}}\Big(\mathbf{A}_0\cdot\mathbf{p}\Big)e^{-i\omega t} \tag{2.8}$$

If the electromagnetic field is treated as a weak perturbation in the electron system, the Hamiltonian has the form of a time-dependent perturbation $\hat{H} = \hat{H}_0 + \hat{H}_1 e^{-i\omega t}$ [15]. For the case of many electrons forming a complex bandstructure, the obtainment of the eigenfunctions and eigenenergies becomes very complicated. However, the photoemission intensity is related to the transition probability of the electrons jump from their initial state to their final photoemitted state. The transition probability of one electron to jump from the initial state $|\Psi_i\rangle$ to the final state $|\Psi_f\rangle$ is given by the Fermi's golden rule [74]:

$$\Gamma_{i\to f} = \frac{2\pi}{\hbar}\Big|\langle\Psi_f|\hat{H}_1|\Psi_i\rangle\Big|^2\delta\Big(E_f - E_i - \hbar\omega\Big) \tag{2.9}$$

The delta-function on the right side of the equation portrays the energy conservation in the photoemission process as described by equation 2.2. The term inside the modulus is

called transition matrix element ($M_{if}$) and it preserves all intrinsic information about initial and final states and the interaction with the light source.

The photon sources used in photoemission experiments generally comes from lab-based UV lamps and Synchrotron radiation facilities. The wavelength is very large (124 Å at 100 eV) compared to atomic dimensions ($\sim$ 1 Å). Since the wavefunction oscillation is very rapid at atomic dimensions, the photon field experienced by the electrons is treated as constant ($\mathbf{A}_0 e^{i\mathbf{q}\cdot\mathbf{r}} \approx \mathbf{A}_0$). This is called dipole approximation and works well for regular UV photon sources [75]. Using this approximation and the quantum-mechanical identity $\langle\Psi_f|\mathbf{p}|\Psi_i\rangle = im\frac{E_f - E_i}{\hbar}\langle\Psi_f|\mathbf{r}|\Psi_i\rangle$ [15], the transition matrix element, expressed in terms of its wavefunctions, becomes:

$$M_{if} = -i\frac{E_f - E_i}{\hbar}\mathbf{A}_0 \int \Psi_f^*(\mathbf{r})[e\mathbf{r}]\Psi_i(\mathbf{r})\, d^3r \tag{2.10}$$

Where $e\mathbf{r}$ is the electrical dipole operator. The practical consequence of the dipole approximation is the appearance of selection rules. They are originated from the polarization dependence of the matrix element expressed in terms of the photon polarization ($\epsilon \parallel \mathbf{A}_0$) and the dipole momentum of initial and final states.

The photoemission intensity for a given energy $E_f$ is obtained by the summation of the transition probability for all occupied states in the material:

$$I(E_f) \propto \sum_i^{occ} \left|\langle\Psi_f|\epsilon\cdot e\mathbf{r}|\Psi_i\rangle\right|^2 \delta\Big(E_f - E_i - \hbar\omega\Big) \tag{2.11}$$

This expression requires the knowledge of the initial and final state wavefunctions. Two different approaches are employed to solving this issue: the one-step model [76] and the three-step model [77]. In the one-step model, the photoemission process is treated a single step: the excitation of the electron from the initial state inside the solid directly to the vacuum final state. For valence band spectroscopy (ARPES), the initial states are bulk Bloch waves $u_n(\mathbf{r})e^{i\mathbf{k}_i\cdot\mathbf{r}}$ [5] and the final states are approximated by free-electron waves $e^{i\mathbf{k}_f\cdot\mathbf{r}}$, also called the "inversed LEED state" [78].

A more instructive method for the evaluation of the photoemission intensity is provided by the three-step model. The photoemission process is divided in three independent and complementary steps: (1) the photoexcitation of an electron into a bulk final state, (2) the travel to the surface and (3) the transmission through the surface into the vacuum. A comparative image containing both models is presented in figure 2.7. The first step gathers all information about the intrinsic properties of material and the initial state is the same employed for the one-step model. On the other hand, the final state is represented

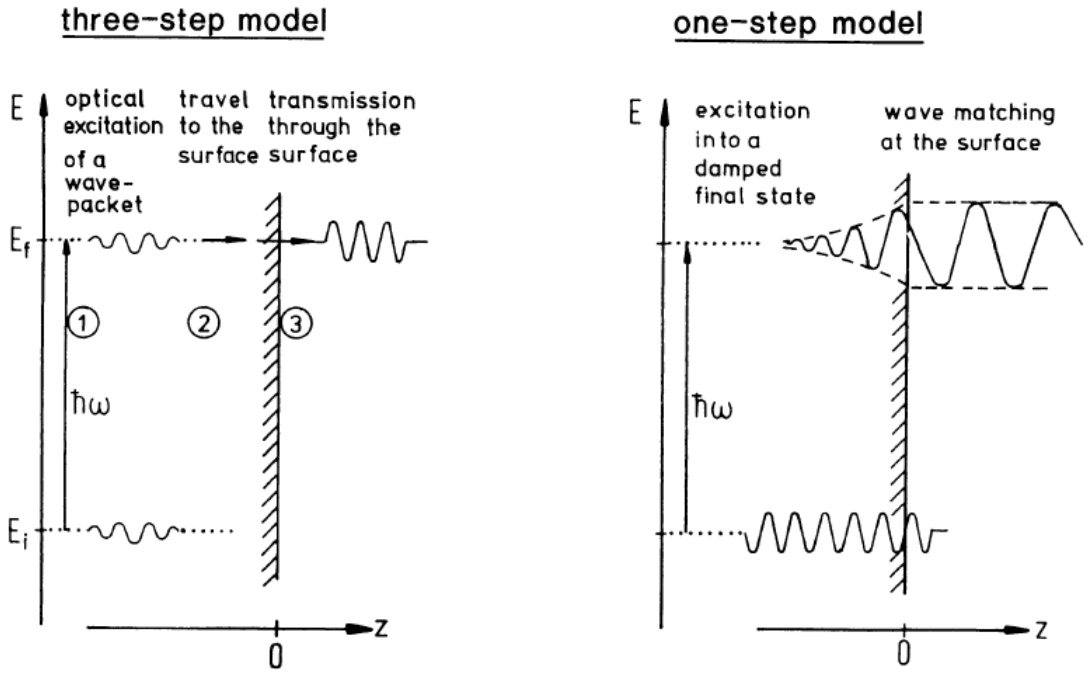


Figure 2.7 – Three-step model vs. One-step model in photoemission theory. In the one-step model, the photoemission process is treated a single step: the excitation of the electron to the vacuum final state. In the three-step model, the photoemission process is divided in three steps: the electron excitation into a bulk final state; the travel to the surface and the transmission through the surface into the vacuum. Image taken from [63].

by a bulk state from the material. More specifically, a Bloch wave containing plane-wave contributions with a number of reciprocal lattice vectors $\mathbf{G}$:

$$\Psi_f(\mathbf{k}) = \sum_{\mathbf{G}} u_f(\mathbf{k}, \mathbf{G}) e^{i(\mathbf{k}+\mathbf{G})\cdot\mathbf{r}} \tag{2.12}$$

Since the photon momentum is negligible compared to the electrons momentum, the periodicity of the crystalline potential guarantees the momentum conservation between initial and final states ($\mathbf{k}_f = \mathbf{k}_i + \mathbf{G}$).

The second step explores the transport of the electrons through the crystal to the surface. During this process, part of the kinect energy of the electrons is lost due to inelastic scattering provoked by interactions with other electrons, phonons and defects in the material. These interactions produce an inelastic background escorting the spectral peaks in the photoemission spectrum, see figure 2.8. The inelastic scattering is evaluated in terms of the electron mean free path which varies from 2 to 20 Å in typical photoemission experiments [79]. Almost 95% of the photoemission signal comes from a penetration depth of approximately three times the mean free electron path, what makes photoemission spectroscopy extremely surface-sensitive. Finally, the third step deals with the transmission

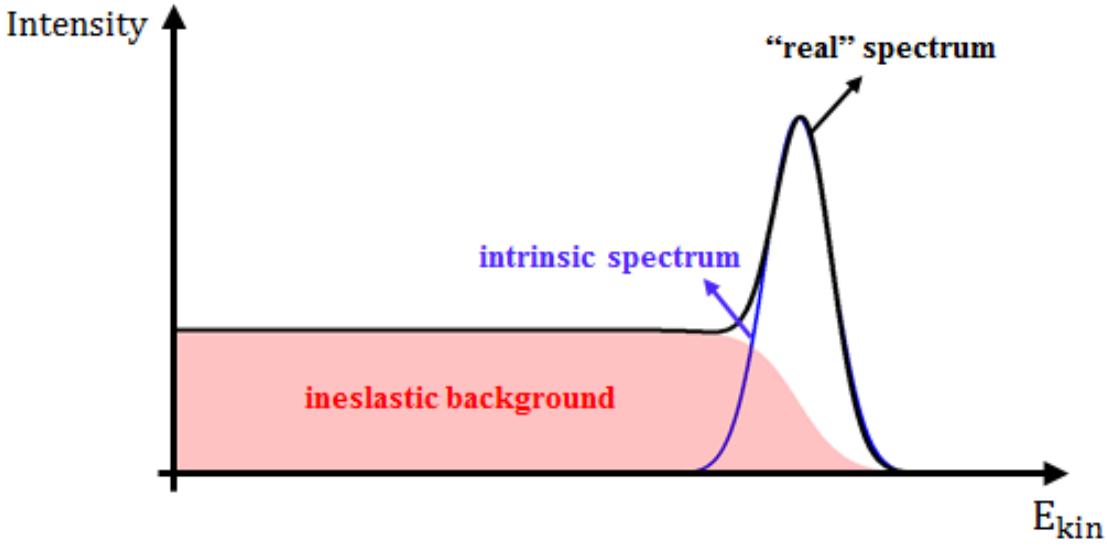


Figure 2.8 – Inelastic background. Spectral peaks have a "loss-tail" towards lower kinect energies due to inelastic scattering with other electrons, phonons, etc.

of the electrons through the surface into the vacuum. The transmission rate depends on the potential vacuum barrier. In the free-electron approximation, the final state is obtained from the inner potential $V_0$ and approximated by a free electron state in the vacuum, see figure 2.6. An important consequence of this step is the non-conservation of the perpendicular momentum.

A photoemission experiment provides a statistical result involving an enormous quantity of photoelectrons, all subjected to the Fermi-Dirac distribution [80]. The final expression of the photoemission intensity is:

$$I(E,\mathbf{k}) = I_B(E) + f(E,T)\sum_f \sum_i^{occ} \delta(E - E_f - \phi)\delta(\mathbf{k} - \mathbf{k}_f)|M_{if}|^2 \delta(E_f - E_i - \hbar\omega)\delta(\mathbf{k}_f - \mathbf{k}_i - \mathbf{G}) \tag{2.13}$$

Where $I_B(E)$ is the inelastic background and $f(E,T)$ is the Fermi-Dirac distribution. The influence of the temperature introduced by the Fermi-Dirac distribution requires that photoemission experiments should be performed at low temperatures to avoid thermal broadening.

### 2.2.2 Photoemission Theory of Interacting Electrons

The development of the photoemission theory presented so far has taken into account the reasonable premise that the photoelectrons do not interact with the remaining electrons inside the solid. This approximation is valid for most of the materials studied in photoemission experiments. The most relevant exception are strong-correlated materials [81], which are only fully understood if strong interactions are considered among the electrons [82]. Some examples are transition metal oxides, as high-Tc superconductors [83], Mott insulators [84], heavy fermions [85] and other low dimensional materials. The complete description of the photoemission process requires a many-body approach where photoemission is treated as the sudden removal of an electron from a system with N electrons. The energy lost by the photoemitted electron is stored by the remaining N-1 electrons. This energy loss is originated from electron-electron interactions [86], phonons [87] or magnons [88]; see figure 2.9.

The photoemission intensity is obtained from the transition probability of an electron be photoemitted from the N-electron system:

$$I(\mathbf{k},\epsilon) \propto \sum_{s} \left|\langle N-1,s;k|\hat{H}_1|N,0\rangle\right|^2 \delta\Big(E_{N-1,s}+\epsilon-E_{N,0}-\hbar\omega\Big) \tag{2.14}$$

Where the initial state is formed by the N electrons in ground state with energy $E_i = E_{N,0}$ and the final state is formed by the composition of the N-1 remaining electrons in the excited state $E_{N,s}$ and the photoelectron with momentum $\mathbf{k}$ and energy $\epsilon$. From the second quantization formalism and the factorization of the light-matter interaction for each electron, the interacting Hamiltonian $\hat{H}_1$ is given by:

$$\hat{H}_1 \propto \sum_{j=1}^{N} \mathbf{A}(\mathbf{r}_j)\cdot\mathbf{p}_j = \sum_{i,f} M_{if} c^{\dagger}_{\mathbf{k}_f} c_{\mathbf{k}_i} \tag{2.15}$$

Where $M_{if}$ is the one-electron transition matrix element. $c^{\dagger}_{\mathbf{k}_f}$ and $c_{\mathbf{k}_i}$ are creation and annihilation operators that create an electron with momentum $\mathbf{k}_f$ and annihilate an electron with momentum $\mathbf{k}_i$, respectively.

The sudden approximation states that the photoelectron decouples from the remaining system immediately after photoexcitation, before relaxation [89]. The final state is factorized into one photoelectron state with momentum $\mathbf{k}$ and the remaining N-1 electron state, which are assumed to be an eigenstate of the unperturbed Hamiltonian:

$$|N-1,s;k\rangle = c^{\dagger}_{\mathbf{k}}|N-1,s\rangle \tag{2.16}$$

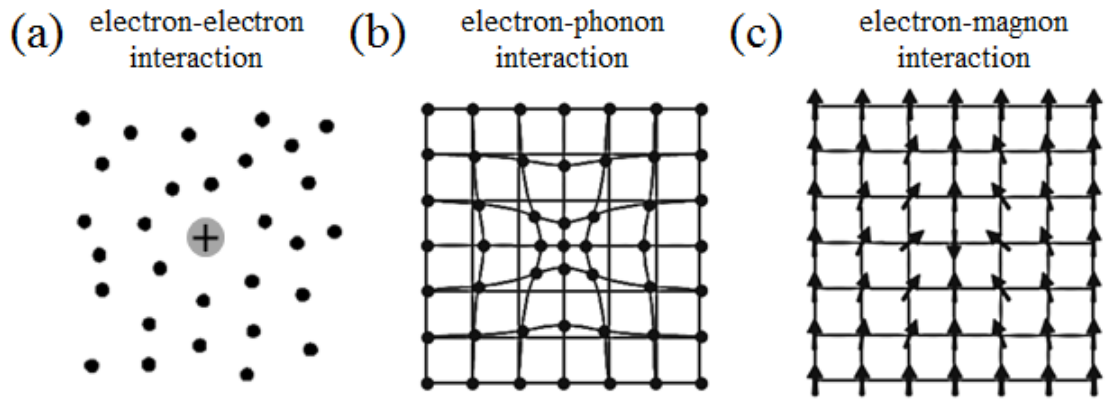


Figure 2.9 – Many-body interactions in photoemission. (a) Coulomb repulsion (electron-electron). (b) lattice distortion (electron-phonon), (c) spin distortion (electron-magnon).

From this statement, the photoemission intensity becomes :

$$I(\mathbf{k},\epsilon) \propto \sum_{s} \left|\langle N-1,s|c_{\mathbf{k}} \sum_{i,f} M_{if} c^{\dagger}_{\mathbf{k}_f} c_{\mathbf{k}_i}|N,0\rangle\right|^2 \delta\Big(E_{N-1,s}+\epsilon-E_{N,0}-\hbar\omega\Big) \tag{2.17}$$

Using momentum conservation and assuming that $M_{if}$ is constant in the energy and momentum range of interest, the obtained photoemission intensity is:

$$I(\mathbf{k},\epsilon) \propto \sum_{s} \left|\langle N-1,s|c_{\mathbf{k}}|N,0\rangle\right|^2 \delta\Big(E_{N-1,s}+\epsilon-E_{N,0}-\hbar\omega\Big) \tag{2.18}$$

Where it is straightforward to observe that photoemission intensity is proportional to the probability of removing an electron with energy $\epsilon$ and momentum $\mathbf{k}$ from the N-electron system. In other words, it is proportional to the removal part of the spectral function $A(\mathbf{k},\epsilon)$. Gathering all this information, the final expression for the photoemission intensity is condensed to:

$$I(\mathbf{k},\epsilon) = I_0(\mathbf{k},\hbar\omega\mathbf{A}) f(\epsilon,T) A(\mathbf{k},\epsilon) \tag{2.19}$$

Where $I_0(\mathbf{k},\hbar\omega\mathbf{A}) = \sum_{i,f} M_{if}$ is the dipole matrix element, which carries information about the interaction of the electrons with the photon source, for instance: photon energy and polarization.

Before analyzing the spectral function in equation 2.19, it is important to make a distinction between the energy dispersion of a system with non-interacting electrons and a system where electron interactions are present. The independent electrons figure produces an energy-momentum dispersion $\epsilon_0(\mathbf{k})$. When evaluated along all reciprocal space, it retrieves the electronic bandstructure of the material [63]. In the interacting electrons case, this is not completely true. The photoelectrons suffer an energy renormalization caused by the energy lost in the excitation of the remaining system. This renormalization is expressed by the self-energy $\Sigma(\mathbf{k}, \epsilon)$, which quantify the electronic interaction with the remaining N-1 electrons. The energy-momentum dispersion of the associated quasiparticle is given by:

$$\epsilon(\mathbf{k}) = \epsilon_0(\mathbf{k}) + \Sigma(\mathbf{k}, \epsilon) \tag{2.20}$$

The self-energy $\Sigma(\mathbf{k}, \epsilon)$ is a complex function. The real part gives the energy renormalization and the imaginary part is related to the lifetime broadening of the quasiparticle, see figure 2.10. The spectral function is directly proportional to the imaginary part of the Green function:

$$A(\mathbf{k}, \epsilon) = -\frac{1}{\pi} Im\ G(\mathbf{k}, \epsilon) \tag{2.21}$$

and the Green function $G(\mathbf{k}, \epsilon)$ for this case is:

$$G(\mathbf{k}, \epsilon) = \frac{1}{\epsilon - \epsilon(\mathbf{k}) + i0^+} \tag{2.22}$$

In the independent electrons picture, the spectral function $A_0(\mathbf{k}, \epsilon)$ is given by:

$$A_0(\mathbf{k}, \epsilon) = -\frac{1}{\pi} Im\ G_0(\mathbf{k}, \epsilon) = \delta\Big(\epsilon - \epsilon_0(\mathbf{k})\Big) \tag{2.23}$$

Where $\delta(\epsilon - \epsilon_0(\mathbf{k}))$ denotes a Dirac delta function. The spectral function $A_I(\mathbf{k}, \epsilon)$ of the interacting electrons system is obtained from the quasiparticle dispersion in equation 2.20:

$$A_I(\mathbf{k}, \epsilon) = -\frac{1}{\pi} Im\ G_I(\mathbf{k}, \epsilon) = \frac{\Sigma_2(\mathbf{k}, \epsilon)}{\Big(\epsilon - \epsilon_0(\mathbf{k}) - \Sigma_1(\mathbf{k}, \epsilon)\Big)^2 + \Sigma_2(\mathbf{k}, \epsilon)^2} \tag{2.24}$$

Where $\Sigma_1(\mathbf{k}, \epsilon)$ and $\Sigma_2(\mathbf{k}, \epsilon)$ are respectively the real and imaginary part of the self-energy $\Sigma(\mathbf{k}, \epsilon)$. In most cases, the $\mathbf{k}$-dependence can be neglected and $\Sigma(\mathbf{k}, \epsilon) = \Sigma(\epsilon)$. The relation between real and imaginary parts of the self-energy is given by Kramers-Kronig relations [90].

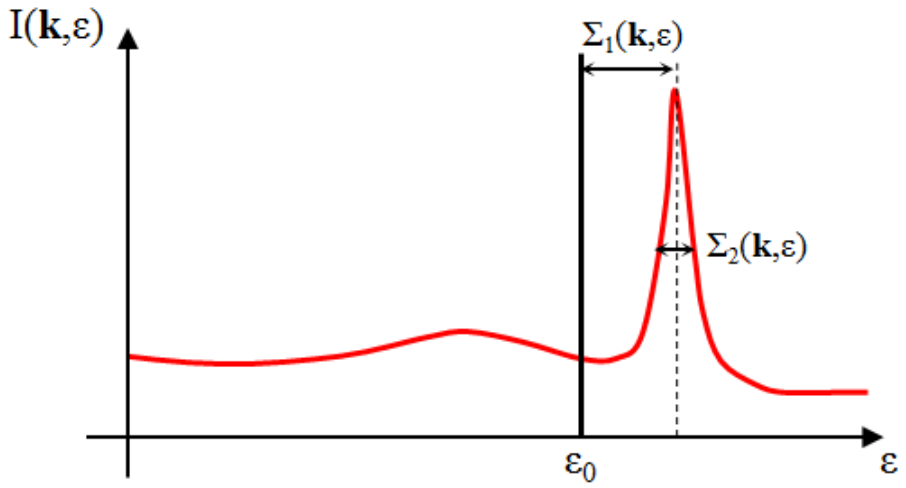


Figure 2.10 – Photoemission Self-energy. The real part of the self energy $\Sigma(\mathbf{k},\epsilon) = \Sigma_1(\mathbf{k},\epsilon)+i\Sigma_2(\mathbf{k},\epsilon)$ gives the energy renormalization, while the imaginary part gives the lifetime of the quasiparticle, i. e, the full width at half maximum (FWHM).

## 2.3 ARPES: Instrumentation and Implementation

The instrumentation required for the execution of an ARPES experiment involves three important elements: the photon source, the sample environment and the electron analyzer. The following paragraphs present the most important aspects associated to each of these components.

### 2.3.1 Photon Sources

The selection of the photon energy is of essential importance for a photoemission experiment. The importance of the photon energy is pointed out by the electron mean free path, i. e, how long the electron travels without being scattered. Figure 2.11 presents the universal curve of the inelastic electron mean free path obtained from [79]. The majority of the experiments are carried out using photon energies in the ultraviolet and soft x-rays range. In this typical range, the electron mean free path varies from 0.2 to 3 Å. That makes ARPES an extremely surface-sensitive technique. The apparent disadvantage is particularly interesting for topological materials, where surface states are more relevant. Three types of photon sources are employed in ARPES experiments nowadays, each applied depending on the purpose. They are: UV gas-discharge lamps, synchrotron light sources and UV lasers.

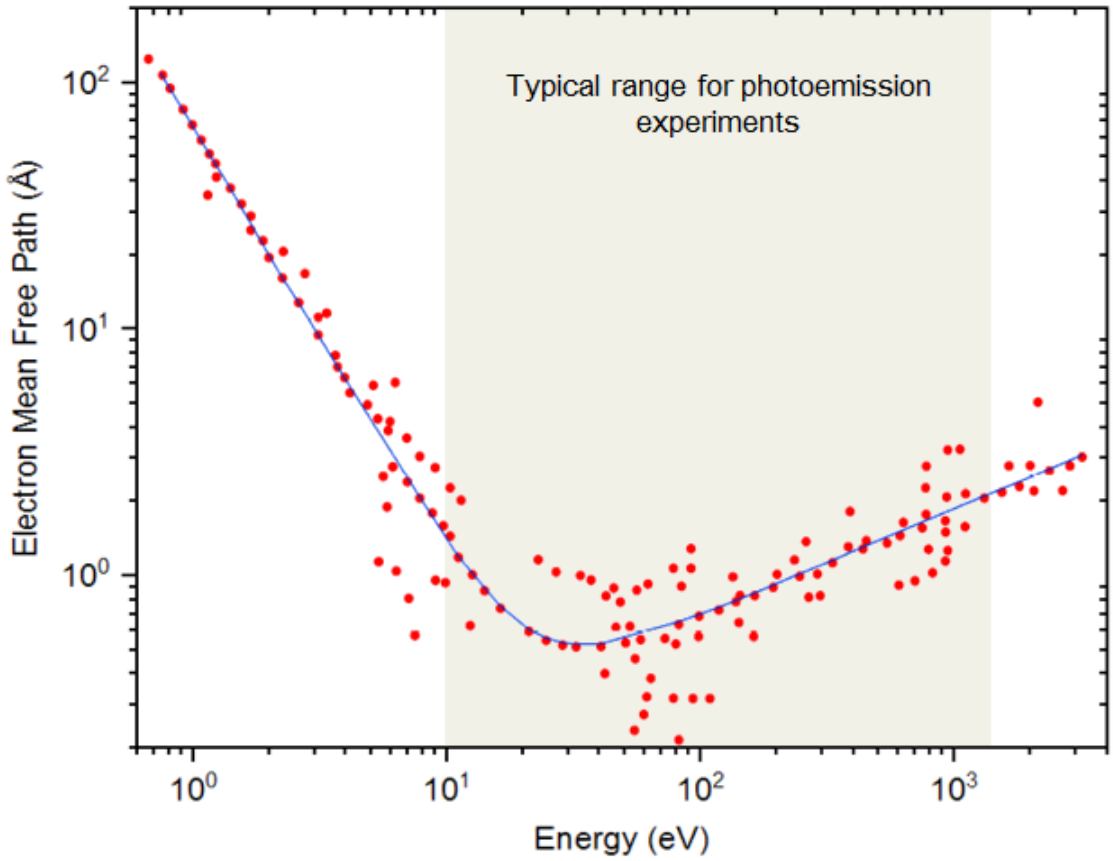


Figure 2.11 – Electron Mean Free Path vs. Electron Energy. Red dots represent experimental data from different materials. The tendency curve is colored in blue. Image taken from [79]

### UV lamps

UV gas-discharge lamps are the most popular photon sources used in laboratories around the world. Their compact size makes them perfect for lab-based ARPES systems [91]. They generate discrete values of photon energies from around 8 to 50 eV [91]. The working principle of a gas-discharge lamp is the ionization of a noble-gas when it is trespassed by an electrical discharge [92]. When the ions return to ground state, energy is released in form of photons. A Helium-lamp, generates photons with two main energies: 21.22 eV and 40.81 eV. Other options of UV lamps include Neon (16.67 and 16.85 eV), Argon (11.62 and 11.83 eV), Krypton (10.03 and 10.64 eV) and Xenon-lamps (8.44 and 9.57 eV). The main advantage of UV lamps is the lower cost of purchase and maintenance. The energy resolution is also noteworthy: $\sim$ 2 meV when combined with a monochromator [91]. Some limitations include the large size of the light beam ($\sim$ 1 mm) and the low photon flux ($\sim 10^{12}$ photons/s) when compared to other light sources.

### Synchrotron light sources

The development of the synchrotron light sources [93] introduced Angle-resolved Photoemission Spectroscopy to another level. The variable photon energy increased considerably the quality of the scientific projects. A synchrotron light laboratory is a scientific facility projected to produce electromagnetic radiation with high brilliance and tunable photon energy. The building is projected to keep electrons moving at relativistic velocities along a close-loop, called storage ring; see figure 2.12. Insertion devices (bending magnets, undulators and wigglers) are responsible for convert the high-energy electron beam into photons [93]. The photon beam produced by the insertion devices passes through a set of optical components to be positioned, focused and monochromatized; finally going to the experimental end-station, called beamline.

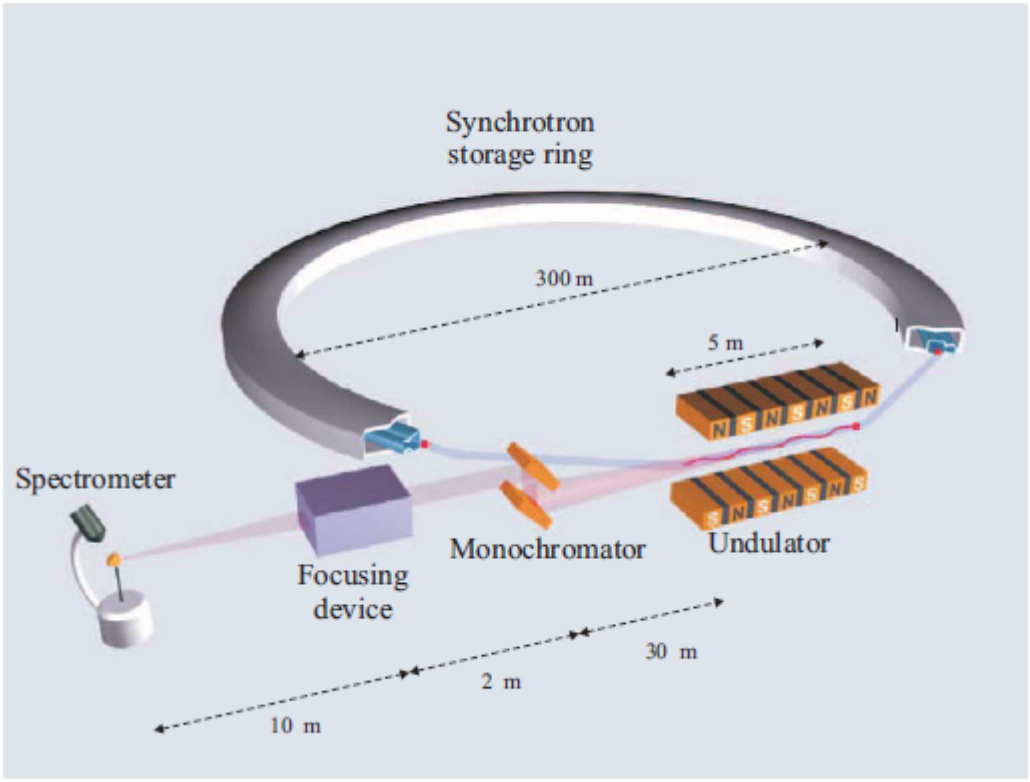


Figure 2.12 – Synchrotron Light Source. A typical beamline containing an undulator, a monochromator and a focusing device is shown. Image taken from [93]

The main advantage of synchrotron light sources is the variable photon energy. The capacity to execute energy-dependent measurements opened the possibility to map the 3D momentum space of the materials [94]. The evaluation of the out-of-plane momentum is also important to distinguish between surface and bulk states, since surface states does not have perpendicular components. Other important feature of synchrotron light sources is the controlling of the light polarization, allowing the analysis of the orbital character of samples

and experiments with dichroism [95]. The extremely small beam spot is another important advantage of synchrotron light sources, achieving 50 nm in nano-ARPES beamlines [96]. The photon flux is around $\sim 10^{12} - 10^{13}$ photons/s. The energy resolution in some ARPES beamlines ($\sim$ 10 meV) is relatively worse than Lamp-based ARPES [97]. This issue is caused due the improvement of the energy resolution been deeply related to the reduction of the photon flux. There are only few synchrotron facilities around the world, often opened for scientific proposals in a semiannual basis. The projects approved by their scientific committees are usually allocated during one week. This short time makes beamtimes extremely valuables for users.

#### UV lasers

Lasers are the less popular photon source used in ARPES experiments, but this reality is changing over the last decade. The main issue with these sources is the low photon energies generated by them ($<$ 10 eV), because of the proximity with the work function of most metallic materials ($\sim$ 5 eV). A solution is been provided by the development of non-linear optical devices to generate sources with higher photon energies. More specifically, using second harmonic generation (SHG) and high harmonic generation (HHG) [98]. UV Lasers are employed when the main concern of the users is to have high photon flux ($\sim 10^{9} - 10^{12}$ photons/s) combined with high energy resolution ($<$ 1meV) [99].

### 2.3.2 Sample Environment

ARPES measurements are mandatorily carried out inside ultrahigh vacuum (UHV) chambers. This requirement is associated with the contamination of the sample surfaces. The intensity of the ARPES signal is manly originated from the first few atomic layers, so an atomically clean surface is essential for a successful experiment [72]. The lifetime of a measurement depends on how long a sample can be appreciated without becoming covered by an insulator layer of adsorbed molecules. At ambient pressure, few nanoseconds are sufficient to cover the sample with a monolayer of absorbed molecules [100]. In UHV chambers, samples can be satisfactorily measured for days depending on their inner pressure. For a relatively relevant number of materials, an atomically clean surface is obtained by performing a crystal cleavage in situ. Pressure cannot be bigger than $10^{-9}$ mbar, otherwise the fresh new surface does not remain clean. An uncounted number of other materials are not cleavable; in those cases, the surface can be cleaned by other methods like polishing, sputtering and annealing [101]. Some systems are equipped with preparation chambers where the sample growth is perform in situ using techniques as molecular beam epitaxy (MBE) [102] and pulsed laser deposition (PLD) [103]. The analysis of the sample quality is done using Low-energy electron diffraction (LEED) [104], Scanning Tunneling Microscopy

(STM) [105] or Atomic-force microscopy (AFM) [106], depending on the purpose of the experiment.

### 2.3.3 Electron Analyzer

The final element of the photoemission experiment refers to the detection of the photoelectrons. Electron energy analyzers are responsible for the measurement of kinect energy and momentum of the photoelectrons. The information regarding the photoelectron energy and momentum are converted into spatial information by an electrostatic construction specially designed for this purpose. The most relevant equipment used for ARPES experiments is the hemispherical analyzer (HSA) [107]. It consists of two concentric hemispherical electrodes responsible for forcing the photoelectrons into different trajectories depending on their kinect energy. The electric field created by the electrodes bends the photoelectrons into concentric trajectories making them reach the detector at different positions, see figure 2.13.

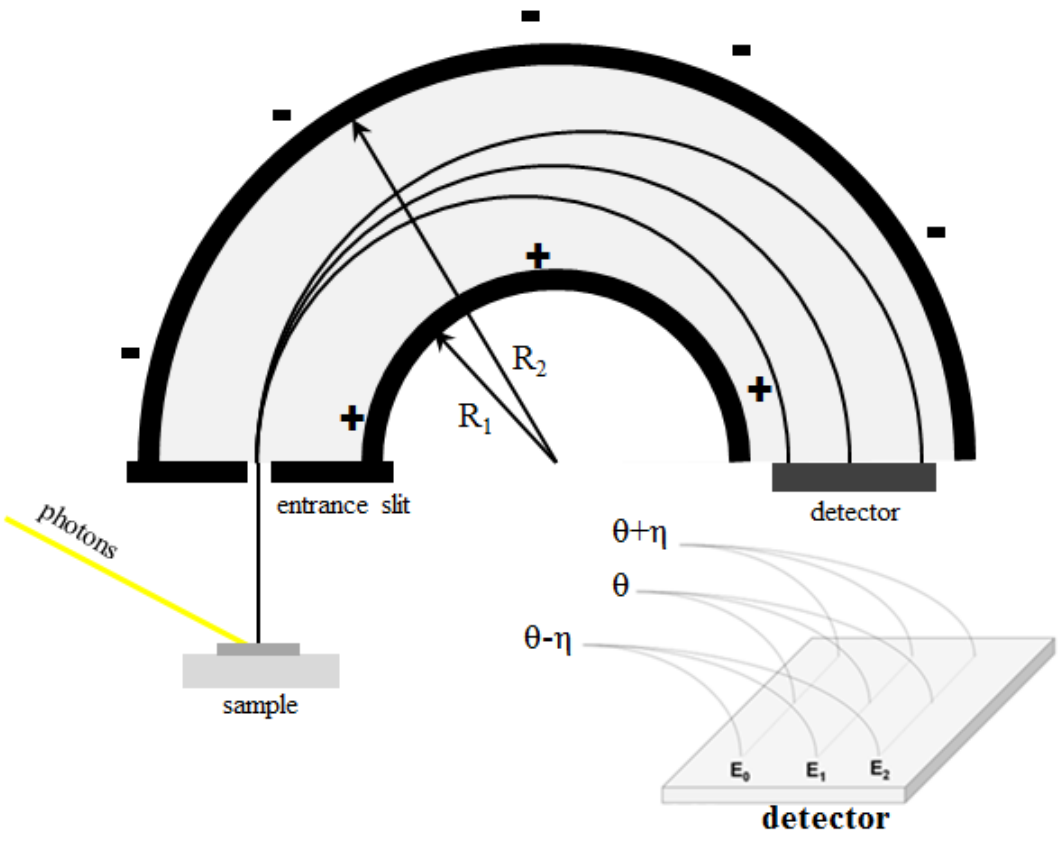


Figure 2.13 – Hemispherical Electron Energy Analyzer (HSA). Two charged hemispherical electrodes with radius $R_1$ and $R_2$, produce an electrical field responsible for forcing the photoelectrons into different trajectories depending on their kinect energy. The position they reach the detector depends on their trajectory and the angular selection done by the entrance slit.

In order to obtain an efficient result for the energy-momentum dispersion, the experimentalist should take into account some important aspects. The pass energy ($E_P$) is responsible for the selection of the energy range to be measured. An electron with kinect energy $E_P$ will execute a trajectory with radius $R = (R_1 + R_2)/2$, where $R_1$ and $R_2$ are the radius of the inner and outer hemispheres, respectively. The value of $E_P$ is obtained from the geometry of the analyzer and the applied voltage on the electrodes ($U$). The applied voltage is controlled by the user and the relation with the pass energy is given by:

$$E_P = \frac{eU}{R_2/R_1 - R_1/R_2} \tag{2.25}$$

The energy resolution ($\Delta E$) is another variable controlled by the dimensions of the equipment. In Particular, the width ($s$) and the angular resolution ($\alpha$) of the entrance slit. For the hemispherical analyzer, the energy resolution is:

$$\Delta E = E_P \left( \frac{s}{R_1 + R_2} + \frac{\alpha^2}{4} \right) \tag{2.26}$$

It is important to mention that there are two distinct energy resolutions involved in the photoemission process: the energy resolution of the photon source and the energy resolution of electron analyzers. The state-of-the-art hemispherical analyzer achieves energy resolution around 2-10 meV and angular resolution of 0.2°.

### 2.3.4 ARPES Experiment

For a successful ARPES experiment, it is important to have access to different geometrical configurations of the source-sample-analyzer system. The photon source and the electron analyzer are fixed, so the controlling of the geometry is done by the position of the sample. A good sample manipulator should be capable of positioning the sample along six degrees of freedom: three translational axes and three angular axes, see figure 2.14. Before start the measurements, the experimentalist should find the best configuration for the sample position. The first step consists of positioning the $y$-direction of the sample manipulator. This direction controls the distance between sample and photon source and the most effective position is obtained when the sample is placed at the focus of the photon beam. In this case, the maximum intensity of photon source is utilized. The next step is to positioning the sample along $x$- and $z$-directions. Depending on the beam spot size, these axes are useful to search for an atomically flat region in the sample, where a better signal is achieved.

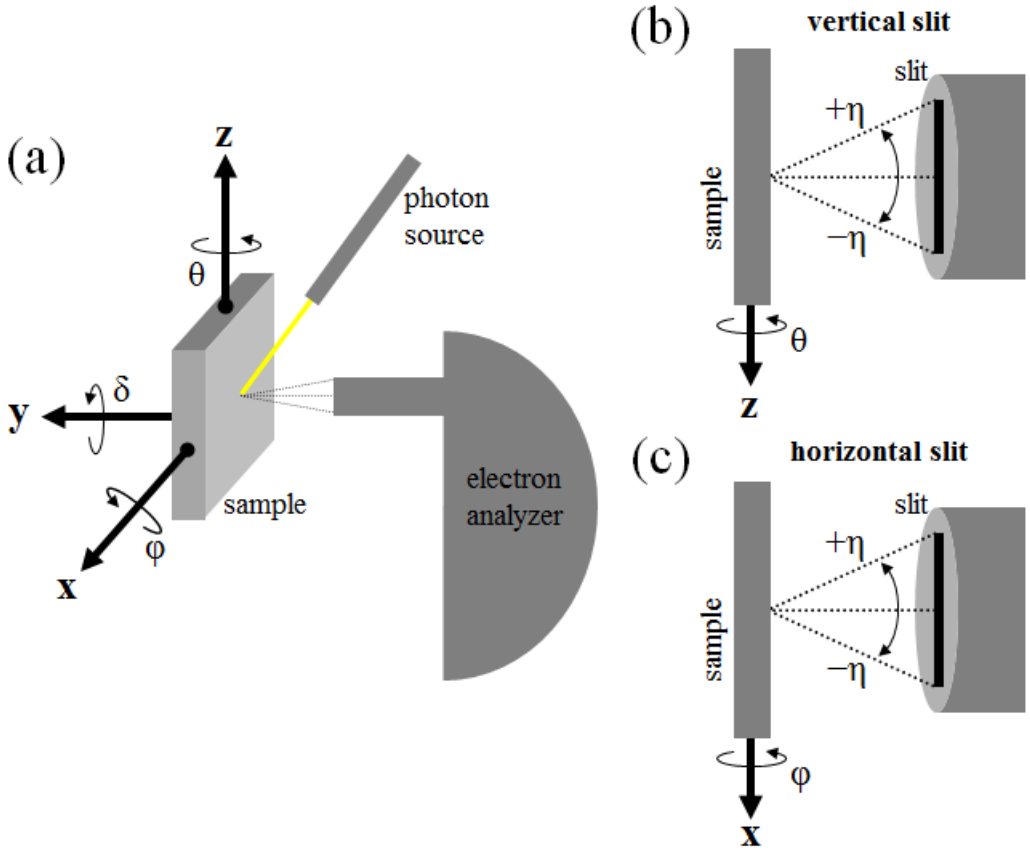


Figure 2.14 – Geometry of the sample manipulator. (a) The sample can move along the directions $x$, $y$ and $z$ and rotates by the respective angles $\phi$, $\delta$ and $\theta$. The angle $\eta$ defines the angular acceptance of the slit. (b) Vertical slits are parallel to $z$-axis, while (c) horizontal slits are parallel to $x$-axis.

The angular calibration is more complicated, it is associated with the image acquired by the electron analyzer. The entrance slit of the analyzer defines the angular range of the incoming electrons from $-\eta$ to $+\eta$. The resulting dispersion is a image representing the photoemission intensity $I(E_{kin}, \eta)$ with the axes formed by the kinect energy of the photoelectrons (the energy range is selected by $E_P$) and the angular range of the entrance slit ($\eta$). A 2D angular map is obtained rotating the sample along the axis perpendicular to the entrance slit. There are two possible configurations for the entrance slit of an electron analyzer: horizontal and vertical. For horizontal slits, the 2D angular map is obtained varying $\phi$ while $\theta$ is fixed, resulting in a 3D matrix $I(E_{kin}, \theta + \eta, \phi)$. For vertical slits, the 2D angular map is obtained varying $\theta$ while $\phi$ is fixed, resulting in a matrix $I(E_{kin}, \eta, \theta)$. From the geometrical configuration of the system and using the equations in 2.3, the 3D angular matrix is converted to a 3D momentum matrix $I(E_{kin}, k_x, k_y)$ revealing the in-plane energy-momentum dispersion of the sample $E_B(\mathbf{k}_\parallel)$.

A potential application of an ARPES experiment is the recovering of the Fermi surface (FS) of a sample, i. e, the electronic momentum dispersions at the Fermi level: $I(k_x, k_y, k_z)$ at $E_B = 0$. This operation is done in two parts: the determination of the

in-plane Fermi surface and the out-of-plane Fermi surface. The in-plane Fermi surface is obtained following the steps described in the last paragraph, resulting in the 2D momentum map $I(k_x, k_y)$ at $E_B = 0$. The out-of-plane Fermi surface involves the construction of a 2D momentum map $I(k_x, k_z)$, which requires the knowledge of the $k_z$ dependency. The pragmatic solution for this problem consists of measuring the sample at different photon energies and making use of the free-electron final state model. This procedure should be carried out with the sample positioned at normal emission ($\theta = 0$), thereby the cosine in equation 2.6 equals the unity. Therefore, the relation between the perpendicular momentum ($k_z$) of the electrons inside the solid and the photon energy ($\hbar\omega$) at the Fermi level ($E_B = 0$), is given by:

$$k_z = \sqrt{\frac{2m}{\hbar^2}(\hbar\omega - \Phi + V_0)} \tag{2.27}$$

Maintaining the sample fixed, $I(E, k_x)$ maps are acquired varying the photon energy. Fixing the kinect energy at the Fermi level, a 2D map $I(k_x, \hbar\omega)$ at normal emission is obtained. The conversion to an out-of-plane Fermi surface $I(k_x, k_z)$ is done using the relation in equation 2.27, if the value of $V_0$ is known beforehand. If $V_0$ is unknown, an iterative method is employed to modify the value of $V_0$ until the $k_z$-axis matches the out-of-plane periodicity of the reciprocal lattice of the sample.

# Chapter 3

# Experimental Realization of the Quaternary Topological Insulator $BiSbSe_{2.5}Te_{0.5}$

## 3.1 Bi-Chalcogenide Topological Insulators

Since the theoretical prediction [27, 108] and experimental realization [109, 110] of the topological insulators $Bi_2Se_3$ and $Bi_2Te_3$, many scientists have started to study materials with potential two- and three-dimensional topological properties [32, 36, 111]. Topological insulators are regular insulators in the bulk with gapless metallic states on the surface. Those metallic states emerge as linear dispersive bands within the bulk bandgap [34], forming the Dirac cone. They are spin-polarized [112] and topologically protected by time-reversal symmetry [113,114]. These properties are responsible for electric conduction without dissipation and robustness to defects at the surface [113, 114].

Bismuth-chalcogenides are known as the second generation of topological insulators. Their atomic structure is based on the stacking of atomic sheets disposed in a hexagonal in-plane arrangement [115, 116]. Groups of five atomic layers form a structure called quintuple-layer (QL), composed by a X-M-X-M-X stacking where X = Se, Te and M = Bi, Sb; see figure 3.1. The quintuple-layers are bounded by van der Walls forces [115], making $M_2X_3$ crystals easily to be cleaved along the direction perpendicular to the atomic layers. Main examples are $Bi_2Se_3$, $Bi_2Te_3$ and $Sb_2Te_3$. The leading properties of regular topological insulators are present in this class, except $Sb_2Se_3$ that has an semiconducting energy gap with no surface states [34].

The dependence between topological properties and crystalline structure in these compounds [116–119] has an important role in the experimental realization of new topological materials. Considerable efforts were done with the investigation of the topological properties in ternary [120, 121] and quaternary [122] compounds. Former measurements

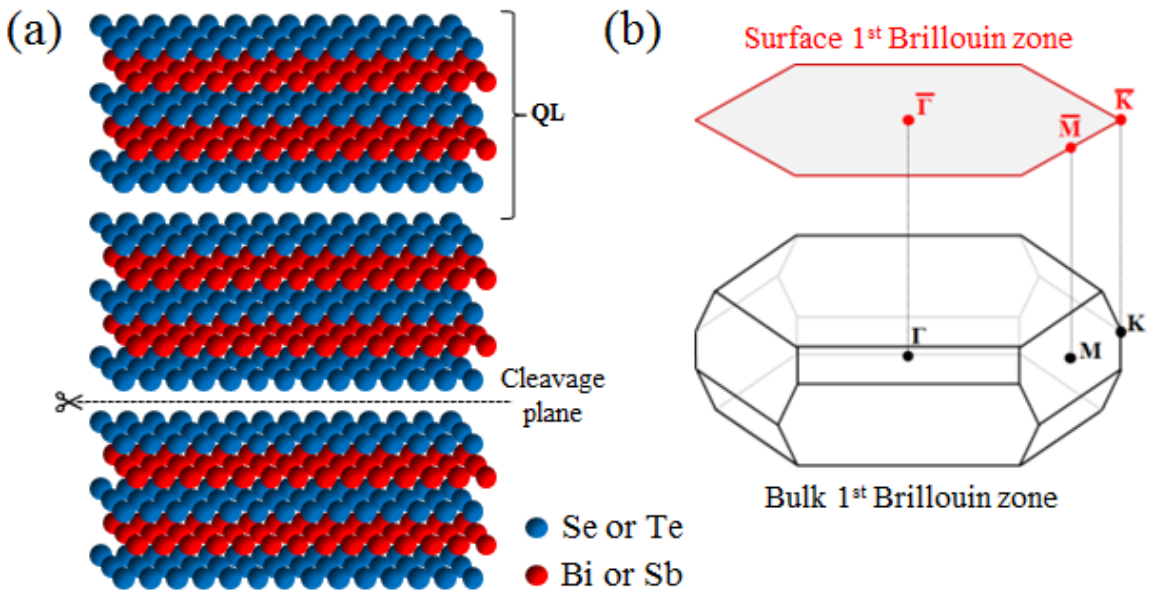


Figure 3.1 – Crystalline structure of Bi-Chalcogenides. (a) Atomic arrangement of $M_2X_3$ crystals evidencing the quintuple-layers and the cleavage plane. (a) Bulk and surface first Brillouin zones of this class with high-symmetric points.

found in the literature evidenced a strong dependence between Se/Te ratio and Dirac cone position in $Bi_2Se_{3-x}Te_x$ [123]. A resembling behaviour related to the Bi/Sb ratio was found in the series $Bi_{2-x}Sb_xTe_3$ [124] and $Bi_{2-x}Sb_xSe_3$ [125]. It was also reported a coexistence of rhombohedral and orthorhombic structure in $BiSbSe_3$, leading to the extinction of the topological property. The increasing of Antimony in $Bi_{2-x}Sb_xSe_3$ is responsible for the transition from hexagonal to orthorhombic [117, 126], although theoretical investigations indicated that the addition of a few amount of Tellurium in this system is sufficient to stabilize the rhombohedral structure [127]. An idealistic picture of a topological insulator prescribes the Dirac point placed at the Fermi level. This feature is scarcely observed in photoemission experiments. Intrinsic vacancies are responsible for heighten the Fermi level of these materials [128, 129]. The standard approach to reach the ideal situation is doping the material to control the Fermi level position [128]. The substitutions Bi $\rightarrow$ Sb and Se $\rightarrow$ Te are also another source of electron vacancies [125, 130] wherefore the Fermi level can also be tunned by the controlling of the Bi/Sb and Se/Te ratios in a quaternary compound.

## 3.2 Synthesis and Characterization of $BiSbSe_{2.5}Te_{0.5}$

$BiSbSe_{2.5}Te_{0.5}$ crystals were produced using the Bridgman method [131], see figure 3.2. The powder mixture of the four elements (Bismuth, Antimony, Tellurium and Selenium) with the expected molar proportions (1:1:0.5:2.5) were placed in an evacuated and sealed

quartz tube with pressure lower than $10^{-5}$ mbar. The tube was heated in a temperature-controlled furnace up to 1000 K at a temperature rate of 5K/min and remained at the final temperature for 30 hours. After natural cooling to room temperature during approximately 24 hours, single crystals of $BiSbSe_{2.5}Te_{0.5}$ were produced.

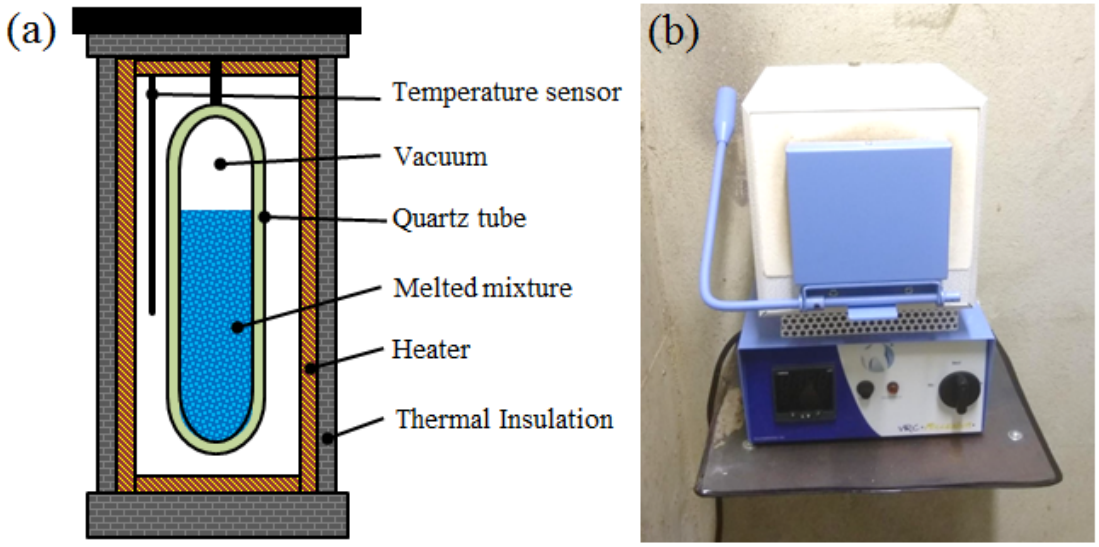


Figure 3.2 – The Bridgman method for crystal growth. (a) Representation of the Bridgman system. An evacuated quartz tube with the mixture of the elements are place inside a temperature-controlled furnace where the mixture is heated until it starts melting. After natural cooling of the system, crystals are formed inside the tube, see [131]. (b) Picture of the furnace in the UHV Nanoscopy Laboratory in UFMG where the samples were grown.

The formation of single crystalline samples were confirmed by X-ray Diffraction (XRD) measurements of powdered pieces using an Empyrean Panalytical X-ray diffractometer with a Cu-tube source. The diffraction data is shown in figure 3.3. Since there is no information about the crystalline structure of $BiSbSe_{2.5}Te_{0.5}$ crystals in the literature, the identification of diffraction peaks was done proposing a $Bi_2Se_3$ structure, where the atomic scattering factors of Bi and Se were replaced by the equivalent Bi/Sb and Se/Te ratios, respectively 1:1 and 2.5:0.5. Almost all diffraction peaks were identified as belonging to the proposed structure. The obtained lattice parameters are: $a = (0.43 \pm 0.01)$ nm and $c = (2.859 \pm 0.001)$ nm, where $a$ is the in-plane lattice parameter and $c$ is the out-of-plane lattice parameter.

X-ray diffraction measurements provide statistical information about the crystalline structure of the sample. Details about the single-crystalline construction are obtained by the local information provided by microscopy techniques. Transmission Electron Microscopy (TEM) experiments were employed resulting in a confirmation that the sample is mostly composed by a single-phase crystal, precisely $BiSbSe_{2.5}Te_{0.5}$. A TEM image of a $BiSbSe_{2.5}Te_{0.5}$ grain is shown in figure 3.4. TEM experiments were carried out in

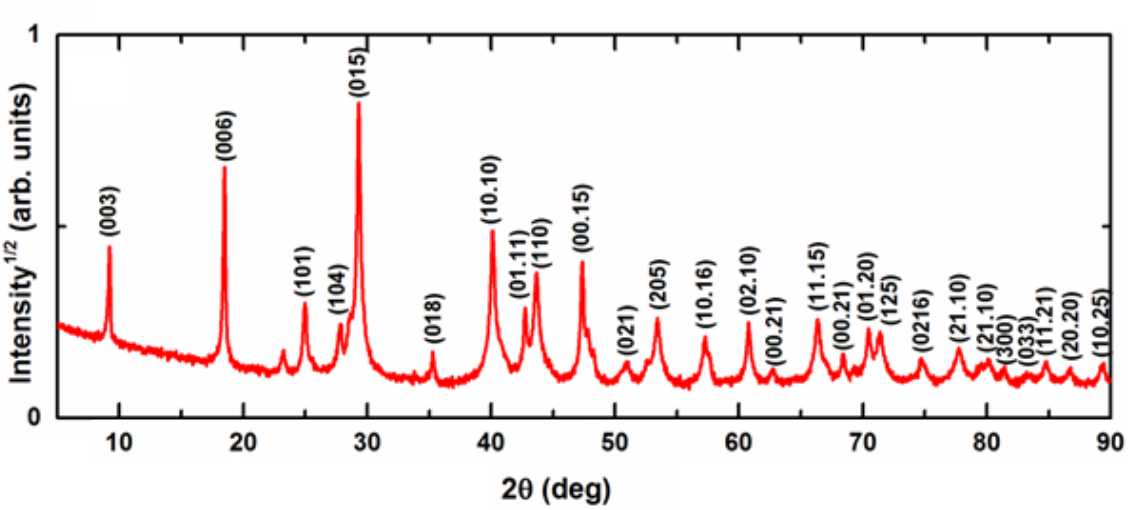


Figure 3.3 – X-Ray diffraction data of $BiSbSe_{2.5}Te_{0.5}$. The indexed diffraction peaks belong to a proposed $Bi_2Se_3$ structure, where the atomic scattering factors of Bi and Se were replaced by the equivalent Bi/Sb (1:1) and Se/Te (2.5:0.5) ratios.

a FEI-Termofisher Tecnai G2-20 microscope with a $LaB_6$ filament, operating at 200 kV. The result on the right side of figure 3.4 is a selected area electron diffraction (SAED) data acquired from a 100 nm$^2$ spot (red circle in figure 3.4), confirming the formation of single-phase crystalline structures in the sample. A variety of other grains were measured with the same result.

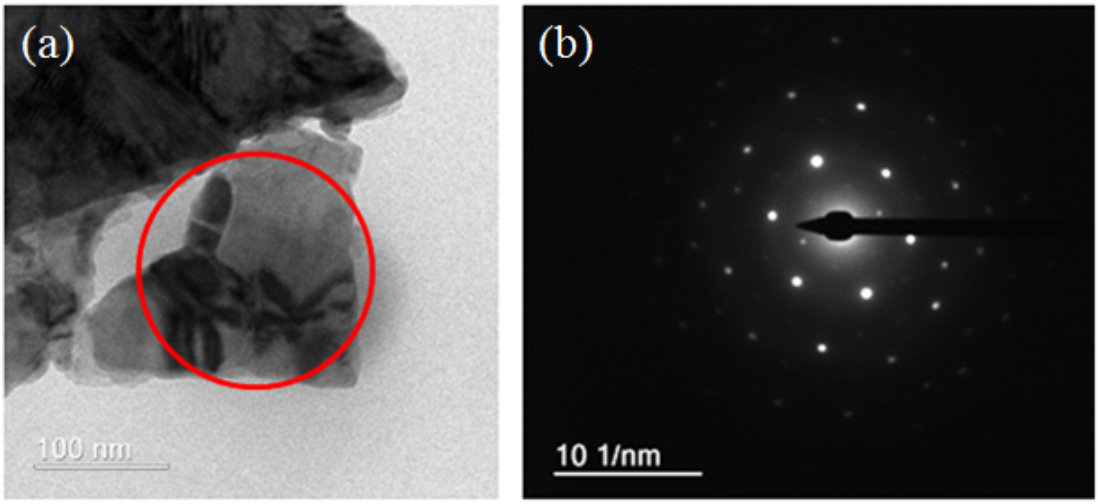


Figure 3.4 – Microscopy measurements of $BiSbSe_{2.5}Te_{0.5}$. (a) Transmission Electron Microscopy image of an individual $BiSbSe_{2.5}Te_{0.5}$ grain. (b) Selected area electron diffraction (SAED) image acquired from the region delimited by the red circle.

The characterization of the crystalline structure is not sufficient to confirm the formation of $BiSbSe_{2.5}Te_{0.5}$ single crystals, a chemical analysis is also mandatory. The chemical composition of the sample was determined by X-ray photoelectron spectroscopy

(XPS). XPS data were obtained in an UHV system equipped with a Al X-ray source and a SPECS Phoibos 100 electron analyzer. The experiment was carried out under room temperature, in a base pressure lower than $6.0 \times 10^{-10}$ mbar. The energy resolution was approximately 0.8 eV. Figure 3.5 shows the resulted data evidencing core-level peaks from each element present in the sample. Typical Gaussian plots were employed to render a quantitative analysis of the photoemission spectra of each element.

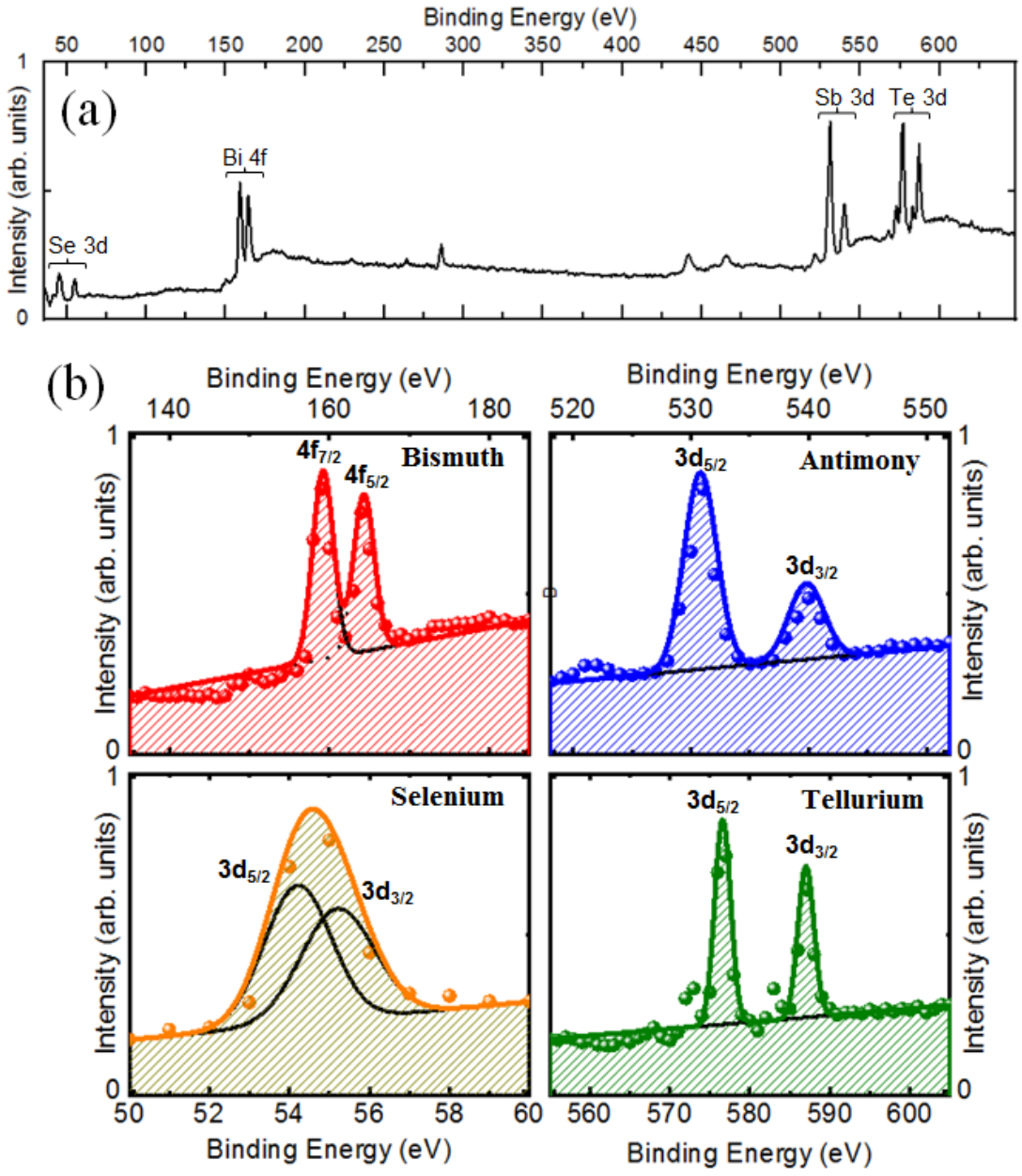


Figure 3.5 – X-ray photoelectron spectroscopy data obtained from $BiSbSe_{2.5}Te_{0.5}$. (a) XPS data evidencing photoemission peaks of each element. (b) Insets of the photoemission peaks: Bismuth 4f, Antimony 3d, Selenium 3d and Tellurium 3d. Typical Gaussian curves are employed to render a quantitative analysis of the chemical composition of the sample. Experimental data is represent by dots, while solid lines represent the calculated curves.

The result of the qualitative analysis is shown in Table 1. Small deviations from the regular peak positions [70] where observed. This effect indicates the absence of segregation of any chemical component, in agreement with the crystalline characterization of the sample. The amount of each chemical component is estimated by the intensity of each photoemission peak. The ratio between the number of atoms ($n$) of two elements is:

$$\frac{n_1}{n_2} = \frac{I_1/S_1}{I_2/S_2} \tag{3.1}$$

Where $I_1$, $I_2$ are the intensity of the photoemission peaks and $S_1$, $S_2$ are the atomic sensitivity factor [70], which varies depending on the element and the selected peak. The general expression for the atomic fraction of any constituent in a sample ($C_x$) is given by:

$$C_x = \frac{n_x}{\sum n_i} \tag{3.2}$$

The accurate stoichiometry obtained from this method is $Bi_{0.9\pm0.1}Sb_{1.1\pm0.1}Se_{2.5\pm0.1}Te_{0.5\pm0.1}$. It represents a (Bi,SB):(Se,Te) ratio of approximately 2:3, as expected.

| **Element – Peak** | **Position (eV) ± 0.5 eV** | **Position Lit. (eV) ± 0.1 eV** | **Atomic % ± 2 %** | **Nominal atomic %** |
|---|---|---|---|---|
| **Bismuth – Bi $4f_{7/2}$** | 157.0 | 159.2 | 18.9 | 20.0 |
| **Antimony – Sb $3d_{5/2}$** | 528.0 | 530.8 | 21.6 | 20.0 |
| **Selenium – Se $3d_{5/2}$** | 54.0 | 56.0 | 49.1 | 50.0 |
| **Tellurium – Te $3d_{5/2}$** | 573.0 | 576.6 | 10.4 | 10.0 |

Table 1 – X-ray photoelectron spectroscopy results of $BiSbSe_{2.5}Te_{0.5}$.

The uniform distribution of the four elements over the sample was verified carrying out Electron Energy Loss Spectroscopy (EELS) measurements, an experimental technique where the sample is exposed to a electron beam with a limited range of kinetic energies. The energy loss measured by an spectrometer is interpreted as inelastic scattering and/or absorption from the atomic constituents of the sample, which provides information about the chemical distribution of the elements in the sample. Energy filtered Transmission Electron Microscopy (EFTEM) images of an ordinary grain were obtained using a Spectrum Imaging tool, which generates a spatially-resolved distribution of the EELS data, see figure 3.6. Each colored EFTEM image were acquired using energies from the absorption borders of each element. The combination of XPS and EELS experiments completes the chemical characterization of $BiSbSe_{2.5}Te_{0.5}$, proving that the sample is uniquely composed by a $BiSbSe_{2.5}Te_{0.5}$ single crystal.

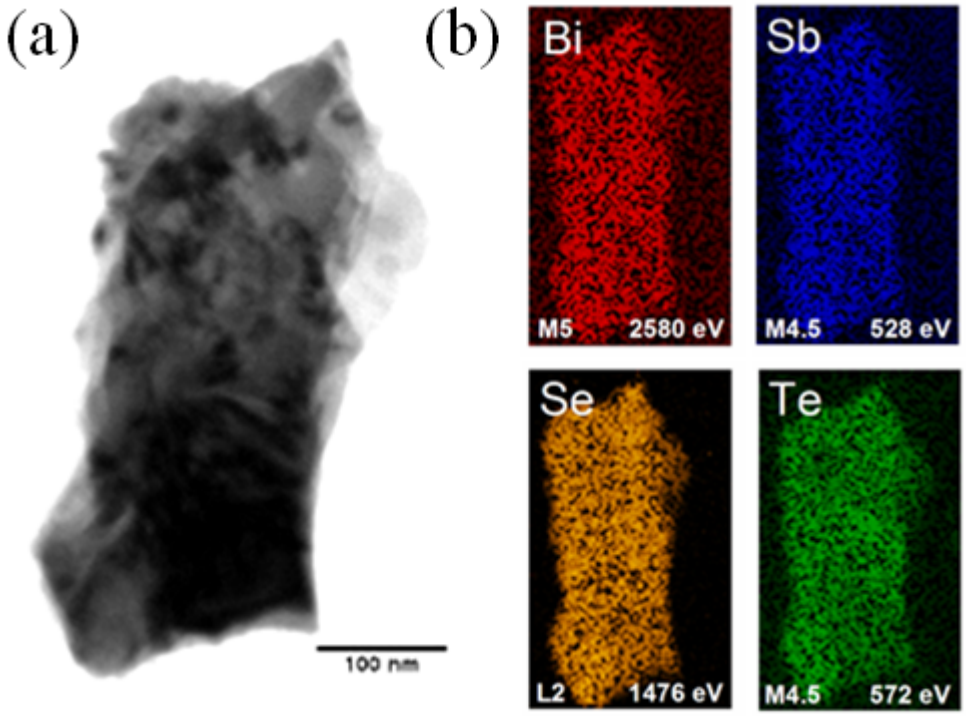


Figure 3.6 – Energy Filtered TEM images of $BiSbSe_{2.5}Te_{0.5}$. (a) A regular TEM image of an individual grain. (b) Energy filtered TEM images of the same grain taken from the absorption energy of each element.

## 3.3 Topological Surface States of $BiSbSe_{2.5}Te_{0.5}$

The electronic properties of $BiSbSe_{2.5}Te_{0.5}$ were studied by Angle-Resolved Photoemission Spectroscopy (ARPES). The experiment was carried out in the PGM beamline of the Brazilian Synchrotron Light Laboratory (LNLS) using a fixed photon energy of 103.5 eV with linear horizontal polarization. The base pressure during the experiment was maintained lower than $5.0 \times 10^{-10}$ mbar and the temperature was fixed at 87 K. The energy-momentum maps were obtained using a SPECS Phoibos 150 electron analyzer with energy resolution of 10 meV and angular resolution of approximately 0.2°. Figure 3.7 shows the energy-momentum maps of $BiSbSe_{2.5}Te_{0.5}$ and $Bi_2Se_3$ for comparison. It was observed the presence of almost linear surfaces states crossing the Fermi level in both samples. The separation between Fermi level and Dirac point positions in $Bi_2Se_3$ is around 0.37 eV. This mismatch is caused by Selenium vacancies on the surface of the material, causing a n-type doping, coherent with previous measurements found in the literature [112, 128, 129]. The separation between Fermi level and Dirac point position observed in $BiSbSe_{2.5}Te_{0.5}$ was 0.22 eV. The addition of Antimony and Tellurium to the $Bi_2Se_3$ matrix was demonstrated to induce a p-type doping in the system, reducing the Fermi level-Dirac point separation by 0.15 eV.

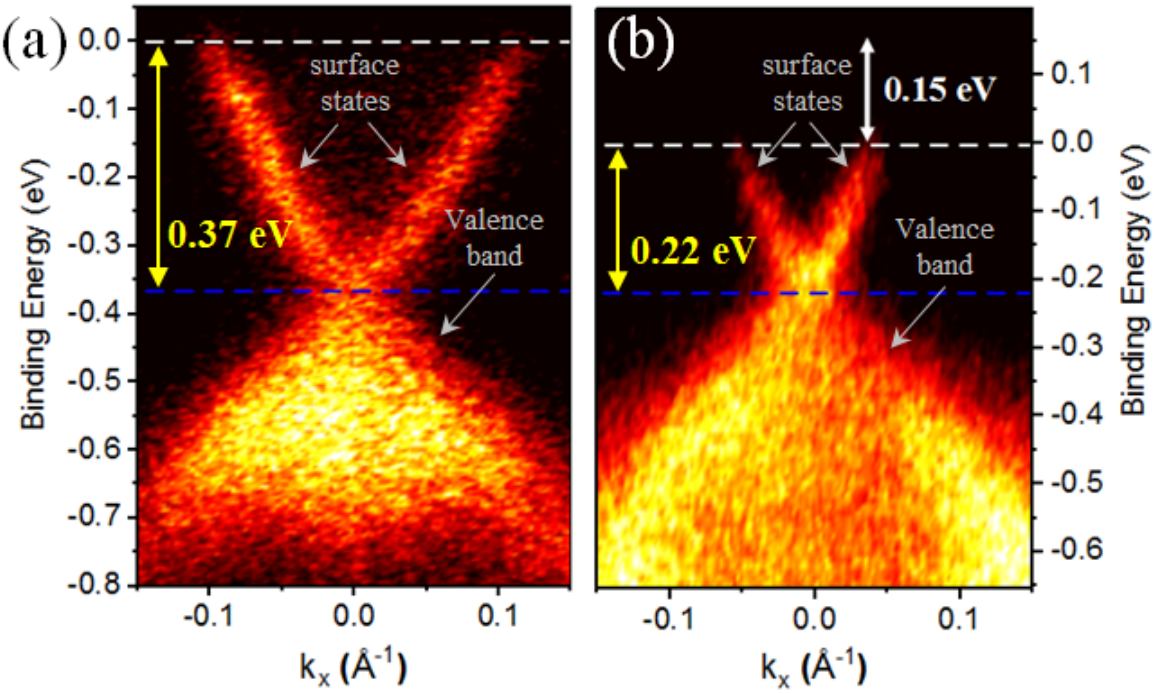


Figure 3.7 – Angle-Resolved Photoemission Spectroscopy of $Bi_2Se_3$ and $BiSbSe_{2.5}Te_{0.5}$. Energy-momentum maps of (a) $Bi_2Se_3$ and (b) $BiSbSe_{2.5}Te_{0.5}$. Fermi and Dirac point levels are marked by white and blue dotted lines, respectively.

The effect of Antimony doping in the separation between Fermi level and Dirac point positions was studied before in the $Bi_{2-x}Sb_xTe_3$ [124, 132] and $Bi_{2-x}Sb_xSe_3$ [125] series. In both cases, the Fermi level moves towards the Dirac point level (p-type doping) as the amount of Antimony increases. For instance, the increasing of the Antimony content in $Bi_{2-x}Sb_xTe_3$ from $Bi_2Te_3$ (x = 0) to $BiSbTe_3$ (x = 1) reduces the separation in 0.07 eV. Above x = 1.5, $Bi_{2-x}Sb_xTe_3$ becomes a conventional conductor. In the $Bi_{2-x}Sb_xSe_3$ [125] series, the Antimony doping effect is even stronger. An increase from x = 0 to x = 0.3 moves the Fermi level around 0.1 eV towards the Dirac point level. The investigation regarding the Se/Te substitution in $Bi_2Se_{3-x}Te_x$ demonstrates interesting observable effects. As well as the previous systems, the increasing of Tellurium reduces the separation between Fermi level and Dirac point positions. Although it also induces an apparent nesting of the Dirac cone into the valence band [123, 130]. This result was not surprising since the main difference between the bandstructure of $Bi_2Se_3$ and $Bi_2Te_3$ is the nesting of the Dirac point inside the bulk valence band in $Bi_2Te_3$. From $Bi_2Se_3$ (x = 0) to $BiSeTe_2$ (x = 2), the top of the valence band moves 0.28 eV towards the Fermi level, completely nesting the Dirac point. For comparison, ARPES measurements carried out with the quaternary sample $BiSbSe_2Te$ [122] indicated a separation of 0.31 eV between Fermi level and Dirac point positions, a difference of 0.09 eV compared with $BiSbSe_{2.5}Te_{0.5}$.

From the analysis of the metallic surface states, important information are obtained about the bandstructure of $BiSbSe_{2.5}Te_{0.5}$. The effective mass ($m^*$) of the electrons on the

surface is evaluated using a semi-classical approach, which associates them to electron wave-packets [133]. The electron velocity ($v_e$) is associated with the group velocity ($v_g$) of the corresponding wave-packet:

$$v_e = v_g \simeq \frac{1}{\hbar}\frac{\partial E}{\partial k} \tag{3.3}$$

Where $\partial E/\partial k$ is obtained from the slope of the surface states, see figure 3.8. The final expression for the electron velocity is:

$$v_e \simeq \frac{E_D}{\hbar k_F} \tag{3.4}$$

Where $E_D$ is the Dirac point level and $k_F$ is the Fermi momentum. The semi-classical argument associates the electron group velocity to the crystalline momentum $\hbar k$. In other words, the electron effective mass evaluated at the Fermi level is given by:

$$m^* \simeq \frac{\hbar k_F}{v_e} = \frac{\hbar^2 k_F^2}{E_D} \tag{3.5}$$

The theoretical expression for the electron effective mass commonly used in solid state physics implies a divergent effective mass for the linear dispersion of the topological surface states, since it is associated with the second derivative of the energy-momentum relation, $m^* = \hbar^2(\partial^2 E/\partial k^2)^{-1}$. This expression is obtained assuming a parabolic dispersion and therefore should not be applied to linear dispersions. The semi-classical approximation provides an expression that is compatible with arbitrary dispersions and also consistent with the cyclotron mass [133]. The resulting electron effective masses and the other relevant quantities obtained for both $Bi_2Se_3$ and $BiSbSe_{2.5}Te_{0.5}$ are shown in Table 2. It was obtained an electron effective mass for $BiSbSe_{2.5}Te_{0.5}$ that is two times smaller than for $Bi_2Se_3$. Those values are in agreement with experimental results [112] and theoretical calculations for a similar stoichiometry ($BiSbSe_2Te$) [134].

| **Sample** | **$E_D$ (± 0.01 eV)** | **$k_F$ (± 0.01 Å$^{-1}$)** | **$v_e$ (± 0.02 x 10$^5$ m/s)** | **m* (± 0.02 $m_e$)** |
|---|---|---|---|---|
| **$Bi_2Se_3$** | 0.37 eV | 0.09 Å$^{-1}$ | 6.2 x 10$^5$ m/s | 0.16 $m_e$ |
| **$BiSbSe_{2.5}Te_{0.}$** | 0.22 eV | 0.05 Å$^{-1}$ | 6.6 x 10$^5$ m/s | 0.08 $m_e$ |

Table 2 – Comparison between $Bi_2Se_3$ and $BiSbSe_{2.5}Te_{0.5}$ for Dirac point level - $E_D$, Fermi momentum - $k_F$, electron velocity - $v_e$ and effective mass - $m^*$.

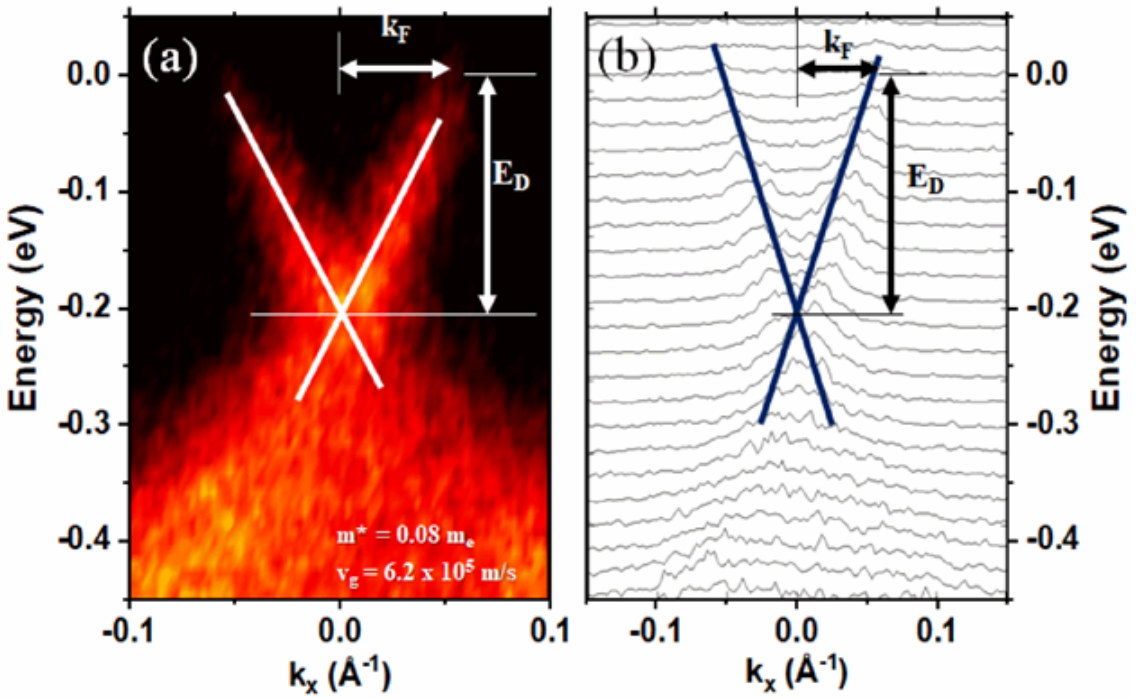


Figure 3.8 – Evaluation of the electron effective mass of $BiSbSe_{2.5}Te_{0.5}$. (a) ARPES energy-momentum map evidencing the linear dispersion of the surface states. (b) Momentum dispersive curves of $BiSbSe_{2.5}Te_{0.5}$ from where was obtained the Dirac point level ($E_D$) and the Fermi momentum ($k_F$). Electron velocity ($v_e$) and effective mass ($m^*$) where obtained using equations 3.4 and 3.5, respectively.

In summary, ARPES experiments were used to characterized the electronic band-structure of $BiSbSe_{2.5}Te_{0.5}$, particularly the topological surface states. When compared with a $Bi_2Se_3$ reference sample, it was observed a positive doping of 0.15 eV with the preservation of the bulk band gap and the metallic surface states. The evaluation of the Dirac point level and the Fermi momentum of both samples presented an electron effective mass for $BiSbSe_{2.5}Te_{0.5}$ that is two times smaller than $Bi_2Se_3$.

# Chapter 4

# Topological States in the CDW Compound $TaTe_4$

## 4.1 Basics of Charge Density Waves

Charge-density waves (CDW) are collective excitations present in materials with large anisotropy. These excitations are created by electron-photon interactions that lead to a new ground state in the material. The instability of one-dimensional materials at low temperature is responsible for inducing that novel phenomenon. Charge density waves are characterized by a collective mode in the charge density formed by electron-hole pairs. The associated charge density is given by

$$\rho(\mathbf{r}) = \rho_0 + \rho_1 \cos 2k_F \cdot \mathbf{r} + \phi \tag{4.1}$$

where $\rho_0$ is the unperturbed electron charge density of the material, $k_F$ the Fermi-momentum and $\phi$ just a phase term. The main consequence of this excitation is the opening of an energy gap in the former metallic bandstructure. In two- and three-dimensional systems, the electron-phonon coupling is responsible for instabilities on the Fermi surface of the materials [135]. The charge-density wave occurs when many electrons are excited with the same wave vector $q = 2k_F$. If all electrons are excited by this $q$ vector, they produce a perfect nesting of the Fermi surface, see figure 4.1. This perfect nesting is only achieved on ideal one-dimensional systems, where all states are connected by the nesting vector $q = 2k_F$. For realistic high-dimensional materials, only some particular regions of the Fermi surface are nested.

The mechanism of the energy gap formation in CDW systems can be easily understood by considering a one-dimensional crystal composed by N identical atoms. The lattice constant is $a$, so the size of the crystal is $L = Na$. The energy gap appears at the reciprocal lattice point $\pi/a$ and there are 2N states available for the first Brillouin zone

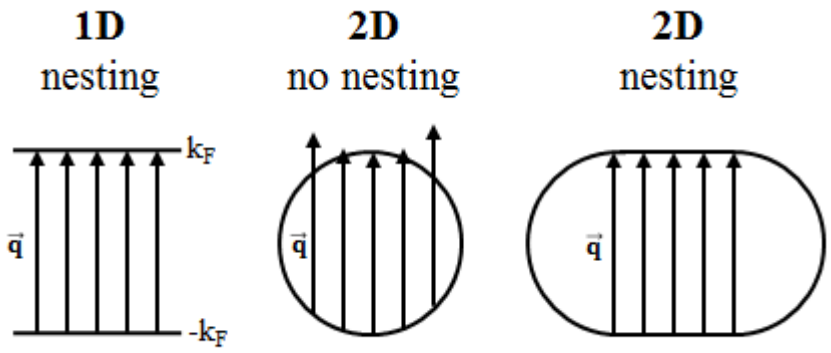


Figure 4.1 – q-vector nesting on 1D and 2D Fermi surfaces. The perfect nesting is only achieved on 1D Fermi surfaces. 2D and 3D Fermi surfaces can only be partially nested by the q-vector.

$(-\pi/a$ to $\pi/a)$, see figure 4.2. If there is one available electron per atom, the energy band is half-filled and the material is metallic. Supposing a small displacement every two atoms, the system acquires a new periodicity – $2a$. The result is an energy gap at $k = \pi/2a$, converting the material to an insulator.

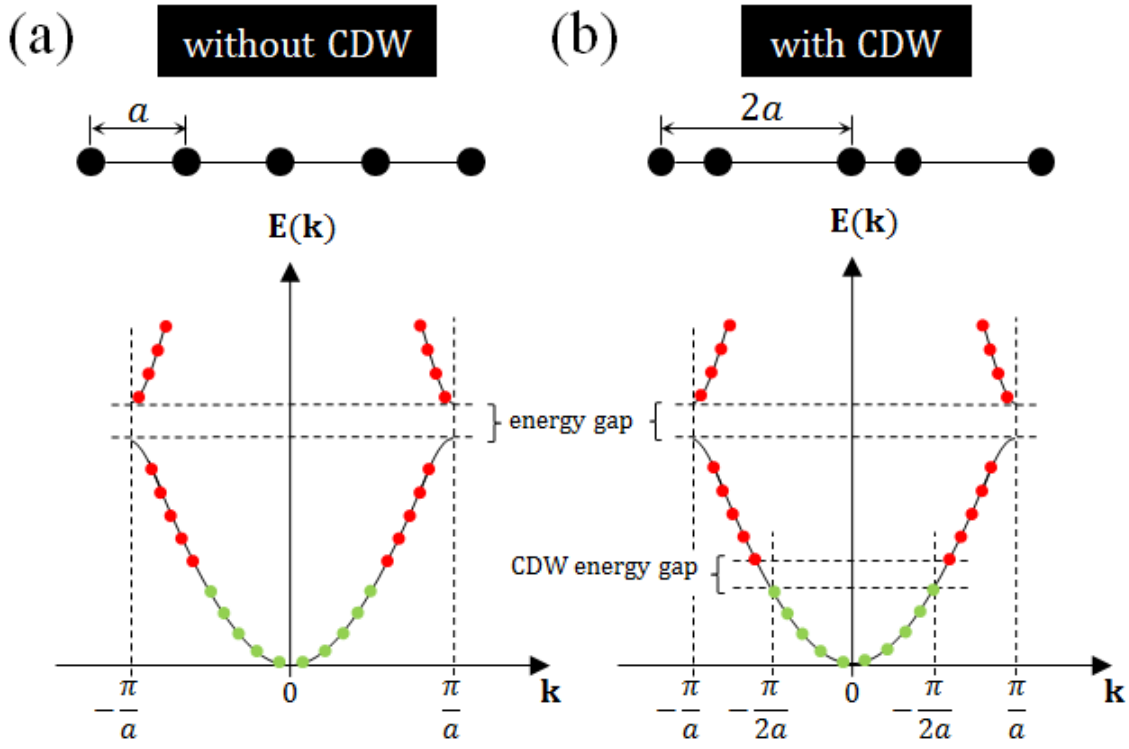


Figure 4.2 – Energy gap formation in CDW systems. (a) In the absence of a CDW, a one-dimensional crystal with lattice constant $a$ has its valence band completely filled. (b) In the presence of a CDW, atomic dislocations in the lattice produce a new periodicity - $2a$, and there is an energy gap associated with the CDW.

Charge density waves are investigated nowadays for a wide range of low-dimensional materials. The increasing interest is related to metal-to-insulator transitions [136] and the search for superconducting phases [137]. The so-called quasi-1D transition metal tetrachacogenides are paradigmatic examples. Some materials as $NbTe_4$ and $TaTe_4$ present CDW at room temperature [138] and pressure-induced superconductivity [139, 140].

## 4.2 Quasi-1D Transition Metal Tetra-Chalcogenides

Since the discovery of topological states in solids in the last decade [32], the usual separation between metals, semiconductors and insulators has been modified. Semiconductors [141], topological insulators [32] and semimetals [142], superconductors [72] and an extended set of intriguing phases of matter [143] have made the field of transport physics much more complex. An interesting class of materials to study new electronic phenomena are the transition metal chalcogenides (TMC). TMCs are formed by the combination of transition metal atoms with chalcogen ones (usually Selenium, Tellurium or Sulfur). Their layered structure creates a favorable environment for the appearance of distinct features related to dimensionality. The most common compounds of this class are the transition metal dichalcogenides [144]. Remarkable properties were observed, related to semiconductors and new topological phases of matter. The most notorious examples are the semiconductor $MoS_2$ [145, 146], the Weyl semimetal $MoTe_2$ [147] and the superconductor $NbSe_2$ [148, 149]. TM trichalcogenides [150] and tetrachalcogenides [151] represent an opportunity in the search for new interesting phenomena. Among these compounds, the quasi-1D transition metal tetrachalcogenides stand out.

The atomic structure of quasi-1D TM tetrachalcogenides is composed by linear chains of metallic atoms surround by chalcogen atoms [138]. That specific construction has important implications for the electronic behavior of these materials. The formation of a quasi-1D structure produces features that only would be observed in a theoretical one-dimensional crystal, as charge density waves (CDW) [152] and spin density waves (SDW) [153]. Some of the most important quasi-1D TM tetrachalcogenides are $TaTe_4$ [138], $NbTe_4$ [138], $(TaSe_4)_2I$ [154, 155] and $(NbSe_4)_2I$ [156]. Recent important discoveries are the pressure-induced superconductivity in $TaTe_4$ [140] and $NbTe_4$ [139] and the realization of an axion insulator in $(TaSe_4)_2I$ [62].

## 4.3 Experimental background of $TaTe_4$

The crystalline structure of $TaTe_4$ is composed by linear chains of Ta atoms surrounded by eight Te atoms in a square anti-prismatic coordination, see figure 4.3. The

unit cell is tetragonal (P4cc, space group no. 103) with lattice constants $a = 6.514$ Å and $c = 6.809$ Å [157], where $c$ is the chain direction. Lattice distortions in the Ta chains are responsible for a CDW transition at 475 K [138]. Below this temperature, a commensurately modulated (2a,2a,3c) structure is observed. $TaTe_4$ has also been described as a topological semimetal [158–160], making it an ideal system to investigate the relationship between CDWs and topological states in low-dimensional systems.

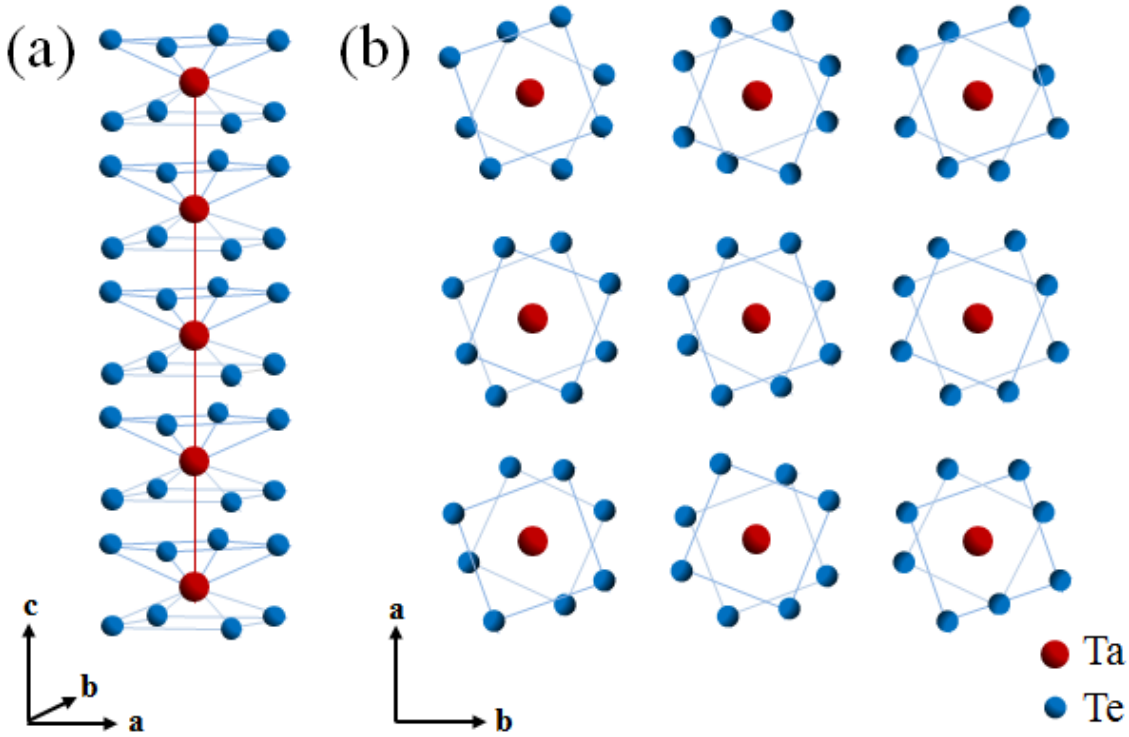


Figure 4.3 – Crystalline structure of $TaTe_4$. (a) Crystal viewed along $c$-axis evidencing the Ta chains surrounded by Te atoms. (b) Top image of the crystal oriented perpendicular to $c$-axis.

Previous investigations reached different conclusions about the electronic structure of $TaTe_4$. ARPES measurements carried out twenty years ago reported a coexistence of one- and three-dimensional signatures [161]. The photoemission experiment revealed valence states that disperse only along the linear chain direction. They also reported a region of reduced spectral weight 0.3 eV below the Fermi level. Regions of reduced spectral weight are commonly observed in quasi-1D materials since one-dimensional materials should not have a Fermi level cutoff for photoemission experiments [162, 163]. The mentioned work also did not observe any dispersive states crossing the Fermi level. In contrast, magneto-transport measurements done four years ago [158] reported the appearance of a resistivity plateau at low temperature. The resistivity plateau is a signature of topological metallic states. The magnetoresistance observed in $TaTe_4$ is highly anisotropic. It shows an angular dependence that makes the magnetoresistance 40 times bigger when the magnetic field is applied

perpendicular to the chain direction $c$, in comparison with parallel measurements [159]. Shubnikov-de Haas oscillations were also observed at low temperatures [160], resulting in an angular dependence of a 2D Fermi surface. These findings indicate that $TaTe_4$ has a three-dimensional bandstructure with metallic states forming a 2D Fermi surface, unlike what was observed by ARPES experiments. The apparent inconsistency between ARPES and magneto-transport results make a renewed ARPES investigation of $TaTe_4$ highly desirable.

## 4.4 2D Fermi Surface and Topological States of $TaTe_4$

Single crystals of $TaTe_4$ were grown using a self-flux technique [164] by the group of Prof. Paula Giraldo-Gallo at Universidad de Los Andes (Colombia). A mixture containing of 1 mol of elemental Ta and 99 mol of elemental Te was deposited put in an alumina crucibles and sealed in an evacuated quartz tube. The mixture was heated to 700°C, held at this temperature for 12 hours and then slowly cooled to 500°C at a rate of 2°C/hour. The remaining melt was decanted and separated from the $TaTe_4$ crystals using a centrifuge. Silver-colored long rectangular crystals were obtained, with sizes up to 0.1× 0.1×1 $cm^3$. The crystalline structure was confirmed by X-ray powder diffraction carried out with powdered pieces of $TaTe_4$ crystals, see figure 4.4.

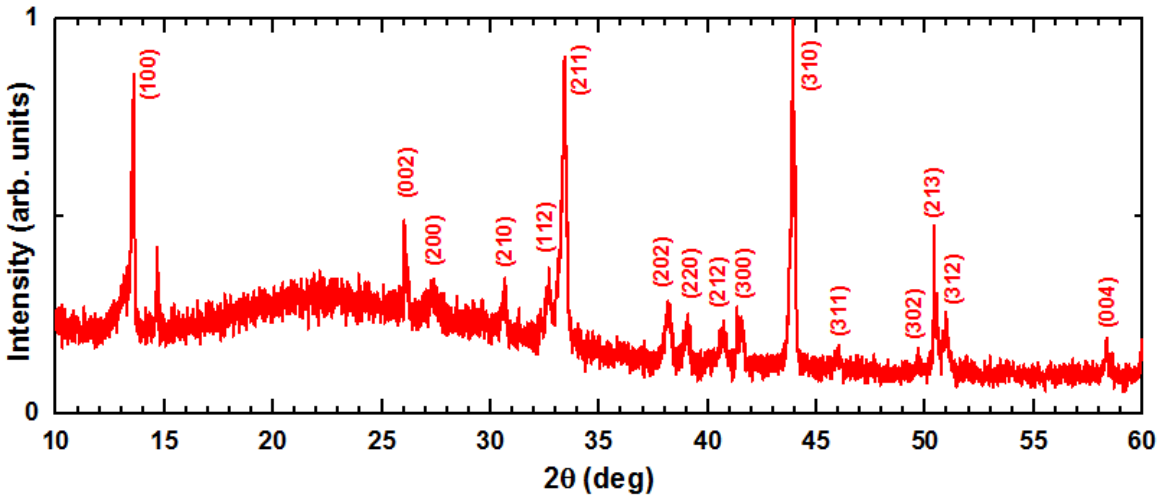


Figure 4.4 – X-ray diffraction data of $TaTe_4$

The energy-momentum dispersion of $TaTe_4$ was obtained by Angle-resolved Photoemission Spectroscopy (ARPES). The experiments were carried out in the CASSIOPEE beamlime of Synchrotron SOLEIL (France) using a fixed photon energy of 75 eV with both linear and horizontal polarization. The base pressure during the experiment was maintained lower than $4.0 \times 10^{-10}$ mbar and the temperature was fixed at 13 K. The

energy-momentum maps were obtained using a Scienta R4000 hemispherical electron analyzer with vertical slits. Typical energy and angular resolutions were 15 meV and 0.25°, respectively. In order to have a pristine surface, the $TaTe_4$ crystal was cleaved in-situ along the [100] direction. This configuration sets the measurement plane formed by directions parallel ($c$) and perpendicular ($b$) to the linear chains, see figure 4.5.

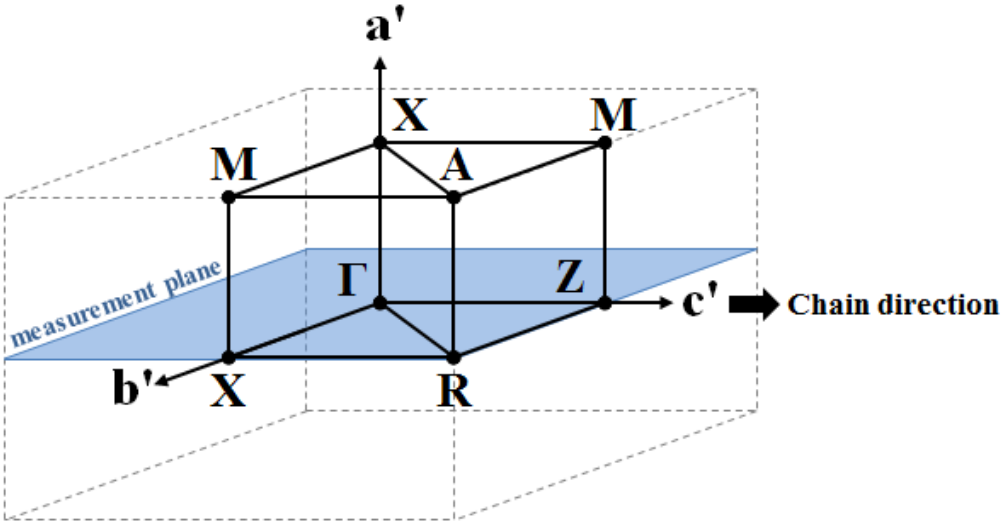


Figure 4.5 – Reciprocal lattice structure of $TaTe_4$ with high-symmetric points. The measurement plane is evidenced along reciprocal directions $b'$ [010] and $c'$ [001], where $c'$ is the reciprocal vector pointing along the linear chain direction.

Figure 4.6 presents energy-momentum maps of $TaTe_4$ obtained along Γ-X and Γ-Z directions. Γ-X is the reciprocal direction associated with the crystalline direction perpendicular to the linear chains, while Γ-Z is the reciprocal direction associated with the crystalline direction parallel to the linear chains. The Γ-Z map is mainly composed by two bands. The upper band has a W-shape centered at Γ and dispersing from approximately -0.3 eV to -0.6 eV, with the band bottom settled at Z. The lower band has a faced-down Y-shape also centered at Γ and dispersing from approximately -0.8 eV to -1.2 eV. The Γ-X map present two overlapping structures: the W-band dispersing from approximately -0.3 eV to -1.0 eV, centered at Γ with the band bottom settled at X; and hole-state centered at X with no symmetric counterpart. The lack of symmetry in this state is explained by matrix elements suppressing the mirroring state on positive momentum values. An important feature observed on both maps is the region with reduced spectral weight near the Fermi level, from 0 eV to approximately -0.3 eV. The photoemission intensity in the region of reduced spectral weight is five times less intense than the valence band. Figure 4.6 shows the angle-integrated photoemission intensity of $TaTe_4$ obtained with the sample at normal emission position. Two sudden decreasing of the spectral weight are observed: the Fermi edge cut-off at 0 eV and a exponential decay starting around approximately 0.3 eV. This exponential decay is a signature of 1D samples, also observed

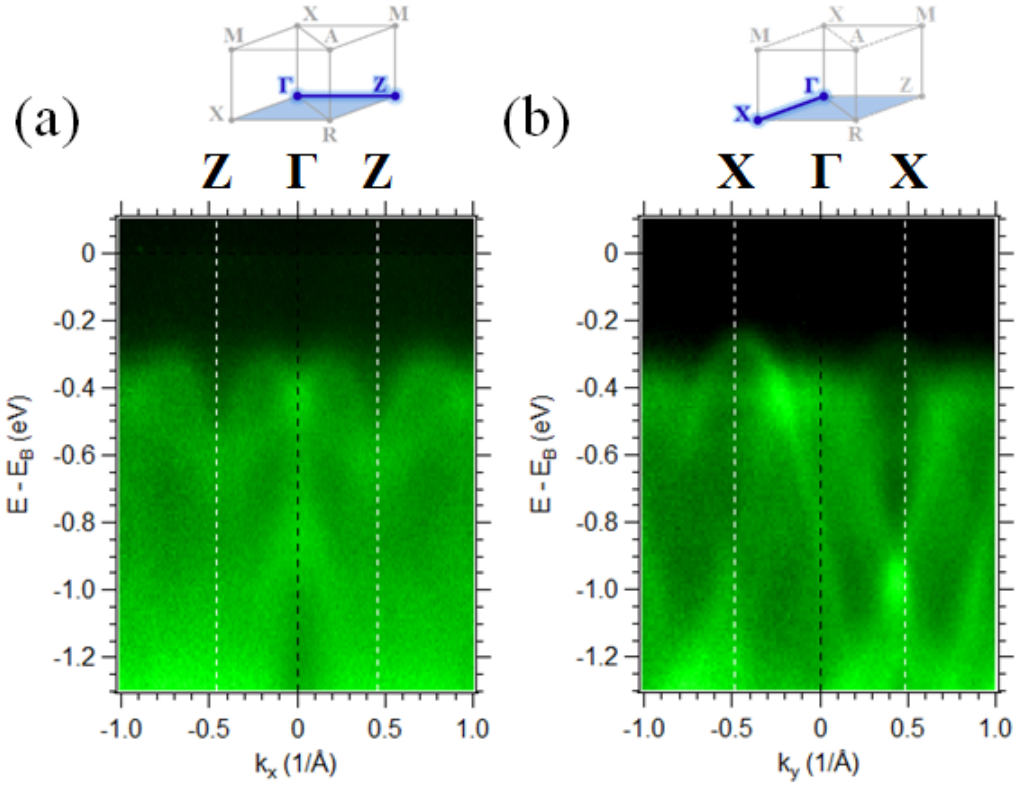


Figure 4.6 – ARPES energy-momentum map of $TaTe_4$ along (a) Γ-Z and (b) Γ-X reciprocal directions. The associated reciprocal direction in the first Brillouin zone is indicated above each energy-momentum map.

in $NbTe_4$ [162], $(NbSe_4)_3I$ [162] and $(TaSe_4)_2I$ [163]. These results reproduce with precision the features observed by later ARPES experiments [161], confirming the coexistence of one and three-dimensional signatures in $TaTe_4$.

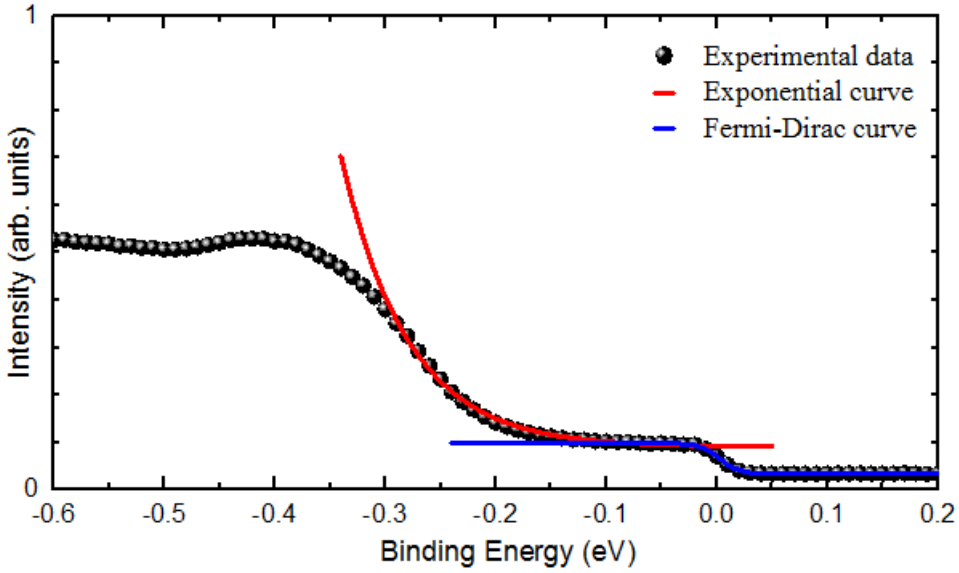


Figure 4.7 – Angle-integrated spectra of $TaTe_4$. Theoretical curves of Fermi-Dirac distribution and exponential decay are represented by red and blue, respectively.

The photoemission intensity observed in Γ-Z and Γ-X maps are apparently uniform in the region of reduced spectral weight, i.e, there is no dispersive states crossing the Fermi level. This finding is in agreement with [161]. In contrast, magneto-transport experiments [158, 159] have suggested the presence of metallic states of topological nature crossing the Fermi level. The divergence is solved employing an analysis of the photoemission intensity along different reciprocal directions. In figure 4.8, the energy-momentum map obtained along the X-R direction present dispersive states crossing the Fermi level. Because of the low photoemission intensity near the Fermi level, the energy-momentum maps were plot in logarithmic scale with saturated contrast to emphasize the region of reduced spectral weight. The energy-momentum map along Γ-Z is also shown for comparison. Dispersive states crossing the Fermi level are clearly observed in the X-R direction. Cone-like states centered at R extending from the valence band to the Fermi level crossing. The presence of these cone-like states crossing the Fermi level provide strong evidences for the classification of this material as a topological material.

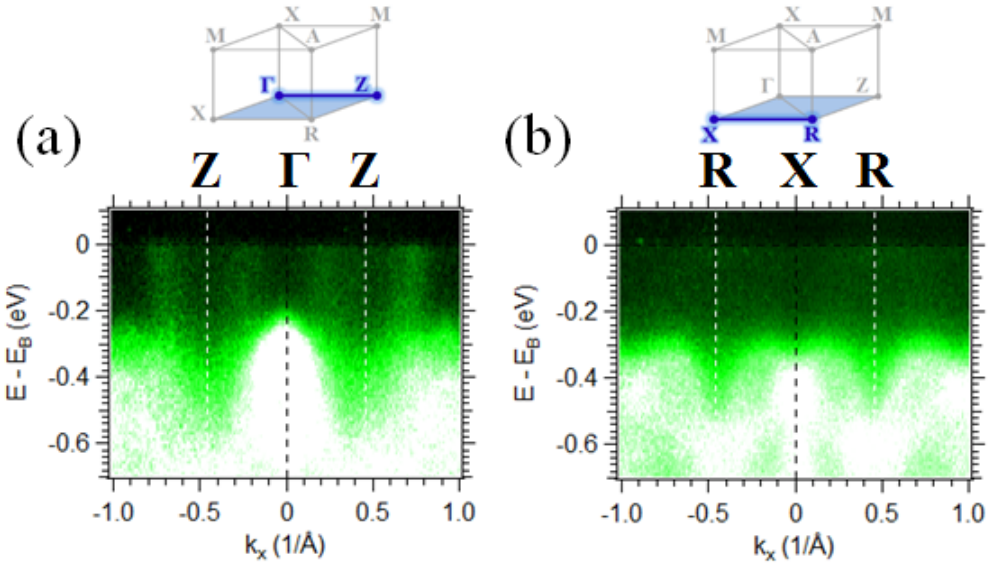


Figure 4.8 – ARPES energy-momentum maps of $TaTe_4$ along (a) Γ-Z and (b) X-R reciprocal directions. Cone-like states crossing the Fermi level are clearly observed in the X-R map.

The in-plane Fermi surface of $TaTe_4$ is shown in figure 4.9. A two-dimensional Fermi surface was predicted by quantum oscillations observed at low temperature [158, 160]. The $k_x$-$k_y$ map revealed the existence of circular orbits in the 2D Fermi surface formed by the cone-like states observed in figure 4.8. $TaTe_4$ has a 2D Fermi surface of a topological material composed by four Dirac/Weyl cones crossing the Fermi level. The flattening of the circular orbits is a consequence of CDW lattice distortion (2x2x3), which stretches the perpendicular direction more than the parallel direction. Furthermore, the 2D Fermi surface also revealed the existence of a quasi-1D state connecting neighboring orbits at approximately $k_y = 0.18$ Å$^{-1}$. Its counterpart is suppressed by matrix elements. The

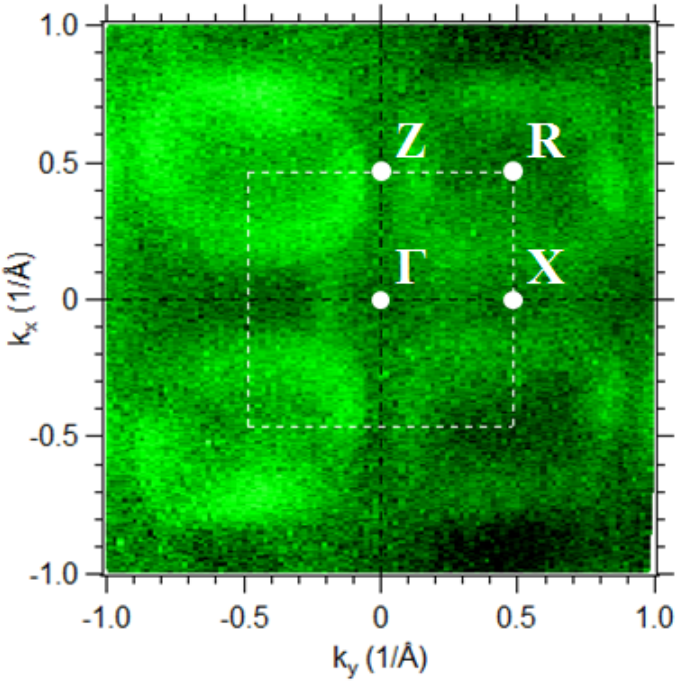


Figure 4.9 – In-plane Fermi surface of $TaTe_4$. The 2D Fermi surface is formed by circular orbits originated from Weyl/Dirac cones crossing the Fermi level. The surface Brillouin zone is highlighted by dashed white lines with the high-symmetry points.

connecting state resembles some characteristics of Fermi-arcs, constant-energy states that connect Weyl/Dirac cones in Weyl/Dirac semimetals [45]. This is particularly important for the electronic characterization of the material as a topological semimetal, instead of a regular topological insulator [140, 158]. The energy-momentum dispersion of the quasi-1D state was characterized by energy-momentum maps taken from perpendicular cuts on the Fermi surface, see figure 4.10. From the energy-momentum map along $k_x = 0$, i.e, crossing perpendicularly the quasi-1D state, it was observed that it maintains a certain relationship with the hole-state observed in figure 4.6. The quasi-1D state seems originated from a band splitting, dispersing from some position inside the valence band. The energy-momentum map taken along $k_y = 0.18$ Å$^{-1}$ reveals the absence of connection between the quasi-1D state and the cone-like states at the Fermi level or any position inside the region of reduced spectral weight. Therefore, the connection must take place at some point inside the valence band.

Fermi arcs usually connect Weyl nodes with a constant-energy contour (Type-I) or tilted Weyl cones with states dispersing in energy (Type-II). The quasi-1D state observed in $TaTe_4$ has a mixture of both features. As the Weyl node is not placed at the Fermi level, the connecting state disperses in energy to appear as a quasi-1D in the Fermi surface. Recently, a new class of Weyl semimetals, named Type-III, was proposed and reported in $(TaSe_4)_2I$ [62, 165]. In those systems, Fermi-arcs connect electron (or hole) pockets in the

Fermi surface. That is another possibility for the characterization of the quasi-1D state as it seems to have a intimate relationship with the hole-state observed in Γ-X map in figure 4.6. The discrimination between both possibilities must be done by finding the connecting point inside the valence band, which is impossible from these measurements as there are many bulk states in the valence band hiding the Weyl node. At the same time, the circular orbits in the 2D Fermi surface cannot be classified as electron pockets, since they overtake the Brillouin zone boundaries. That feature deviates from the description of the Type-III Weyl semimetal reported in $(TaSe_4)_2I$ [62, 165, 166]. However, the similarities between the two systems allow us to continue pursuing the classification of $TaTe_4$ as a new incarnation of Weyl semimetal.

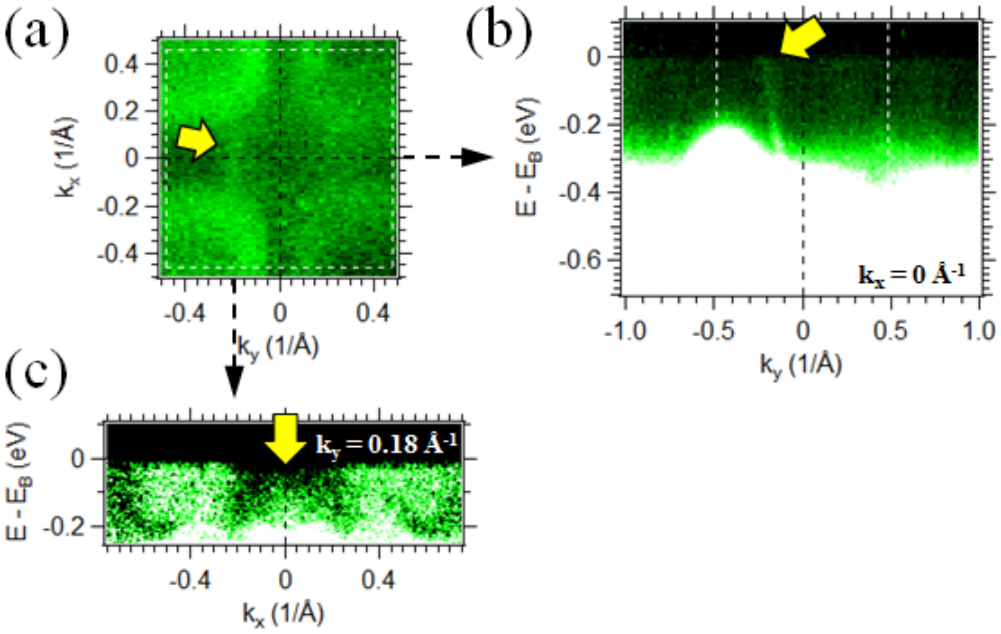


Figure 4.10 – Energy-momentum dispersion of the quasi-1D state. (a) In-plane Fermi surface of $TaTe_4$ evidencing the quasi-1D state connecting neighbouring Weyl/Dirac cones. (b) Energy-momentum map along $k_x = 0$, perpendicular to the quasi-1D state, showing the dispersion in energy of the state as originated from a band splitting with the hole-state observed in the Γ-X map. (c) Energy-momentum map along $k_y = 0.18$ Å$^{-1}$, tangent to the quasi-1D state, revealing the absence of connection with the Weyl/Dirac cones at the Fermi level.

In summary, Angle-resolved photoemission spectroscopy experiments carried out on $TaTe_4$ single crystals revealed the existence of a 2D Fermi-surface. This Fermi surface is composed by circular orbits originated from cone-like states crossing the Fermi level, compatible with topological states of Dirac/Weyl nature. That discovery makes a connection between antagonistic results in the literature [158–161]. The existence of topological features in a quasi-1D compound makes $TaTe_4$ an interesting material to explore the correlation between topology and charge density waves, more specific: the existence of axions in the

material. The existence of charge-density waves in a topological Weyl semimetal could lead to the realization of an axion insulator [57]. These features and the observation of a quasi-1D state on the Fermi surface allow the classification of the material as a topological semimetal and a complete characterization of the quasi-1D is necessary for distinguish between different topological semimetal phases. A theoretical analysis of the electronic structure of $TaTe_4$ is also mandatory.

# Conclusions

The content of this thesis presented the realization of two projects involving the analysis of the electronic structure of topological materials probed by Angle-resolved Photoemission spectroscopy (ARPES). First of all, it was presented a review about the properties of topological materials, more specific: topological insulators and Weyl semimetals. The knowledge about the main concepts associated with the electronic properties of these materials was important for the analysis of the electronic structures presented in the scientific projects of this thesis. Another review was introduced about the experimental technique of ARPES, which is the most powerful tool employed in the characterization of the electronic bandstructure of topological materials. The theory of photoemission was presented in a comprehensive way were the experimental aspects were highlighted. In addition, the apparatus involved with the implementation of an ARPES experiments were also described in detail.

The scientific projects developed during this doctorate were presented in two separated chapters were the data was discussed. The first project addressed the process of structural, chemical and electronic characterization of the topological insulator $BiSbSe_{2.5}Te_{0.5}$. It was shown that the disorder induced by the addition of Sb and Te in the $Bi_2Se_3$ matrix, at the given composition, was not capable to suppress the topological nature of the compound. The Dirac cone observed by ARPES experiment suffered a modification portrayed by chemical doping: electrons move with a smaller effective mass around the Fermi surface with the topological protection still intact. These findings were published in the Journal of Physical Chemistry C in May of 2019, see https://doi.org/10.1021/acs.jpcc.9b01811.

The second project presented in this thesis was related to the quasi-1D transition metal tetrachalcogenide $TaTe_4$. It was measured its energy-momentum dispersions along the most relevant reciprocal lattice directions and a clear image of the in-plane Fermi surface of the material was recovered. The practical interest in this material relies on the fact that it hosts the existence of a charge-density wave in a topological semimetal candidate, which could lead to the realization of an axion insulator. Unfortunately, the

gap-opening observed in this kind of material could not been observed due the localization of the Weyl nodes related to the valence band of the material. Using ARPES, it was possible to visualize the topological Weyl/Dirac cones crossing the Fermi level and the appearance of a quasi-1D electronic state that resembles a Fermi arc. These findings made a connection between divergent results from the literature and opened new questions about the topological nature of the material. An article was written about this project and it is currently under revision of the authors to be submitted to an international scientific journal.

# List of Publications

1 - *Phase separation of Dirac electrons in topological insulators at the spatial limit*. Nano Letters **17**, 97 (2016). https://doi.org/10.1021/acs.nanolett.6b03506
Authors: Carolina Parra, Thiago Henrique Rodrigues da Cunha, Alex W. Contryman, Desheng Kong, Francisco Montero-Silva, Pedro Henrique Rezende Gonçalves, Diogo Duarte dos Reis, Paula Giraldo-Gallo, Rodrigo Segura, Fernanda Olivares, Francis Niestemski, Yi Cui, Rogério Magalhães-Paniago and Hari Manoharan.

2 - *Formation of $Bi_xSe_y$ Phases Upon Annealing of the Topological Insulator $Bi_2Se_3$: Stabilization of In-Depth Bismuth Bilayers*. Journal of Physical Chemistry Letters **9**, (5), 954-960 (2018). https://doi.org/10.1021/acs.jpclett.7b03172
Authors: P. H. R. Gonçalves, Thais Chagas, V. B. Nascimento, D. D. dos Reis, Carolina Parra, M. S. C. Mazzoni, Ângelo Malachias and Rogério Magalhães-Paniago.

3 - *Self-assembled triangular graphene nanostructures: Evidence of dual electronic response*. Carbon **142**, 580-591 (2019). https://doi.org/10.1016/j.carbon.2018.10.059
Authors: Thais Chagas, Marta Pelc, Pedro H. R. Gonçalves, Igor Antoniazzi, Jhon W. Gonzalez, Andres Ayuela, Joao Marcelo J. Lopes, Myriano H. Oliveira Jr., Rogério Magalhães-Paniago and Ângelo Malachias.

4 - *Experimental Realization of a Quaternary Bi-Chalcogenide Topological Insulator with Smaller Effective Mass*. Journal of Physical Chemistry C **123**, 14398 (2019). https://doi.org/10.1021/acs.jpcc.9b01811
Authors: Pedro H. R. Gonçalves, Luan Calil, Igor Antoniazzi, Thais Chagas, Ângelo Malachias, Edmar A. Soares, Vagner E. de Carvalho, Douglas R. Miquita, Rogério Magalhães-Paniago and Wendell S. Silva.

5 - *$Bi_2$:$Bi_2Te_3$ stacking influence on the surface electronic response of the topological*

*insulator* $Bi_4Te_3$. Electronic Structure. **2**, 1, 015002 (2020). https://doi.org/10.1088/2516-1075/ab7398

Authors: Thais Chagas, Guilherme A. S. Ribeiro, Pedro H. R. Gonçalves, Luan Calil, Wendell S. Silva, Ângelo Malachias, Mario S. C. Mazzoni and Rogério Magalhães-Paniago.

# Bibliography


[1] Mendelson, B.: *Introduction to Topology: Third Edition*. Dover Publications, 2012, ISBN 9780486135090. Cited in page 15.

[2] Abate, M. and F. Tovena: *Curves and Surfaces*. Springer Milan, 2012, ISBN 9788847019416. Cited in page 15.

[3] Friedman, M.: *A History of Folding in Mathematics: Mathematizing the Margins*. Springer International Publishing, 2018, ISBN 9783319724874. Cited in page 15.

[4] Bansil, A., H. Lin, and T. Das: *Colloquium: Topological band theory*. Rev. Mod. Phys., 88:021004, 2016. https://doi.org/10.1103/RevModPhys.88.021004. Cited in page 16.

[5] Kittel, C.: *Introduction to Solid State Physics*. Wiley, 2004, ISBN 9780471415268. Cited 3 times in pages 16, 41, and 46.

[6] Vanderbilt, D.: *Berry Phases in Electronic Structure Theory: Electric Polarization, Orbital Magnetization and Topological Insulators*. Cambridge University Press, 2018, ISBN 9781107157651. Cited in page 17.

[7] Jackson, J. D.: *Classical Electrodynamics*. Wiley, 1975, ISBN 9780471431329. Cited 4 times in pages 17, 20, 39, and 45.

[8] Stewart, J.: *Calculus*. Cengage Learning, 2011, ISBN 9781133170693. Cited in page 17.

[9] Franz, M. and L. Molenkamp: *Topological Insulators*. Elsevier Science, 2013, ISBN 9780444633187. Cited 3 times in pages 18, 21, and 28.

[10] Klitzing, K. von: *Quantum Hall Effect: Discovery and Application*. Annu. Rev. Conden. Ma. P., 8:13, 2017. https://doi.org/10.1146/annurev-conmatphys-031016-025148. Cited in page 18.

[11] Hall, E. H.: *On a New Action of the Magnet on Electric Currents*. Am. J. Math., 2:287, 1879. https://doi.org/10.2307/2369245. Cited in page 19.

[12] Klitzing, K. von: *The quantized Hall effect*. Rev. Mod. Phys., 58:519, 1986. https://doi.org/10.1103/RevModPhys.58.519. Cited in page 19.

[13] Yoshioka, D.: *The Quantum Hall Effect*. Springer Berlin Heidelberg, 2013, ISBN 9783662050163. Cited in page 19.

[14] Landau, L. D. and E. M. Lifshitz: *Quantum Mechanics: Non-Relativistic Theory*. Elsevier Science, 1991, ISBN 9780750635394. Cited in page 20.

[15] Ballentine, L. E.: *Quantum Mechanics: A Modern Development*. World Scientific, 2015, ISBN 9789814578578. Cited 3 times in pages 21, 45, and 46.

[16] Mikhailov, S. A.: *A new approach to the ground state of quantum hall systems. basic principles*. Physica B, 299:6, 2001. https://doi.org/10.1016/S0921-4526(00)00769-9. Cited in page 21.

[17] Hatsugai, Y.: *Topological aspects of the quantum Hall effect*. J. Phys. Condens. Mat., 9:2507, 1997. https://doi.org/10.1088/0953-8984/9/12/003. Cited in page 22.

[18] Laughlin, R. B.: *Quantized Hall conductivity in two dimensions*. Phys. Rev. B, 23:5632, 1981. https://doi.org/10.1103/PhysRevB.23.5632. Cited in page 22.

[19] Chakraborty, T. and P. Pietilainen: *The Quantum Hall Effects: Integral and Fractional*. Springer Berlin Heidelberg, 2013, ISBN 9783642793196. Cited in page 22.

[20] Tsui, D. C., H. L. Stormer, and A. C. Gossard: *Two-Dimensional Magnetotransport in the Extreme Quantum Limit*. Phys. Rev. Lett., 48:1559, 1982. https://doi.org/10.1103/PhysRevLett.48.1559. Cited in page 23.

[21] Hall, E.H.: *XVIII. On the "Rotational Coefficient" in nickel and cobalt*. London Edinburgh Philos. Mag. J. Sci., 12:157, 1881. https://doi.org/10.1080/14786448108627086. Cited in page 24.

[22] Karplus, R. and J. M. Luttinger: *Hall Effect in Ferromagnetics*. Phys. Rev., 95:1154, 1954. https://doi.org/10.1103/PhysRev.95.1154. Cited in page 24.

[23] Dyakonov, M.I. and V.I. Perel: *Current-induced spin orientation of electrons in semiconductors*. Physics Letters A, 35:459, 1971. https://doi.org/10.1016/0375-9601(71)90196-4. Cited in page 24.

[24] Haldane, F. D. M.: *Model for a Quantum Hall Effect without Landau Levels: Condensed-Matter Realization of the "Parity Anomaly"*. Phys. Rev. Lett., 61:2015, 1988. https://doir.org/10.1103/PhysRevLett.61.2015. Cited in page 24.

[25] Kane, C. L. and E. J. Mele: *Quantum Spin Hall Effect in Graphene*. Phys. Rev. Lett., 95:226801, 2005. https://link.aps.org/doi/10.1103/PhysRevLett.95.226801. Cited in page 24.

[26] Sinitsyn, N. A.: *Semiclassical theories of the anomalous Hall effect*. J. Phys-Condens. Mat., 20:023201, 2007. https://doi.org/10.1088/0953-8984/20/02/023201. Cited in page 24.

[27] Kane, C. L. and E. J. Mele: *$Z_2$ Topological Order and the Quantum Spin Hall Effect*. Phys. Rev. Lett., 95:146802, 2005. https://doi.org/10.1103/PhysRevLett.95.146802. Cited 2 times in pages 24 and 60.

[28] Bernevig, B. A., T. L. Hughes, and S. C. Zhang: *Quantum Spin Hall Effect and Topological Phase Transition in HgTe Quantum Wells*. Science, 314:5, 2006. https://doi.org/10.1126/science.1133734. Cited in page 24.

[29] Asboth, J. K., L. Oroszlany, and A. P. Palyi: *A Short Course on Topological Insulators: Band Structure and Edge States in One and Two Dimensions*. Springer International Publishing, 2016, ISBN 9783319256078. Cited in page 25.

[30] Kramers, H. A.: *Semiclassical theories of the anomalous Hall effect*. Proc. Amsterdam Acad., 33:959, 1930. Cited in page 27.

[31] Ortmann, F., S. Roche, S. O. Valenzuela, and L. W. Molenkamp: *Topological Insulators: Fundamentals and Perspectives*. Wiley, 2015, ISBN 9783527681600. Cited in page 28.

[32] Hasan, M. Z. and C. L. Kane: *Colloquium: Topological Insulators*. Rev. Mod. Phys., 82:3045, 2010. https://doi.org/10.1103/RevModPhys.82.3045. Cited 3 times in pages 28, 60, and 72.

[33] Hsieh, D., D. Qian, L. Wray, Y. Xia, Y. S. Hor, R. J. Cava, and M. Z. Hasan: *A Topological Dirac Insulator in a Quantum Spin Hall Phase*. Nature, 452:970, 2008. https://doi.org/10.1038/nature06843. Cited in page 30.

[34] Zhang, H., C. X. Liu, X. L. Qi, X. Dai, Z. Fang, and S. C. Zhang: *Topological Insulators in $Bi_2Se_3$, $Bi_2Te_3$ and $Sb_2Te_3$ with a Single Dirac Cone on the Surface*. Nat. Phys., 5:438, 2009. https://doi.org/10.1038/nphys1270. Cited 2 times in pages 31 and 60.

[35] Shen, S. Q.: *Topological Insulators: Dirac Equation in Condensed Matter*. Springer Singapore, 2017, ISBN 9789811046063. Cited in page 32.

[36] Yan, B. and C. Felser: *Topological Materials: Weyl Semimetals*. Annu. Rev. Condens. Matter., 8:337, 2017. https://doi.org/10.1146/annurev-conmatphys-031016-025458. Cited 2 times in pages 32 and 60.

[37] Pal, P. B.: *Dirac, Majorana, and Weyl fermions*. Am. J. Phys., 79:485, 2011. https://doi.org/10.1119/1.3549729. Cited in page 32.

[38] Armitage, N. P., E. J. Mele, and A. Vishwanath: *Weyl and Dirac semimetals in three-dimensional solids*. Rev. Mod. Phys., 90:015001, 2018. https://doi.org/10.1103/RevModPhys.90.015001. Cited 2 times in pages 32 and 35.

[39] Dirac, P. A. M. and R. H. Fowler: *The quantum theory of the electron*. P. R. Soc. Lond. A-Conta., 117:610, 1928. https://doi.org/10.1098/rspa.1928.0023. Cited in page 32.

[40] Weyl, H.: *Elektron und gravitation. i*. Z. Physik, 56:330, 1929. https://doi.org/10.1007/BF01339504. Cited in page 33.

[41] Hasan, M. Z., S. Xu, I. Belopolski, and S. Huang: *Discovery of Weyl Fermion Semimetals and Topological Fermi Arc States*. Annu. Rev. Condens. Matter, 8:289, 2017. https://doi.org/10.1146/annurev-conmatphys-031016-025225. Cited in page 33.

[42] Thiang, G. C., K. Sato, and K. Gomi: *Fu–Kane–Mele monopoles in semimetals*. Nucl. Phys. B, 923:107, 2017. https://doi.org/10.1016/j.nuclphysb.2017.07.018. Cited in page 33.

[43] Zyuzin, A. A., S. Wu, and A. A. Burkov: *Weyl semimetal with broken time reversal and inversion symmetries*. Phys. Rev. B, 85:165110, 2012. https://doi.org/10.1103/PhysRevB.85.165110. Cited in page 34.

[44] Yang, B. J. and N. Nagaosa: *Classification of stable three-dimensional Dirac semimetals with nontrivial topology*. Nature Commun., 5:4898, 2014. https://doi.org/10.1038/ncomms5898. Cited in page 34.

[45] Jia, S., S. Y. Xu, and M. Hasan: *Weyl semimetals, Fermi arcs and chiral anomalies*. Nature Mater, 15:1140, 2016. https://doi.org/10.1038/nmat4787. Cited 2 times in pages 35 and 78.

[46] Yuan, X., C. Zhang, Y. Zhang, Z. Yan, T. Lyu, M. Zhang, Z. Li, C. Song, M. Zhao, P. Leng, M. Ozerov, X. Chen, N. Wang, Y. Shi, H. Yan, and F. Xiu: *The discovery of dynamic chiral anomaly in a Weyl semimetal NbAs*. Nat. Commun., 11:1259, 2020. https://doi.org/10.1038/s41467-020-14749-4. Cited in page 35.

[47] Burkov, A. A.: *Anomalous Hall Effect in Weyl Metals.* Phys. Rev. Lett., 113:187202, 2014. https://link.aps.org/doi/10.1103/PhysRevLett.113.187202. Cited in page 35.

[48] Lv, B. Q., H. M. Weng, B. B. Fu, X. P. Wang, H. Miao, J. Ma, P. Richard, X. C. Huang, L. X. Zhao, G. F. Chen, Z. Fang, X. Dai, T. Qian, and H. Ding: *Experimental Discovery of Weyl Semimetal TaAs.* Phys. Rev. X, 5:031013, 2015. https://link.aps.org/doi/10.1103/PhysRevX.5.031013. Cited in page 36.

[49] Xu, S., I. Belopolski, D. S. Sanchez, C. Zhang, G. Chang, C. Guo, G. Bian, Z. Yuan, H. Lu, T. Chang, P. P. Shibayev, M. L. Prokopovych, N. Alidoust, H. Zheng, C. Lee, S. Huang, R. Sankar, F. Chou, C. Hsu, H. Jeng, A. Bansil, T. Neupert, V. N. Strocov, H. Lin, and S. Jia M. Z. Hasan: *Experimental discovery of a topological Weyl semimetal state in TaP.* Sci. Adv., 1:10, 2015. https://doi.org/10.1126/sciadv.1501092. Cited in page 36.

[50] Modic, K. A., T. Meng, F. Ronning, E. D. Bauer, P. J. W. Moll, and B. J. Ramshaw: *Thermodynamic Signatures of Weyl Fermions in NbP.* Sci. Rep., 9:20950, 2019. https://doi.org/10.1038/s41598-018-38161-7. Cited in page 36.

[51] Xu, S., N. Alidoust, I. Belopolski, Z. Yuan, G. Bian, T. Chang, H. Zheng, V. N. Strocov, D. S. Sanchez, G. Chang, C. Zhang, D. Mou, Y. Wu, L. Huang, C. Lee, S. Huang, B. Wang, A. Bansil, H. Jeng, T. Neupert, A. Kaminski, H. Lin, S. Jia, and M. Z. Hasan: *Discovery of a Weyl fermion state with Fermi arcs in niobium arsenide.* Nature Phys., 11:748, 2015. https://doi.org/10.1038/nphys3437. Cited in page 36.

[52] Jiang, J., Z. K. Liu, Y. Sun, H. F. Yang, C. R. Rajamathi, Y. P. Qi, L. X. Yang, C. Chen, H. Peng, C. Hwang, S. Z. Sun, S. Mo, I. Vobornik, J. Fujii, S. S. P. Parkin, C. Felser, B. H. Yan, and Y. L. Chen: *Signature of type-II Weyl semimetal phase in* $MoTe_2$. Nat. Commun., 8:13973, 2017. https://doi.org/10.1038/ncomms13973. Cited in page 36.

[53] Li, P., Y. Wen, X. He, Q. Zhang, C. Xia, Z. Yu, S. A. Yang, Z. Zhu, H. N. Alshareef, and X. Zhang: *Evidence for topological type-II Weyl semimetal* $WTe_2$. Nat. Commun., 8:2150, 2017. https://doi.org/10.1038/s41467-017-02237-1. Cited in page 36.

[54] Tsai, H., T. Higo, K. Kondou, T. Nomoto, A. Sakai, A. Kobayashi, T. Nakano, K. Yakushiji, R. Arita, S. Miwaand Y. Otani, and S. Nakatsuji: *Electrical manipulation of a topological antiferromagnetic state.* Nature, 580:608, 2020. https://doi.org/10.1038/s41586-020-2211-2. Cited in page 36.

[55] Peccei, R. D. and H. R. Quinn: CP *Conservation in the Presence of Pseudoparticles*. Phys. Rev. Lett., 38:1440, 1977. https://doi.org/10.1103/PhysRevLett.38.1440. Cited in page 36.

[56] Wilczek, F.: *Two applications of axion electrodynamics*. Phys. Rev. Lett., 58:1799, 1987. https://doi.org/10.1103/PhysRevLett.58.1799. Cited in page 37.

[57] Sekine, A. and K. Nomura: *Axion electrodynamics in topological materials*. J. Appl. Phys., 129:141101, 2021. https://doi.org/10.1063/5.0038804. Cited 2 times in pages 37 and 80.

[58] Fiebig, M.: *Revival of the magnetoelectric effect*. J. Phys. D Appl. Phys., 38:R123, 2005. https://doi.org/10.1088/0022-3727/38/8/r01. Cited in page 37.

[59] Wan, W., A. M. Turner, A. Vishwanath, and S. Y. Savrasov: *Topological semimetal and Fermi-arc surface states in the electronic structure of pyrochlore iridates*. Phys. Rev. B, 83:205101, 2011. https://doi.org/10.1103/PhysRevB.83.205101. Cited in page 37.

[60] Hou, Y. S., J. W. Kim, and R. Q. Wu: *Axion insulator state in ferromagnetically ordered $CrI_3/Bi_2Se_3/MnBi_2Se_4$ heterostructures*. Phys. Rev. B, 101:121401, 2020. https://doi.org/10.1103/PhysRevB.101.121401. Cited in page 37.

[61] Wang, Z. and S. Zhang: *Chiral anomaly, charge density waves, and axion strings from Weyl semimetals*. Phys. Rev. B, 87:161107, 2013. https://link.aps.org/doi/10.1103/PhysRevB.87.161107. Cited in page 37.

[62] Gooth, J., B. Bradlyn, S. Honnali, C. Schindler, N. Kumar, J. Noky, Y. Qi, C. Shekhar, Y. Sun, Z. Wang, B. A. Bernevig, and C. Felser: *Axionic Charge-density Wave in the Weyl Semimetal $(TaSe_4)_2I$*. Nature, 575:315, 2019. https://doi.org/10.1038/s41586-019-1630-4. Cited 4 times in pages 37, 72, 78, and 79.

[63] Hufner, S. and T. W. Huber: *Photoelectron Spectroscopy: Principles and Applications*. Springer, 2003, ISBN 9783540418023. Cited 5 times in pages 38, 40, 45, 47, and 51.

[64] Hertz, H.: *Ueber einen Einfluss des ultravioletten Lichtes auf die electrische Entladung*. Annalen der Physik, 267:983, 1887. https://doi.org/10.1002/andp.18872670827. Cited in page 38.

[65] Hallwachs, W.: *Ueber den Einfluss des Lichtes auf electrostatisch geladene Körper*. Annalen der Physik, 269:301, 1888. https://doi.org/10.1002/andp.18882690206. Cited in page 38.

[66] Lenard, P.: *Ueber die lichtelektrische Wirkung*. Annalen der Physik, 313:149, 1902. https://doi.org/10.1002/andp.19023130510. Cited 2 times in pages 38 and 39.

[67] Palmer, F.: *Ionisation of Air by Ultra-violet Light*. Annalen der Physik, 77:582, 1902. https://doi.org/10.1002/andp.19023130510https://doi.org/10.1038/077582b0. Cited in page 39.

[68] Einstein, A.: *Über einen die Erzeugung und Verwandlung des Lichtes betreffenden heuristischen Gesichtspunkt*. Annalen der Physik, 322:132, 1905. https://doi.org/10.1002/andp.19053220607. Cited in page 39.

[69] Lide, D. R.: *CRC Handbook of Chemistry and Physics, 89th Edition*. Taylor & Francis, 2008, ISBN 9781420066791. Cited in page 40.

[70] Moulder, J. F. and J. Chastain: *Handbook of X-ray Photoelectron Spectroscopy: A Reference Book of Standard Spectra for Identification and Interpretation of XPS Data*. Physical Electronics Division, Perkin-Elmer Corp., 1992, ISBN 9780962702624. Cited 2 times in pages 41 and 65.

[71] Cohen, M. L. and S. G. Louie: *Fundamentals of Condensed Matter Physics*. Cambridge University Press, 2016, ISBN 9780521513319. Cited in page 42.

[72] Damascelli, A., Z. Hussain, and Z. X. Shen: *Angle-Resolved Photoemission Studies of the Cuprate Superconductors*. Rev. Mod. Phys., 75:473, 2003. https://doi.org/10.1103/RevModPhys.75.473. Cited 4 times in pages 43, 44, 55, and 72.

[73] Weinelt, M.: *Time-resolved two-photon photoemission from metal surfaces*. J. Phys.-Condens. Mat., 14:R1099, 2002. https://doi.org/10.1088/0953-8984/14/43/202. Cited in page 45.

[74] P.Dirac and N. Bohr: *The quantum theory of the emission and absorption of radiation*. P. R. Soc. Lond. A-Conta., 114:243, 1927. https://doi.org/10.1098/rspa.1927.0039. Cited in page 45.

[75] Hecht, K. T., J. L. Birman, J. W. Lynn, M. P. Silverman, H. E. Stanley, and M. Voloshin: *Quantum Mechanics*. Springer New York, 2000, ISBN 9780387989198. Cited in page 46.

[76] Karkare, S., W. Wan, J. Feng, T. Chiang, and H. A. Padmore: *One-step model of photoemission from single-crystal surfaces*. Phys. Rev. B, 95:075439, 2017. https://doi.org/10.1103/PhysRevB.95.075439. Cited in page 46.

[77] Maldonado, J. R., P. Pianetta, D. H. Dowell, J. Corbett, S. Park, J. Schmerge, A. Trautwein, and W. Clay: *Experimental verification of the 3-step model of photoemission for energy spread and emittance measurements of copper and CsBr-coated copper photocathodes suitable for free electron laser applications*. Appl. Phys. Lett., 101:231103, 2012. https://doi.org/10.1063/1.4769220. Cited in page 46.

[78] Das, P. and N. Kar: *Photoemission calculation using LEED type wavefunctions and a spatially varying photon field*. Mod. Phys. Lett. B, 09:947, 1995. https://doi.org/10.1142/S0217984995000905. Cited in page 46.

[79] Seah, M. P. and W. A. Dench: *Quantitative Electron Spectroscopy of Surfaces: A Standard database for Electron Inelastic Mean Free Paths in Solids*. Surf. Interface Anal., 1:2, 1979. https://doi.org/10.1002/sia.740010103. Cited 3 times in pages 47, 52, and 53.

[80] Dirac, P. and R. Fowler: *On the theory of quantum mechanics*. P. R. Soc. Lond. A-Conta., 112:661, 1926. https://doi.org/10.1098/rspa.1926.0133. Cited in page 48.

[81] Anisimov, V. and Y. Izyumov: *Electronic Structure of Strongly Correlated Materials*. Springer Berlin Heidelberg, 2010, ISBN 9783642048265. Cited in page 49.

[82] Bardeen, J., L. N. Cooper, and J. R. Schrieffer: *Microscopic Theory of Superconductivity*. Phys. Rev., 106:162, 1957. https://doi.org/10.1103/PhysRev.106.162. Cited in page 49.

[83] Phillips, J.: *Physics Of High-Tc Superconductors*. Elsevier Science, 2012, ISBN 9780323151993. Cited in page 49.

[84] Brandow, B. H.: *Electronic structure of Mott insulators*. Adv. Phys., 26:651, 1977. https://doi.org/10.1080/00018737700101443. Cited in page 49.

[85] Stewart, G. R.: *Heavy-fermion systems*. Rev. Mod. Phys., 56:755, 1984. https://doi.org/10.1103/RevModPhys.56.755. Cited in page 49.

[86] Gonzalez, J., F. Guinea, and M. Vozmediano: *Electron-electron interactions in graphene sheets*. Phys. Rev. B, 63:134421, 2001. https://doi.org/10.1103/PhysRevB.63.134421. Cited in page 49.

[87] Cuk, T., D. Lu, X. J. Zhou, Z. Shen, T. P. Devereaux, and N. Nagaosa: *A review of electron–phonon coupling seen in the high-$T_c$ superconductors by angle-resolved photoemission studies (ARPES)*. Phys. Status Solidi B, 242:11, 2005. https://doi.org/10.1002/pssb.200404959. Cited in page 49.

[88] Woolsey, R. and R. M. White: *Electron-Magnon Interaction in Ferromagnetic Semiconductors*. Phys. Rev. B, 1:4474, 1970. https://doi.org/10.1103/PhysRevB.1.4474. Cited in page 49.

[89] Hedin, L. and J. D. Lee: *Sudden approximation in photoemission and beyond*. J. Electron Spectrosc., 124:289, 2002. https://doi.org/10.1016/S0368-2048(02)00060-9. Cited in page 49.

[90] King, F. W.: *Hilbert Transforms*. Cambridge University Press, 2009, ISBN 9781139887144. Cited in page 51.

[91] Bogaerts, A., E. Neyts, and R. Gijbels: *Gas discharge plasmas and their applications*. Spectrochim. Acta B, 57:609–658, 2002. https://doi.org/10.1016/S0584-8547(01)00406-2. Cited in page 53.

[92] Ryde, J. W.: *Rare Gas Discharge Lamps*. Nature, 112:994, 1923. https://doi.org/10.1038/112944a0. Cited in page 53.

[93] Als-Nielsen, J. and D. McMorrow: *Elements of Modern X-ray Physics*. Wiley, 2011, ISBN 9781119970156. Cited in page 54.

[94] Zhang, Y., L. Yang, F. Chen, B. Zhou, X. F. Wang, X. H. Chen, M. Arita, K. Shimada, H. Namatame, M. Taniguchi, J. P. Hu, B. P. Xie, and D. L. Feng: *Out-of-Plane Momentum and Symmetry-Dependent Energy Gap of the Pnictide $Ba_{0.6}K_{0.4}Fe_2As_2$ Superconductor Revealed by Angle-Resolved Photoemission Spectroscopy*. Phys. Rev. Lett., 105:117003, 2010. https://doi.org/10.1103/PhysRevLett.105.117003. Cited in page 54.

[95] Pagni, R. M.: *Circular Dichroism and Linear Dichroism (Rodger, Alison; Norden, Bengt)*. J. Chem. Educ., 75:1095, 1998. https://doi.org/10.1021/ed075p1095. Cited in page 55.

[96] Avila, J. and M. C. Asensio: *First NanoARPES User Facility Available at SOLEIL: An Innovative and Powerful Tool for Studying Advanced Materials*. Synchrotron Rad. News, 27:24, 2014. https://doi.org/10.1080/08940886.2014.889549. Cited in page 55.

[97] Borisenko, S. V.: *"One-cubed" ARPES User Facility at BESSY II*. Synchrotron Radiat. News, 25:6, 2012. https://doi.org/10.1080/08940886.2012.720159. Cited in page 55.

[98] Kleinman, D. A., A. Ashkin, and G. D. Boyd: *Second-Harmonic Generation of Light by Focused Laser Beams*. Phys. Rev., 145:338, 1966. https://doi.org/10.1103/PhysRev.145.338. Cited in page 55.

[99] Liu, G., G. Wang, Y. Zhu, H. Zhang, G. Zhang, X. Wang, Y. Zhou, W. Zhang, H. Liu, L. Zhao, J. Meng, X. Dong, C. Chen, Z. Xu, and X. J. Zhou: *Development of a vacuum ultraviolet laser-based angle-resolved photoemission system with a superhigh energy resolution better than 1meV*. Rev. Sci. Instrum., 79:023105, 2008. https://doi.org/10.1063/1.2835901. Cited in page 55.

[100] Tompkins, H. G.: *The Fundamentals of Vacuum Technology*. American Vacuum Society, 1991, ISBN 9780883189979. Cited in page 55.

[101] Tang, C., Z. Rao, Q. Yuan, S. Tian, H. Li, Y. Huang, H. Lei, S. Li, T. Qian, Y. Sun, and H. Ding: *Atomically flat surface preparation for surface-sensitive technologies.* Chinese Phys. B, 29:028101, 2020. https://doi.org/10.1088/1674-1056/ab6586. Cited in page 55.

[102] Herman, M. A. and H. Sitter: *Molecular Beam Epitaxy: Fundamentals and Current Status.* Springer Berlin Heidelberg, 2012, ISBN 9783642800603. Cited in page 55.

[103] Eason, R.: *Pulsed Laser Deposition of Thin Films: Applications-Led Growth of Functional Materials.* Wiley, 2007, ISBN 9780471447092. Cited in page 55.

[104] VanHove, M. A., W. H. Weinberg, and C. M. Chan: *Low-Energy Electron Diffraction: Experiment, Theory and Surface Structure Determination.* Springer Berlin Heidelberg, 2012, ISBN 9783642827211. Cited in page 55.

[105] Binnig, G. and H. Rohrer: *Scanning tunneling microscopy - from birth to adolescence.* Rev. Mod. Phys., 59:615, 1987. https://doi.org/10.1103/RevModPhys.59.615. Cited in page 56.

[106] Rugar, D. and P. Hansma: *Atomic Force Microscopy.* Phys. Today, 43:23, 1990. https://doi.org/10.1063/1.881238. Cited in page 56.

[107] Tusche, C., Y. Chen, C. M. Schneider, and J. Kirschner: *Imaging properties of hemispherical electrostatic energy analyzers for high resolution momentum microscopy.* Ultramicroscopy, 206:112815, 2019. https://doi.org/10.1016/j.ultramic.2019.112815. Cited in page 56.

[108] Kane, C. L. and E. J. Mele: *A New Spin on the Insulating State.* Science, 314:1692, 2006. https://doi.org/10.1126/science.1136573. Cited in page 60.

[109] Xia, Y., D. Qian, D. Hsieh, L. Wray, A. Pal, H. Lin, A. Bansil, D. Grauer, Y. S. Hor, R. J. Cava, and M. Z. Hasan: *Observation of a Large-gap Topological-Insulator Class with a Single Dirac Cone on the Surface.* Nat. Phys, 5:398, 2009. https://doi.org/10.1038/nphys1274. Cited in page 60.

[110] Konig, M., C. Brune S. Wiedmann, A. Roth, H. Buhmann, L. W. Molenkamp, X. L. Qi, and S. C. Zhang: *Quantum Spin Hall Insulator State in HgTe Quantum Wells.* Science, 318:766, 2007. doi.org/10.1126/science.1148047. Cited in page 60.

[111] Asorey, M.: *Space, Matter and Topology.* Nat. Phys., 12:616, 2016. https://doi.org/10.1038/nphys3800. Cited in page 60.

[112] Orgiani, P., C. Bigi, P. Kumar Das, J. Fujii, R. Ciancio, B. Gobaut, A. Galdi, C. Sacco, L. Maritato, P. Torelli, G. Panaccione, I. Vobornik, and G. Rossi: *Structural and Electronic properties of $Bi_2Se_3$ Topological Insulator Thin Films Grown by Pulsed*

*Laser Deposition*. Appl. Phys. Lett., 110:171601, 2017. https://doi.org/10.1063/1.4982207. Cited 3 times in pages 60, 66, and 68.

[113] Hsieh, D., Y. Xia, D., L. Wray, F. Meier, J. H. Dil, J. Osterwalder, L. Patthey, A. V. Fedorov, H. Lin, A. Bansil, D. Grauer, Y. S. Hor, R. J. Cava, and M. Z. Hasan: *Observation of Time-Reversal-Protected Single-Dirac-Cone Topological-Insulator States in $Bi_2Te_3$ and $Sb_2Te_3$*. Phys. Rev. Lett., 103:146401, 2009. https://doi.org/10.1103/PhysRevLett.103.146401. Cited in page 60.

[114] Roushan, P., J. Seo, C. V. Parker, Y. S. Hor, D. Hsieh, D. Qian, A. Richardella, M. Z. Hasan, R. J. Cava, and A. Yazdani: *Topological Surface States Protected from Backscattering by Chiral Spin Texture*. Nature, 460:1106, 2009. https://doi.org/10.1038/nature08308. Cited in page 60.

[115] Deng, J. and Z. Y. Zhao: *Electronic Structure and Optical Properties of Bismuth Chalcogenides $Bi_2Q_3$ (Q = O, S, Se, Te) by first-principles calculations*. Com. Mat. Sci., 142:312, 2018. https://doi.org/10.1016/j.commatsci.2017.10.032. Cited in page 60.

[116] Gonçalves, P. H. R., T. Chagas, V. B. Nascimento, D. D. Reis, C. Parra, M. S. C. Mazzoni, A. Malachias, and R. Magalhães-Paniago: *Formation of $Bi_xSe_y$ Phases Upon Annealing of the Topological Insulator $Bi_2Se_3$: Stabilization of In-Depth Bismuth Bilayers*. J. Phys. Chem. Lett., 9:954, 2018. https://doi.org/10.1021/acs.jpclett.7b03172. Cited in page 60.

[117] Wang, S., Y. Sun, J. Yang, B. Duan, L. Wu, W. Zhang, and J. Yang: *High Thermoelectric Performance in Te-free $(Bi,Sb)_2Se_3$ via Structural Transition Induced Band Convergence and Chemical Bond Softening*. Energy Environ. Sci., 9:3436, 2016. https://doi.org/10.1039/c6ee02674e. Cited 2 times in pages 60 and 61.

[118] Coelho, P. M., G. A. S. Ribeiro, A. Malachias, V. L. Pimentel, W. S. Silva, D. D. Reis, M. S. C. Mazzoni, and R. Magalhães-Paniago: *Temperature-Induced Coexistence of a Conducting Bilayer and the Bulk-Terminated Surface of the Topological Insulator $Bi_2Te_3$*. Nano Lett., 13:4517, 2013. https://doi.org/10.1021/nl402450b. Cited in page 60.

[119] Parra, C., T. H. R. Cunha, A. W. Contryman, D. Kong, F. Montero-Silva, P. H. R. Gonçalves, D. D. Reis, P. Giraldo-Gallo, R. Segura, F. Olivares, F. Niestemski, Y. Cui, R. Magalhães-Paniago, and H. C. Manoharan: *Phase Separation of Dirac Electrons in Topological Insulators at the Spatial Limit*. Nano Lett., 17:97, 2017. https://doi.org/10.1021/acs.nanolett.6b03506. Cited in page 60.

[120] Koumoulis, D., B. Leung, T. C. Chasapis, R. Taylor, D. King Jr., M. G. Kanatzidis, and L. S. Bouchard: *Understanding Bulk Defects in Topological Insulators from*

*Nuclear-Spin Interactions*. Adv. Func. Mat., 24:11, 2014. https://doi.org/10.1002/adfm.201302673. Cited in page 60.

[121] Mi, J. L., M. Bremholm, M. Bianchi, K. Borup, S. Johnsen, M. Søndergaard, D. Guan, R. C. Hatch, P. Hofmann, and B. B. Iversen: *Phase Separation and Bulk p-n Transition in Single Crystals of $Bi_2Te_2Se$ Topological Insulator*. Adv. Mat., 25:6, 2013. https://doi.org/10.1002/adma.201203542. Cited in page 60.

[122] Lohani, H., P. Mishra, A. Banerjee, K. Majhi, R. Ganesan, U. Manju, D. Topwal, P. S. Anil Kumar, and B. R. Sekhar: *Band Structure of Topological Insulator $BiSbTe_{1.25}Se_{1.75}$*. Sci. Rep., 7:4567, 2017. https://doi.org/10.1038/s41598-017-04985-y. Cited 2 times in pages 60 and 67.

[123] Lei, T., K. H. Jin, N. Zhang, J. L. Zhao, C. Liu, W. J. Li, J. O. Wang, R. Wu, H. J. Qian, F. Liu, and K. Ibrahim: *Electronic Structure Evolution of Single Bilayer Bi(111) Film on 3D Topological Insulator $Bi_2Se_xTe_{3-x}$ surfaces*. J. Phys.: Condens. Matter., 28:255501, 2016. https://doi.org/10.1088/0953-8984/28/25/255501. Cited 2 times in pages 61 and 67.

[124] Zhou, B., Z. K. Liu, J. G. Analytis, K. Igarashi, S. K. Mo, D. H. Lu, R. G. Moore, I. R. Fisher, T. Sasagawa, Z. X. Shen, Z. Hussain, and Y. L. Chen: *Controlling the Carriers of Topological Insulators by Bulk and Surface Doping*. Semicond. Sci. Technol., 27:124002, 2012. https://doi.org/10.1088/0268-1242/27/12/124002. Cited 2 times in pages 61 and 67.

[125] Zhang, Y., C. Z. Chang, K. He, L. L. Wang, X. Chen, J. F. Jia, X. C. Ma, and Q. K. Xue: *Doping Effects of Sb and Pb in Epitaxial Topological Insulator Thin Films: An in Situ Angle-Resolved Photoemission Spectroscopy Study*. Appl. Phys. Lett., 97:194102, 2010. https://doi.org/10.1063/1.3516160. Cited 2 times in pages 61 and 67.

[126] Li, J., B. Wang, F. Liu, J. Liu, M. Jia, Y. Lai, J. Li, and Y. Liu: *Structural and Optical Properties of Electrodeposited $Bi_{2-x}Sb_xSe_3$ Thin Films*. ECS Solid State Lett., 1:29, 2012. https://doi.org/10.1149/2.001203ssl. Cited in page 61.

[127] Xuelai, L., S. Zhimei, S. Zhitang, R. Feng, W. Liangcai, and L. Weili: *Ab initio Study of $Sb_2Se_xTe_{3-x}$ (x = 0, 1, 2) Phase Change Materials*. Solid State Sci., 13:131, 2011. https://doi.org/10.1016/j.solidstatesciences.2010.10.025. Cited in page 61.

[128] Hor, Y. S., A. Richardella, P. Roushan, Y. Xia, J. G. Checkelsky, A. Yazdani, M. Z. Hasan, N. P. Ong, and R. J. Cava: *p-Type $Bi_2Se_3$ for Topological Insulator and Low-Temperature Thermoelectric Applications*. Phys. Rev. B, 79:195208, 2009. https://doi.org/10.1103/PhysRevB.79.195208. Cited 2 times in pages 61 and 66.

[129] Dai, J., D. West, X. Wang, Y. Wang, D. Kwok, S. W. Cheong, S. B. Zhang, and W. Wu: *Toward the Intrinsic Limit of the Topological Insulator $Bi_2Se_3$*. Phys. Rev. Lett., 117:106401, 2016. https://doi.org/10.1103/PhysRevLett.117.106401. Cited 2 times in pages 61 and 66.

[130] Scanlon, D. O., P. D. C. King, R. P. Singh, A. de la Torre, S. M. Walker, G. Balakrishnan, F. Baumberger, and C. R. A. Catlow: *Controlling Bulk Conductivity in Topological Insulators: Key Role of Anti-Site Defects*. Adv. Mat., 24:16, 2012. https://doi.org/10.1002/adma.201200187. Cited 2 times in pages 61 and 67.

[131] Rudolph, P. and F. M. Kiessling: *The Horizontal Bridgman Method*. Cryst. Res. Technol., 23:1207, 1988. https://doi.org/10.1002/crat.2170231002. Cited 2 times in pages 61 and 62.

[132] Kong, D., Y. Chen, J. J. Cha, Q. Zhang, J. G. Analytis, K. Lai, Z. Liu, S. S. Hong, K. J. Koski, S. K. Mo, Z. Hussain, I. R. Fisher, Z. X. Shen, and Y. Cui: *Ambipolar Field Effect in the Ternary Topological Insulator $(Bi_xSb_{1-x})_2Te_3$ by composition tuning*. Nat. Nanotechnol., 6:705, 2011. https://doi.org/10.1038/nnano.2011.172. Cited in page 67.

[133] Ariel, V. and A. Natan: *Electron Effective Mass in Graphene*, 2012. https://arxiv.org/abs/1206.6100v2. Cited in page 68.

[134] Yin, J., H. Krishnamoorthy, G. Adamo, A. M. Dubrovkin, Y. Chong, N. I. Zheludev, and C. Soci: *Plasmonics of Topological Insulators at Optical Frequencies*. NPG Asia Mater., 9:425, 2017. https://doi.org/10.1038/am.2017.149. Cited in page 68.

[135] Plakida, N. M.: *Lattice Instability and Strong Electron-phonon Coupling for High-$T_c$ Superconductivity*. Physica C, 162-164:1341, 1989. https://doi.org/10.1016/0921-4534(89)90723-5. Cited in page 70.

[136] Lee, S. H., J. S. Goh, and D. Cho: *Origin of the Insulating Phase and First-Order Metal-Insulator Transition in 1T-$TaS_2$*. Phys. Rev. Lett., 122:106404, 2019. https://10.1103/PhysRevLett.122.106404. Cited in page 72.

[137] Chikina, A., A. Fedorov, D. Bhoi, V. Voroshnin, E. Haubold, Y. Kushnirenko, K. Hoon Kim, and S. Borisenko: *Turning Charge-density Waves into Cooper Pairs*. NPJ Quantum Mater., 5:22, 2020. https://doi.org/10.1038/s41535-020-0225-5. Cited in page 72.

[138] Boswell, F. W., A. Prodan, and J. K. Brandon: *Charge-density Waves in the Quasi-one-dimensional Compounds $NbTe_4$ and $TaTe_4$*. J. Phys. C Solid State, 16:1067, 1983. https://doi.org/10.1088/0022-3719/16/6/012. Cited 2 times in pages 72 and 73.

[139] Yang, X., Y. Zhou, M. Wang, H. Bai, X. Chen, C. An, Y. Zhou, Q. Chen, Y. Li, Z. Wang, J. Chen, C. Cao, Y. Li, Y. Zhou, Z. Yang, and Z. A. Xu: *Pressure Induced Superconductivity Bordering a Charge-density-wave State in $NbTe_4$ with Strong Spin-orbit Coupling*. Sci. Rep., 8:6298, 2018. https://doi.org/10.1038/s41598-018-24572-z. Cited in page 72.

[140] Yuan, Y., W. Wang, Y. Zhou, X. Chen, C. Gu, C. An, Y. Zhou, B. Zhang, C. Chen, R. Zhang, and Z. Yang: *Pressure-Induced Superconductivity in Topological Semimetal Candidate $TaTe_4$*. Adv. Electron. Mater., 6:1901260, 2020. https://doi.org/10.1002/aelm.201901260. Cited 2 times in pages 72 and 78.

[141] Yu, Peter Y. and Manuel Cardona: *Fundamentals of Semiconductors: Physics and Materials Properties*. Springer, Berlin, Heidelberg, 2005. https://doi.org/10.1007/978-3-642-00710-1. Cited in page 72.

[142] Burkov, A. A.: *Topological Semimetals*. Nat. Mater., 15:1145, 2016. https://doi.org/10.1038/nmat4788. Cited in page 72.

[143] Zhang, T., Y. Jiang, Z. Song, H. Huang, Y. He, Z. Fang, H. Weng, and C. Fang: *Catalogue of Topological Electronic Materials*. Nature, 566:475, 2019. https://doi.org/10.1038/s41586-019-0944-6. Cited in page 72.

[144] Manzeli, S., D. Ovchinnikov, D. Pasquier, O. V. Yazyev, and A. Kis: *2D Transition Metal Dichalcogenides*. Nat. Rev. Mater., 2:17033, 2017. https://doi.org/10.1038/natrevmats.2017.33. Cited in page 72.

[145] Splendiani, A., L. Sun, Y. Zhang, T. Li, J. Kim, C. Y. Chim, G. Galli, and F. Wang: *Emerging Photoluminescence in Monolayer $MoS_2$*. Nano Lett., 10:1271, 2010. https://doi.org/10.1021/nl903868w. Cited in page 72.

[146] Yin, Z., H. Li, H. Li, L. Jiang, Y. Shi, Y. Sun, G. Lu, Q. Zhang, X. Chen, and H. Zhang: *Single-Layer $MoS_2$ Phototransistors*. ACS Nano, 6:74, 2012. https://doi.org/. Cited in page 72.

[147] Deng, K., G. Wan, P. Deng, K. Zhang, S. Ding, E. Wang, M. Yan, H. Huang, H. Zhang, Z. Xu, J. Denlinger, A. Fedorov, H. Yang, W. Duan, H. Yao, Y. Wu, S. Fan, H. Zhang, X. Chen, and S. Zhou: *Experimental Observation of Topological Fermi Arcs in Type-II Weyl Semimetal $MoTe_2$*. Nat. Phys., 12:1105, 2016. https://doi.org/10.1021/nn2024557. Cited in page 72.

[148] Wang, H., X. Huang, J. Lin, J. Cui, Y. Chen, C. Zhu, F. Liu, Q. Zeng, J. Zhou, P. Yu, X. Wang, H. He, S. H. Tsang, W. Gao, K. Suenaga, F. Ma, C. Yang, L. Lu, T. Yu, E. H. T. Teo, G. Liu, and Z. Liu: *High-Quality Monolayer Superconductor*

*$NbSe_2$ Grown by Chemical Vapour Deposition*. Nature Commun., 8:394, 2017. https://doi.org/10.1038/s41467-017-00427-5. Cited in page 72.

[149] Island, J. O., A. J. Molina-Mendoza, M. Barawi, R. Biele, E. Flores, J. M. Clamagirand, J. R. Ares, C. Sánchez, H. S. J. van der Zant, R. D'Agosta, I. J. Ferrer, and A. Castellanos-Gomez: *Electronics and Optoelectronics of Quasi-1D Layered Transition Metal Trichalcogenides*. 2D Mater., 4:022003, 2017. https://doi.org/10.1088/2053-1583/aa6ca6. Cited in page 72.

[150] Srivastava, S. K. and B. N. Avasthi: *Preparation, Structure and Properties of Transition Metal Trichalcogenides*. J. Mater. Sci., 27:3693, 1992. https://doi.org/10.1007/BF00545445. Cited in page 72.

[151] Gressier, P., M. H. Whangbo, A. Meerschaut, and J. Rouxel: *Electronic Structures of Transition-metal Tetrachalcogenides $(MSe_4)_nI$ (M = Nb, Ta)*. Inorg. Chem., 23:12213, 1984. https://doi.org/10.1021/ic00177a011. Cited in page 72.

[152] Grüner, G.: *The Dynamics of Charge-density Waves*. Rev. Mod. Phys., 60:1129, 1988. https://doi.org/10.1103/RevModPhys.60.1129. Cited in page 72.

[153] Grüner, G.: *The Dynamics of Spin-density Waves*. Rev. Mod. Phys., 66:1, 1994. https://doi.org/10.1103/RevModPhys.66.1. Cited in page 72.

[154] Wang, Z. Z., M. C. Saint-Lager, P. Monceau, M. Renard, P. Gressier, A. Meerschaut, L. Guemas, and J.Rouxel: *Charge Density Wave Transport in $(TaSe_4)_2I$*. Solid State Commun., 46:325, 1983. https://doi.org/10.1016/0038-1098(83)90662-2. Cited in page 72.

[155] Maki, M., M. Kaiser, A. Zettl, and G. Grüner: *Charge Density Wave Transport in a Novel Inorganic Chain Compound, $(TaSe_4)_2I$*. Solid State Commun., 46:497, 1983. https://doi.org/10.1016/0038-1098(83)90676-2. Cited in page 72.

[156] Philipp, A., W. Mayr, T. W. Kim, B. Alavi, M. Maki, and G. Grüner: *Dynamics of the Charge-density-wave Mode in $(NbSe_4)_2I$*. Phys. Rev. B, 39:7536, 1989. https://doi.org/10.1103/PhysRevB.39.7536. Cited in page 72.

[157] Bjerkelund, E. and A. Kjekshus: *On the Crystal Structure of $TaTe_4$*. J. Less-Common. Met., 7:231, 1964. https://doi.org/10.1016/0022-5088(64)90071-2. Cited in page 73.

[158] Luo, X., F. C. Chen, Q. L. Pei, J. J. Gao, J. Yan, W. J. Lu, P. Tong, Y. Y. Han, W. H. Song, and Y. P. Sun: *Resistivity Plateau and Large Magnetoresistance in the Charge Density Wave System $TaTe_4$*. Appl. Phys. Lett., 110:092401, 2017. https://doi.org/10.1063/1.4977708. Cited 4 times in pages 73, 77, 78, and 79.

[159] Gao, Y., L. Xu, Y. Qiu, Z. Tian, S. Yuan, and J. Wang: *Anisotropic Large Magnetoresistance in $TaTe_4$ Single Crystals.* J. Appl. Phys., 122:135101, 2017. https://doi.org/10.1063/1.5005907. Cited 4 times in pages 73, 74, 77, and 79.

[160] Sambongi, T., S. Tadaki, N. Hino, and K. Nomura: *Shubnikov-de Haas Study of $TaTe_4$.* Synthetic Met., 58:109, 1993. https://doi.org/10.1016/0379-6779(93)91122-I. Cited 4 times in pages 73, 74, 77, and 79.

[161] Zwick, F., H. Berger, M. Grioni, G. Margaritondo, L. Forro, J. LaVeigne, D. B. Tanner, and M. Onellion: *Coexisting One-dimensional and Three-dimensional Spectral Signatures in $TaTe_4$.* Phys. Rev. B, 59:7762, 1999. https://doi.org/10.1103/PhysRevB.59.7762. Cited 4 times in pages 73, 76, 77, and 79.

[162] Hwu, Y., P. Almeras, M. Marsi, H. Berger, F. Levy, M. Grioni, D. Malterre, and G. Margaritondo: *Photoemission Near the Fermi Energy in One Dimension.* Phys. Rev. B, 46:13624, 1992. https://doi.org/10.1103/PhysRevB.46.13624. Cited 2 times in pages 73 and 76.

[163] Coluzza, C., H. Berger, P. Almeras, F. Gozzo, G. Margaritondo, G. Indlekofer, L. Forro, and Y. Hwu: *High-Resolution Tests of Low-dimensionality Effects in Photoemission.* Phys. Rev. B, 47:6625, 1993. https://doi.org/10.1103/PhysRevB.47.6625. Cited 2 times in pages 73 and 76.

[164] Byrappa, K. and T. Ohachi: *Crystal Growth Technology.* Springer, 2003, ISBN 9783540003670. Cited in page 74.

[165] Li, X. P., K. Deng, B. Fu, Y. Li, D. Ma, J. Han, J. Zhou, S. Zhou, and Y. Yao: *Type-III Weyl Semimetals: $(TaSe_4)_2I$.* Phys. Rev. B, 103:L081402, 2021. https://doi.org/10.1103/PhysRevB.103.L081402. Cited 2 times in pages 78 and 79.

[166] Shi, W., B. J. Wieder, H. L. Meyerheim, Y. Sun, Y. Zhang, Y. Li, L. Shen, Y. Qi, L. Yang, J. Jena, P. Werner, K. Koepernik, S. Parkin, Y. Chen, C. Felser, B. A. Bernevig, and Z. Wang: *A Charge-density-wave Topological Semimetal.* Nat. Phys., 17:381, 2021. https://doi.org/10.1038/s41567-020-01104-z. Cited in page 79.